Diagnostic of the solar transition region and corona from VUV spectroscopy and imaging

Von der Fakultät für Elektrotechnik, Informationstechnik, Physik
der Technischen Universität Carolo-Wilhelmina
zu Braunschweig
zur Erlangung des Grades einer
Doktorin der Naturwissenschaften
(Dr.rer.nat.)
genehmigte
Dissertation

von Neda Dadashigharehbalagh
aus Qaemshahr / Iran

1. Referent: Prof. Dr. Sami K. Solanki
2. Referent: Prof. Dr. Karl-Heinz Glaßmeier
eingereicht am: 1. Februar 2013
mündliche Prüfung (Disputation) am: 3. Mai 2013

Printed in Germany

Vorveröffentlichungen der Dissertation

Teilergebnisse aus dieser Arbeit wurden mit Genehmigung der Fakultät für Elektrotechnik, Informationstechnik, Physik, vertreten durch den Mentor der Arbeit, in folgenden Beiträgen vorab veröffentlicht:

Publikationen

- **Dadashi, N.**, Teriaca, L., Tripathi, D., Solanki, S. K., Wiegelmann, T., Doppler shift of hot coronal lines in a moss area of an active region, Astronomy and Astrophysics, 548, 115 (2012)

- **Dadashi, N.**, Teriaca, L., Solanki, S. K., The quiet Sun average Doppler shift of coronal lines up to 2 MK, Astronomy and Astrophysics, 534, 90 (2011)

Tagungsbeiträge

- **Dadashi, N.**, Teriaca, L., Tripathi, D., Solanki, S. K., Wiegelmann, T., Behaviour of the Doppler shift versus temperature for hot coronal lines (1-3 MK) in a moss area of an active region (Poster), The Solar System within Geo- and Astrophysics (Rocks 'n' Stars), Veranstaltungszentrum am Wilhelmsplatz, Göttingen, Germany, 8.-11. Oktober (2012)

- **Dadashi, N.**, Teriaca, L., Tripathi, D., Solanki, S. K., Wiegelmann, T., The average Doppler shift of TR and coronal lines on the quiet Sun and active region (Oral), IGEP seminar, TU Braunschweig, Braunschweig, Germany, 8. Mai (2012)

- **Dadashi, N.**, Teriaca, L., Tripathi, D., Solanki, S. K., Doppler shift of hot coronal lines in a Moss Area of an Active region (Poster), Spectroscopy of the dynamic Sun, University College London, London, UK, 18.-20. April (2012)

- **Dadashi, N.**, Teriaca, L., Tripathi, D., Solanki, The average Doppler shift of transition region and coronal lines (Oral), IMPRS S3 seminar, Katlenburg-Lindau, Germany, 15. Februar (2012)

- **Dadashi, N.**, Teriaca, L., Solanki, S. K., The quiet Sun average Doppler shift of TR and coronal lines up to 2 MK (Poster), 13th European Solar Physics Meeting (ESPM13), Rhodes, Greece, 12.-16. September (2011)

- **Dadashi, N.**, Teriaca, L., Solanki, S. K., The quiet Sun average Doppler shift of TR and coronal lines up to 2 MK (Poster), The sun 360 (Stereo-4/SDO-2/SOHO-25 Workshop), Christian-Albrechts-Universität, Kiel, Germany, 25.-29. Juli (2011)

- **Dadashi, N.**, Teriaca, L., Solanki, S. K., The quiet-Sun average Doppler shift of transition regions and coronal lines up to 2 MK (Oral), IMPRS S3 seminar, Katlenburg-Lindau, Germany, 15. Juni (2011)

- **Dadashi, N.**, Teriaca, L., Solanki, S. K., The quiet Sun average Doppler shift of TR and coronal lines up to 2 MK (Poster), 4th SOLAIRE Network Meeting, Teistungen, Germany, 9.-13. Mai (2011)

- **Dadashi, N.**, Teriaca, L., Solanki, S. K., The average Doppler shift of coronal lines on the quiet Sun (Poster), Hinode-4 meeting, Palermo, Italy, 11.-15. Oktober (2010)

- **Dadashi, N.**, Teriaca, L., Solanki, S. K., The average Doppler shift of solar transition region and coronal lines (Oral), IMPRS S3 seminar, Katlenburg-Lindau, Germany, 25. November (2009)

Contents

Summary

Imaging and spectroscopy at vacuum ultra-violet (VUV: 100 to 2000 Å) wavelengths are the key tools to study the outer solar atmosphere. This is a very dynamic environment where structures and their changes can be observed down to very small scales. However, it also shows average properties that must be accounted for by any reliable modelling effort. The average Doppler shift shown by spectral lines formed from chromosphere to corona, in particular, reveals important information on the mass and energy balance of the solar atmosphere, providing a tight observational constraint on any model of the solar corona. So far, spectroscopic studies revealed a persistent average red shift of the lines formed at temperatures below 0.5 MK that revert to blue shift at higher temperatures. However, for temperatures above 1 MK the behaviour was, so far, unknown.

Since VUV radiation is entirely absorbed by the atmosphere of the Earth, it can only be detected with instruments operating in space. In this thesis I have used simultaneous and co-spatial VUV spectra recorded by two spectrometers: SUMER (Solar Ultraviolet Measurements of Emitted Radiation)/SoHO (Solar and Heliospheric Observatory) and EIS (Extreme ultraviolet Imaging Spectrometer)/Hinode. The behaviour of the absolute Doppler shift versus temperature (up to 2 MK) is measured by using a novel technique developed during this thesis work and applied to the quiet Sun near disk center and to the moss area of an active region. The results are compared with different coronal models present in the literature.

Lines with formation temperatures between 1 to 2 MK are formed to be blue shifted in the quiet Sun, i.e. showing upflows. As the temperature increases, the amount of the upward motion increases from a value of (-1.8 ± 0.6) km s^{-1} around 1 MK (Mg x and Fe x formation temperature) to a maximum of (-4.4 ± 2.2) km s^{-1} at Fe xiv formation temperature (1.8 MK). At even higher temperatures the value of the upward motion decrease to (-1.3 ± 2.6) km s^{-1} at 2.1 MK (formation temperature of Fe xv). These results are in good agreement with the predictions of 3-D MHD numerical models considering the braiding and stressing of the magnetic fields that are produced by the photospheric motions as well as episodic heating events occurring in the chromosphere (e.g., Hansteen et al. 2010).

The Doppler shift measurements over the moss area of an active region (the area at the footpoints of the 3 to 5 MK hot loops forming at the core of active regions) show almost constant blue shifts (upflows) of about (-5 ± 2) km s^{-1} for the temperatures of 1 to 1.6 MK (Formation temperatures of Fe x to Fe xiii). The strength of the upflows decreases to 1 km s^{-1} for hotter lines up to 2.1 MK (Fe xiv and Fe xv). The near zero flow velocities at the footpoints of the hot loops, the fact that line profiles in the moss are symmetric (no evidence of unresolved high speed plasma flows), and the observations that the plasma seems to accelerate as it moves up along the loop legs, suggest that the heating in the hot

core loops of active regions is prevalently occurring in a quasi-steady manner.

The first Chapter contains a brief introduction to the problem that is investigated in this work. Chapter 2 introduces the instruments that are used in the work and Chapter 3 describes the data reduction process for each instrument. Chapters 4 and 5 present the results of the work on the quiet Sun and active region moss and provide a discussion. These results have been published in a refereed journal (Dadashi et al. 2011, 2012).

1 Introduction

The temperature in the core of the Sun, where the nuclear reactions happen, is about 15 MK. As one goes through the core toward the surface of the Sun, the temperature essentially drops to about 5700 K, at the visible surface of the Sun or photosphere. Heat transfer inside the Sun is easily understood in terms of radiative transport (from the core up to 0.7 solar radii) and, at greater radial distances, by convection up to the photosphere. However, if one goes away from the surface of the Sun, the temperature of the atmosphere increases dramatically by a factor of about 200 and reaches a few million Kelvin in the corona. This phenomenon cannot be explained by heat transfer processes (thermal conduction, thermal convection, and thermal radiation). In fact, in the solar corona they either do not play a role (convection) or act as cooling agents.

If thermal conduction would be the only mechanism responsible for the heat transfer in the solar atmosphere, the temperature would drop continuously as one gets far from the solar surface. A hot corona over a cooler photosphere produces a downward heat flux that acts as a cooling agent that must be balanced. Moreover, radiation escaping the atmosphere of the Sun (e.g., VUV emission) and solar mass flows (e.g., solar wind and eruptive events such as CMEs, flares, and prominences) cause extra losses of energy (and mass). The total energy loss is of about 10^7 ergs cm^{-2} s^{-1} in the active regions and 3×10^5 ergs cm^{-2} s^{-1} in the quiet Sun (Withbroe and Noyes 1977, Walsh and Ireland 2003). If not compensated, the continual loss of energy (and mass) would make the corona disappear in a couple of hours or days (Aschwanden 2004). Since it does not happen, there must be process(es) depositing energy (and supplying mass) to the corona.

This problem is called *"coronal heating problem"* and its origin can be traced back to the work of Grotrian (1939) and Edlén (1942). They realized that the unknown coronal emission lines observed during the total solar eclipses were not signatures of the presence of a new element in the corona, the so called *"coronium"*, but that of known elements (like iron, calcium, and nickel) in their high states of ionization. This means that the coronal environment must be at very hot temperatures (millions of degrees). Finding and identifying the physical mechanism(s) responsible for heating the corona of the Sun (and of Sun-like stars) up to millions of degrees is one of the big puzzles in astrophysics that does not have a definitive solution, yet.

Several models have been proposed to solve this problem. The first solar atmospheric models developed in the 1950s were based on gravitational stratification. Left panel of Figure 1.1 shows a simple sketch of these models (from Schrijver 2001, Aschwanden et al. 2001). These traditional models divided the atmosphere of the Sun into four layers or parallel shells:

- Photosphere: defined as the apparent surface of the Sun at visible wavelengths.
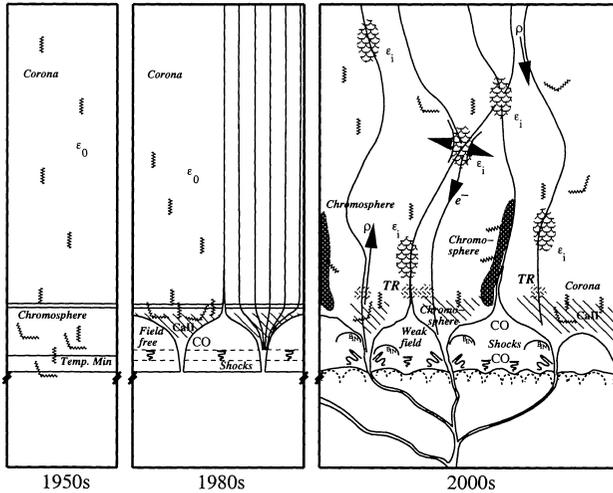
Figure 1.1: Solar atmosphere models developed since 1950s (from Schrijver 2001).

More precisely, the height in the atmosphere where opacity at 5000 Å is equal to one ($\tau_{5000} = 1$). The photosphere has an effective (equivalent to a black body) temperature of 5780 K.

- Chromosphere: right above the photosphere there is an irregular reddish layer visible with the naked eye during the total solar eclipses. The density decreases and the temperature increases with increasing distance from the base of this layer. At the top of the chromosphere the temperature reaches ≈ 20000 K. This high temperature causes the hydrogen atom to emit the red-pinkish coloured light of Hα (6563 Å, the first line of the Balmer series) emission.

- Transition region (TR): the thermal interval between the relatively dense and cold chromosphere (T $\approx$ 20000 K) and hot corona (T $\approx$ 1 MK). Vernazza et al. (1981), using a simple Semi-empirical 1-D model of the solar atmosphere under quiet Sun conditions, predicted a thickness of less than 100 km for this layer. Fig. 1.2 (adopted from Peter 2004) shows the average temperature and density behaviour for the solar atmosphere. As the temperature increase, the constituents of the atmosphere changes from neutral atoms to few to several times ionized atoms. Some of these ionized atoms formed in the transition region are C III-IV, O III-VI, Si III-VI, N III-V (Fig. 1.2). These ions emit light almost entirely in the ultraviolet part of the solar spectrum and therefore can only be studied from space.

- Corona: the outer layer of the solar atmosphere. It is visible as a glowing crown around the Sun during solar total eclipses or by using coronagraph telescopes that block the emissions coming from the surface of the Sun. The temperature rises to few million Kelvin in this layer and therefore it is made of highly ionized atoms that emit light mostly at VUV and X-ray wavelengths.
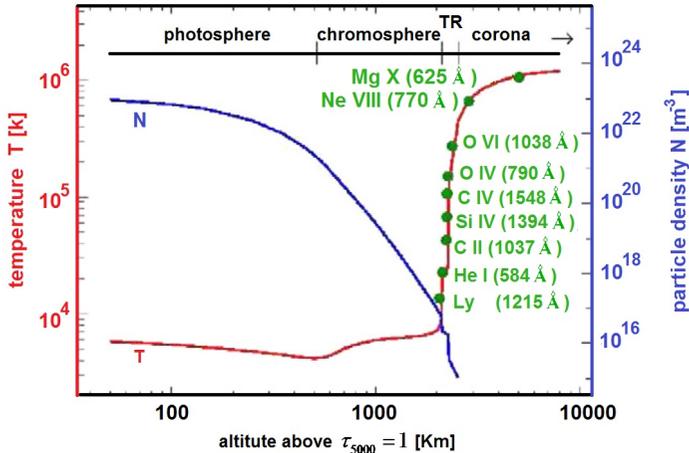
Figure 1.2: Temperature and density structure of the Sun's atmosphere with respect to height in a 1-D model. The density decreases and the temperature increases with increasing distance from the surface of the Sun ($\tau_{5000} = 1$). At the top of the chromosphere temperature reaches 20000 K. Passing through a very thin layer called transition region (TR), the temperature rises by a factor of 100 and keeps increasing afterward in the corona. Some of the ions that are forming at transition region temperatures are shown in the figure (from Peter 2004, Tian et al. 2010).

However, at the time these early models were constructed, in the 1950s and 1960s the details of the structure of the atmosphere of the Sun were still unknown. It was possible to perform ground-based observations of photosphere and chromosphere, but for the hotter transition region and corona, the emission lines are mainly located in the range of vacuum ultra-violet (VUV:100 to 2000 Å) and became accessible only after the advent of the space era. Space missions, such as NASA's Skylab (1973-1974), started providing a more detailed view of the coronal structures (such as active region loops and coronal holes, Aschwanden et al. 2001). The mass flows in the transition region, for instance, were observed for the first time by Doschek et al. (1976) using Skylab and later on by the NASA Solar Maximum Mission (1980-1989) and a few other rocket experiments (e.g., Hassler et al. 1991). Therefore, by the 1980s, models were trying to consider the large scale magnetic structures and the presence of quasi-steady flows.

During the 1990s, the very successful SOHO[1] and TRACE[2] space missions, revealed the much more complicated and fine structures of the atmosphere of the Sun. Many types of mass flows (ejection of spicular and flare materials, siphon flows, draining of coronal material, flows in the individual loops, etc.) and magnetohydrodynamic transversal plasma waves were detected. Later on, in the 2000s, Hinode[3], and SDO[4] revealed even more detailed structures and dynamics. The classical layers of the atmosphere of the Sun (photosphere, chromosphere, transition region, and corona) were distinguished more by temperature than by geometry. The right panel of Fig. 1.1 shows a sketch of this complex scenario. For instance, the height of the chromosphere in areas with open magnetic field lines (like coronal holes) could be higher than the height of the transition region in the closed magnetic field regions (like quiet Sun or active region, Tian et al. 2010). It seems that most probably there are different heating mechanisms operating over the different energy ranges in the different coronal structures (such as quiet Sun, coronal holes, different classes of loops in active regions) but which one dominates is still unknown (Walsh and Ireland 2003, Klimchuk 2006).

Theoretical models of coronal heating were developed during these decades to better reproduce the new observation results from the above mentioned space missions. However, this has not been an easy task since the observations actually provide (line-of-sight integrated) measurements of physical parameters, such as temperature, density, and flow speed, while the older theoretical models are often described in terms of spatially resolved physical parameters like vertical and azimuthal magnetic field components, currents, resistivity, viscosity, turbulence, waves and etc. (Aschwanden 2004). In general, a realistic theoretical model of coronal heating must include several steps like determining the energy source(s) that cause(s) the heating, determining the response of the plasma to the heating, and foresee the final radiated spectrum out of the model. Since each of these steps has its own difficulties, limitations and errors, most of the existing coronal heating models focus only on certain steps. For instance, 1-D hydrostatic models (loop models) do not care about the physical origin of the heating and instead focus on the response of the plasma to the heating. On the other hand, multi-dimensional MHD[5] models mainly focus on the responsible mechanisms of converting energy to heat and do not take the response of the plasma and the produced radiation into account in such detail (Klimchuk 2006). A comprehensive model should take all these aspects into account since what the observer observes in the end is the radiation emerging from the corona. Good reviews of these models are given by Walsh and Ireland (2003), Aschwanden (2004), Klimchuk (2006).

Only recently, some 3-D comprehensive numerical models of the solar atmosphere from the photosphere to corona could provide a measure of the mentioned observed physical parameters[6] (e.g., Gudiksen and Nordlund 2002, Peter et al. 2004, 2006, Hansteen et al. 2010). There have been lots of measurements on quantities like densities and temperatures of the transition region and corona (e.g., Pérez et al. 1999, Del Zanna and

---

[1]Solar and Heliospheric Observatory, an ESA/NASA collaboration launched in 1995.
[2]Transition Region And Coronal Explorer, launched in 1998 by NASA.
[3]JAXA/NASA/PPARC mission launched in 2006.
[4]NASA's Solar Dynamic Observatory launched in 2010.
[5]Magneto-Hydro-Dynamics
[6]such as flows, densities, temperatures, etc.

Bromage 1999, Chae et al. 2002, Tripathi et al. 2008, Buchlin and Vial 2009, Warren and Brooks 2009, Magdalenic and Marque 2010, Muglach et al. 2010, Winebarger et al. 2011, Wilhelm 2012). However, due to limitations in the observed wavelength ranges (resulting in limited temperature coverage), spectral resolution, and available wavelength calibration, measurements of flow velocities at coronal temperatures were missing. Since velocity behaviour of the flows with respect to the formation temperature is one of the physical parameters that can be estimated theoretically by the newly developed 3-D models, having an accurate measurements of this quantity will help to put observational constrains on the existing models or improve them to achieve a more realistic view of the structures of the solar atmosphere. In this thesis work, using simultaneous spectroscopic observations from SUMER[7] and EIS[8] spectrometers, and a novel technique that was developed as part of this thesis work, I have measured the absolute Doppler shifts of transition region and hot coronal lines over a quiet Sun and a moss area in an active region.

In the following parts of this Chapter, there is first an introduction to the Doppler shift measurements and then an introduction to the VUV part of the solar spectrum. Afterward, there is a short introduction to the different features of the solar atmosphere. Then, the prevalent net red shift puzzle of the solar transition region and the possible models to explain this phenomenon are described and, finally, there is a Section about *"moss"* structures in active regions and the importance of studying the physical characteristics of such structures to distinguish between the different heating mechanisms that have been proposed for the hot loops rooted in moss areas.

1.1 Doppler shift measurements

As described by Mariska (1992), if the size scale of the motions of the plasma are larger than the spatial resolution of the observers' spectrometer, then the whole line profile will shift toward longer or shorter wavelengths depending on the direction of the plasma motion with respect to the observer. Therefore, accurate Doppler shift measurements could give a direct estimate of the plasma velocity component along the line-of-sight (LOS) in the transition region and corona. The plasma speed along the line-of-sight (v_{LOS}) is obtained as:

$$v_{LOS} = \frac{\lambda - \lambda_0}{\lambda_0} c \qquad (1.1)$$

where c is the speed of light in vacuum, λ is the observed wavelength, and λ_0 is the wavelength of the atomic transition producing the line when the emitting atom and the observer are at rest respect to each other (rest wavelength). Measuring the rest wavelength of highly ionized atoms in the laboratory one needs to produce very high temperatures (usually through a discharge) resulting in broad (and generally weak) profiles. Thus, the rest wavelength measurements obtained in this way are characterized by relatively large errors. On the other hand, for an emission line with $\lambda = 200$ Å, a measurement of the line position with accuracy of ±0.01 Å results in a ±15 km s^{-1} velocity error. For the VUV lines that are observable in the solar atmosphere against cool lines (whose rest wavelengths are well measured) there is a better way to obtain their rest wavelength by

---

[7]described in Section 2.1

[8]described in Section 2.2

using off-limb observations (e.g., Peter and Judge 1999). In general, it should be noticed that the problem of the large errors in λ_0 can be largely circumvent if the quantity $(\lambda - \lambda_0)$ is directly measured. This is one of the main advantages of the technique developed during this thesis work. It should remembered that, for spectra acquired at disk center, the observed blue shifted profiles correspond to upflows[9] and the red shifted profiles are signatures of downflows[10].

1.2   Solar VUV radiation

The VUV part of the spectrum covers the wavelength range between 100 and 2000 Å, while the **E**xtereme **U**ltra**v**iolet portion of the electromagnetic spectrum (**EUV**) is covering the range of 100 to 1200 Å. The solar VUV spectrum contains a lot of bright emission spectral lines (Curdt et al. 2001, Wilhelm et al. 2004, Young et al. 2007a) that are produced by the atomic transitions from neutral and ionized atoms. These lines form in the temperature range of 0.01 to 20 MK in the chromosphere, transition region, corona, and solar flares (Wilhelm et al. 2004). A review of past VUV instruments and the achieved results is given by Wilhelm et al. (2004) and Aschwanden (2004).

Figure 1.3 shows the VUV range of the solar spectrum (adopted from, Heroux and Hinteregger 1978). Overplotted on this graph, there are a light blue and two light red regions. The first one shows the wavelength coverage of SUMER/SoHO and enables us to study the chromosphere, transition region, and the cooler part of the corona[11] and the two light red ones show the wavelength coverage of EIS/Hinode that provides the opportunity to study hot coronal lines.

1.3   Regions of the solar atmosphere (AR, QS, CH)

As mentioned earlier, the solar atmosphere is highly structured in both vertical and horizontal directions and is highly variable with time. However, it is also differentiated in large-scale regions that are the result of the different strength and polarity distribution of the magnetic field. In general, three different types of regions are distinguishable, particularly when observing at VUV wavelengths:

- AR: Active regions are the sites of intense emission associated with strong, mostly closed, magnetic fields. In the optical wavelength, sunspots are seen in these areas. The strength of the photospheric magnetic fields in these areas can reach up to a few kilo Gauss (in the Sunspot umbrae). The magnetic field is structured in a bipolar pattern in the low corona. The typical field strength is hundred to few hundred G.

- QS: Quiet Sun regions look fainter with respect to ARs while viewed in the EUV and are mostly associated with closed weaker ($\approx$ 20 G in corona) magnetic field lines. The magnetic field (and the VUV emission) is concentrated along the edges

---

[9]Flows that are moving away from the surface of the Sun.

[10]Flows that are moving toward the surface of the Sun.

[11]It should be noticed that there are also lines from highly ionized atoms that become visible only during flares or high energy events.
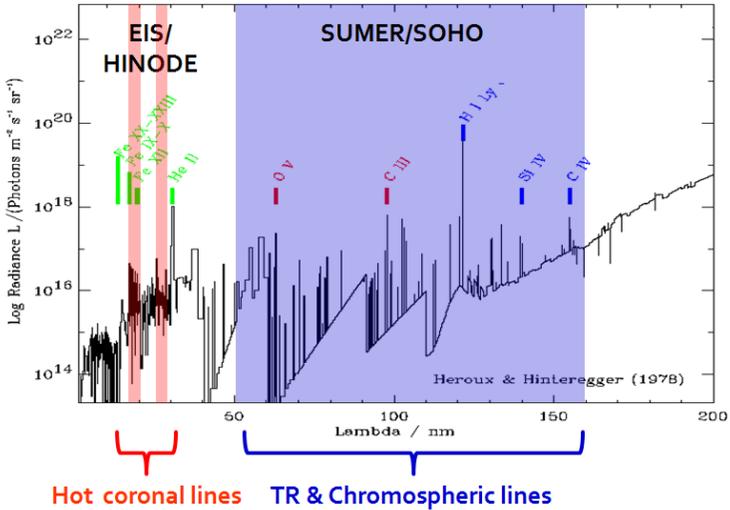
Figure 1.3: The solar reference spectrum for solar UV below 2000 Å from Heroux and Hinteregger (1978). Overplotted light blue region represents the wavelength coverage of SUMER/SoHO spectrometer, while the overplotted light red regions represent the wavelength coverage of EIS/Hinode spectrometer.

of the supergranular cells, where the field is advected by convection. Opposite magnetic polarities are distributed relatively randomly among the magnetic features.

- CH: Coronal holes are the source of the fast solar wind (≈ 800 km s^{-1} terminal speed at 1 AU[12], Krieger et al. 1973). They are the dark areas (weaker emissions with respect to QS area) at coronal temperatures mostly concentrated at solar poles (polar coronal holes) but also occurring at lower latitudes (equatorial coronal holes). The magnetic field has a prevalent polarity (it is unipolar) and, thus, the magnetic field lines are mostly open.

The left panel of Fig. 1.4 shows an EUV image of the Sun taken in the Fe ix-x 171 Å channel of AIA/SDO on 4 July 2011 at 16:40:5 UTC. Right panel shows a magnetogram of the Sun recorded by HMI/SDO very close in time (16:35:15 UTC). Active region, quiet Sun, and coronal holes are marked in both panels. White and black patches in the magnetogram show the two different polarities. The brightest and darkest shades show the stronger line-of-sight (LOS) component of the magnetic field.

In this thesis work, we have investigated the flows on the quiet Sun and an active region. The general behaviour of the Doppler shift versus temperature looks to be the

---

[12]Astronomical unit: average distance between the Earth and the Sun
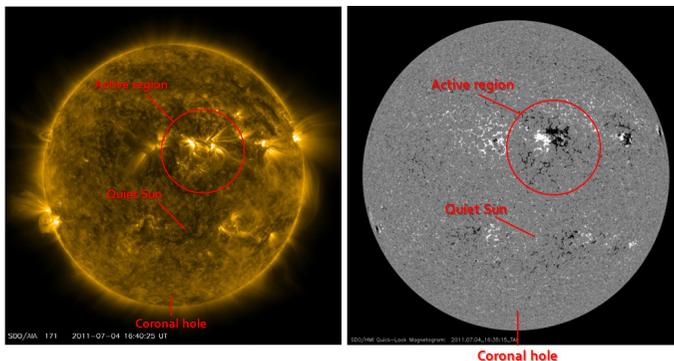
Figure 1.4: The left panel shows an EUV image of the Sun from the 171 Å channel of AIA/SDO on 4 July 2011 at 16:40:5 UTC. Right panel shows a magnetogram of the Sun recorded close in time (16:35:15 UTC) on the same day with HMI/SDO. Active region, quiet Sun, and coronal holes are marked on both panels.

same over these two areas. However, our results show the flows in the active region to be stronger than in the quiet Sun. Results of the flow measurements in the quiet Sun and active region moss are presented in Chapters 4 and 5, respectively. Unfortunately, because of the low signal to noise ratio of the Mg x 625 Å (which is observed by SUMER/SoHO), practically it is not possible to use our technique to measure the velocity of the flows of hot coronal lines over the coronal hole regions.

1.4 Transition Region prevalent red shift

The observations provided by the satellites launched in 1990s (e.g., SoHO[13] and TRACE[14]) fully revealed the dynamic nature of the transition region. Therefore, continuous changes at both small and large scales are going on in the solar atmosphere and any attempt to model the heating of the solar atmosphere should consider this dynamic behaviour.

Despite this dynamic nature of the transition region, an average net red shift or downward motion is detected for emission lines (e.g., C iv, O iv, and N v) forming at transition region temperatures in the quiet Sun around disk center since the launch of SO82B/Skylab[15] spectrograph (Doschek et al. 1976). Later on, other VUV spectrometers (HRTS[16], UVSP/

---

[13]The ESA/NASA Solar and Heliospheric Observatory
[14]The NASA's Transition Region and Coronal Explorer
[15]The first NASA's space station launched in 1973.
[16]The NRL's High Resolution Telescope and Spectrograph (HRTS). First rocket flight launched in 1975.

SMM[17], LASP[18], and SUMER/SoHO[19]) observed and confirmed this phenomenon (Gebbie et al. 1981, Brueckner and Bartoe 1983, Brekke 1993, Achour et al. 1995, Brekke et al. 1997, Chae et al. 1998, Brekke 1999, Peter and Judge 1999, Dammasch et al. 1999a,b, Teriaca et al. 1999a).
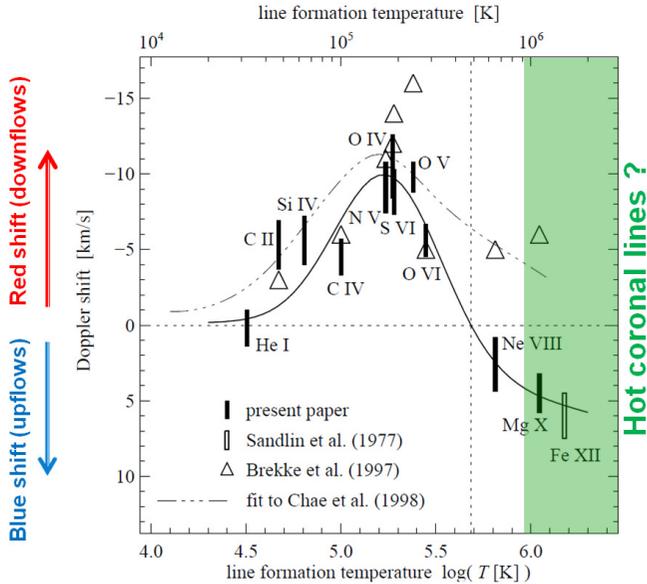
Figure 1.5: The variation of the Doppler shift versus temperature at disk center (adopted from Peter and Judge 1999). Unlike the rest of this thesis work, only in this plot, blue and red shifts or upward and downward motions are represented with positive and negative velocity values, respectively. The solid line demonstrates a by-eye fit to the Doppler shifts of the lines studied by Peter and Judge (1999). The light orange coloured area is the temperature range of our interest. The different values reported for Ne VIII and Mg X are due to a different choice of the rest wavelength by the different authors. See Section 3.1.4.6.

In general, the amount of the red shift increases as we go toward hotter lines (starting at chromospheric temperatures), and reaches maximum velocities of 10 to 15 km s^{-1} in the quiet Sun at temperatures of about 0.2 MK. As the temperature increase further, the Doppler shift decreases. However, determining the rest wavelength of the lines formed

---

[17]The Solar Maximum Mission (SMM) was launched in 1980.

[18]EUV coronal spectrometer aboard Laboratory for Atmospheric and Space Physics (LASP) an American mission launched with a sounding rocket 1987.

[19]Will be described in Section 2.1.

at high temperatures is technically difficult and associated with large uncertainties. A detailed discussion of this issue can be found in Section 3.1.4.6. Figure 1.5, from Peter and Judge (1999), shows the Doppler shift with respect to line formation temperature. Measurements of Brekke et al. (1997) are also overplotted in the graph. The importance of choosing a correct rest wavelength in obtaining Doppler shifts is apparent. The area coloured in orange shows the lack of the Doppler shift measurements in hot coronal lines that are investigated in this PhD thesis.

Going back to the prevalent average red shift of transition region lines, we have to note that such strong mass flux of downward motions is enough to empty the whole corona within an hour (Kjeldseth-Moe 2003). Therefore, there should be some mechanism(s) that balance this huge mass flux. In the following, the suggested physical models to explain such average net red shifts of the transition region lines (such as, siphon flows, return of the spicular material, upward propagating waves, downward propagating acoustic waves, and 3D comprehensive models of the Sun's atmosphere) are introduced. The comparison of our results with the predictions of these models are discussed later in Chapters 4 and 5.

1.4.1   Siphon flow models

The prevalent average red shift of TR lines could be caused by siphon flows in coronal loops. There are several possible causes for siphon flows (e.g., driven by a pressure difference between the two photospheric footpoints of the loops (Noci 1981), or by asymmetric heating (Boris and Mariska 1982, McClymont and Craig 1987), or via an asymmetric loop cross section (Mariska and Boris 1983)). Most likely are uni-directional siphon flows. In this case, the extra pressure at one footpoint of the loop drives an upflow that moves along the whole loop length and falls back toward the photosphere at the opposite footpoint (Fig. 1.6).
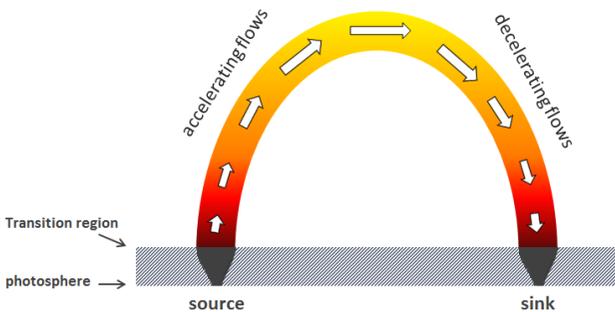

Figure 1.6: A simple sketch of a uni-directional siphon flow with constant cross section, driven by the pressure difference at different footpoints of the loop (Aschwanden 2004).

Using a siphon flow model Boris and Mariska (1982) obtained downflows at TR tem-

peratures (T$\approx 10^5$ K) with velocities less than 1 km s^{-1}, while Mariska and Boris (1983) at the same temperature obtained maximum velocities of 4 km s^{-1}. McClymont and Craig (1987) studied a siphon flow in cool coronal loops (T$\approx 10^6$ K) driven by a strong asymmetric heating in the loop. This asymmetry causes the plasma inside the loop to evaporate and drain at the other leg of the loop. They obtained a maximum velocity of 6.4 km s^{-1} at 10^6 K. These kinds of models are able to qualitatively explain the net red shift phenomenon in TR emission lines, but the strengths of the obtained downflows are much smaller (except in the cases of very large asymmetries) than the observed ones.

Mariska (1988) applied a time dependent asymmetry to the loop model and computed UV emission line profiles. He obtained both red shift (5 to 8 km s^{-1} in cooler TR lines such as O III, C IV, and O IV) and blue shift (18 to 24 km s^{-1} for hotter TR lines like O V and O IV). The obtained Doppler shifts for hotter TR lines (T $\approx$ 2 to 3×10^5 MK) is obviously not consistent with the observations. Spadaro et al. (1991) added the effect of non-equilibrium ionization to the model of Mariska (1988). This model produces smaller red and blue shifts, which are still in disagreement with the observations.

1.4.2   Spicule models

One of the earliest ideas to explain the red shift was emission from downflowing and cooling plasma that had been previously heated and injected to in the corona by spicules (Pneuman and Kopp 1978, Athay and Holzer 1982, Athay 1984). Using observations from the Solar Optical Telescope aboard Hinode, De Pontieu et al. (2007) claimed that there are two types of spicules. Figure 1.7 shows a cartoon of spicules type I and type II:

- Type I: or the classical spicules described by Beckers (1968), Pneuman and Kopp (1978). They are thin jets of gas (in the network) rising from the cool chromosphere toward the corona. They are usually observed in Hα at heights of 6 to 10 Mm. The spicules are cold (with temperatures of 10000 K) with respect to their sourrounding enviroment (Pneuman and Kopp 1978). Type I spicules have life times of 3 to 10 minutes with speeds of 20 to 30 km s^{-1} (Beckers 1968). There is no observational evidence that proves that this type of spicules could reach coronal temperatures.

- Type II: highly dynamic small (finger-like) and thin (about 200 to 300 km width) jets of chromospheric cool plasma with speeds of 50 to 150 km s^{-1} and shorter life times of 10 to 150 s (De Pontieu et al. 2007, 2009, McIntosh and De Pontieu 2009b). Unlike type I spicules, there is some evidence that parts of the cool mass inside the type II spicules are heated up to coronal temperatures during their ejection (De Pontieu et al. 2011, Zhang et al. 2012).

Pneuman and Kopp (1978), Athay and Holzer (1982), Athay (1984) estimated that spicules carry a very large upward flux (10^{15} atoms cm^{-2} s^{-1}) which is almost 100 times larger than the solar wind measured flux at 1 AU. Therefore, most of the material ejected upward by spicules must have returned back to the chromosphere. Pneuman and Kopp (1978) and Athay (1981) used this picture to argue that return of the spicular material is the source of the net average red shift (downflows) observed in the transition region quiet Sun. Since the returned spicular material are not seen in Hα images, but at transition region temperatures, therefore the returning plasma should be hotter than spicules themselves.
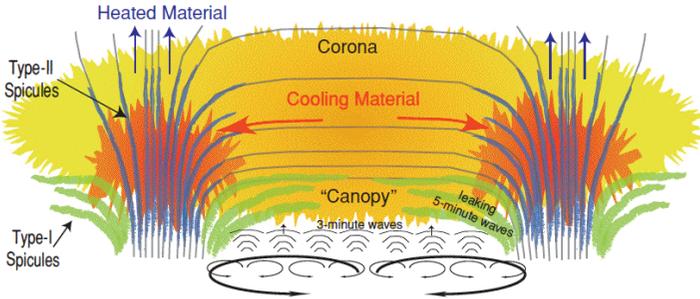
Figure 1.7: Spicule type I and type II (courtesy of McIntosh and De Pontieu 2009b).

Numerical calculations of this model by Mariska (1987) could not obtain the observed red shift values Moreover, the classical spicules model does not show any blue shift (upflows) signatures in the hotter lines. Therefore, people came to the conclusion that this theory cannot be the only mechanism responsible for the red shifts.

The recent discovery of the type II spicules (De Pontieu et al. 2007) and claims of observational evidence that they could reach coronal temperatures, revived interest in spicules as possible suppliers of heat and mass to the corona (De Pontieu et al. 2009, McIntosh and De Pontieu 2009b, De Pontieu et al. 2011).

1.4.3   Nanoflare (impulsive) models

Models driven by nanaflares are listed and introduced in the following Subsections.

1.4.3.1   Upward propagating waves

Upward propagating waves or rebound shock model for spicules, was another proposed mechanism to explain the TR red shifts. A shock train, which is produced by impulsively released energy at photospheric heights, propagates upward in the spicule and push the plasma upward and heats it to transition region temperatures. Cheng (1992) found that this model can produce average downward motions (red shifts). However, Hansteen and Wikstol (1994), considering that the line emission varies with time and position, demonstrated that the hydrodynamic evolution results in upflows (blue shifts) at transition region temperatures.

1.4.3.2   Downward propagating acoustic waves

Hansteen (1993) suggested that energy released near the top of coronal loops by nanoflares could generate downward propagating acoustic waves that move along the loop legs toward and through the transition region. He calculated the effect of this perturbation on the transition region and low coronal emission lines, finding red shifts for transition region

lines (e.g., C IV and O VI , but smaller than the observed ones) and small blue shifts for coronal lines (e.g., Ne VIII).

1.4.3.3 MHD wave models

Later on, Hansteen et al. (1997) added to the downward propagating acoustic waves model, the effect of downward propagating MHD waves along the loop leg from the corona toward the chromosphere. They found a larger red shift of 15 and 7.5 km s^{-1} for transition region C III and C IV lines, respectively. On the other hand the blue shifts of the coronal lines (e.g., Mg IX) became very large (15 km s^{-1}). Some observational support to downward propagating waves was produced by Judge et al. (1998).

1.4.4 3-D comprehensive models of the Sun's atmosphere

Gudiksen and Nordlund (2002), Peter et al. (2004, 2006) have developed a three dimensional MHD numerical model from photosphere to corona and produced the synthesized spectra of the coronal emission lines. In their models, the photospheric motions cause the magnetic field lines to get braided and produce currents. Dissipation of these currents heat the corona. Figure 1.8 shows a comparison between the Doppler shifts out of thier models and the observations. They obtained red shifs at transition region temperatures but also red shift (though smaller), in the low coronal lines.
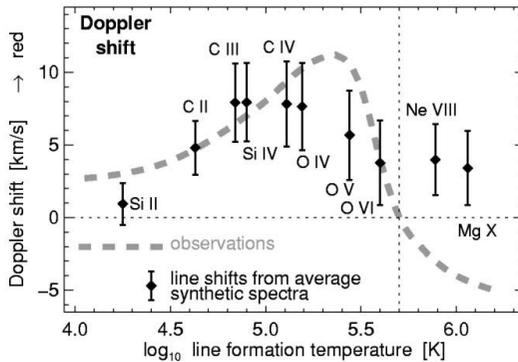
Figure 1.8: Variation of Doppler shifts with respect to temperature in the quiet Sun. The dashed line shows the observational results and the black diamonds shows the synthesized one (Figure is taken from Peter et al. 2004). Their result is in good agreement with observations of transition region lines, but not for coronal lines.

Hansteen et al. (2010) added the effect of injection of emerging magnetic flux to the model of Peter et al. (2006). By introducing rapid episodic heating to a layer between the

top of the chromosphere[20] and the corona[21] in their B1 model (with unsigned magnetic field of 75 G), they obtained a red shift for transition region temperatures and increasing blue shifts (with increasing coronal temperatures) for coronal lines (e.g., Si VII and Fe XII). However, for their hottest synthesized line (Fe XV), they found only a small red shift. The result of their synthesized line shifts are overplotted with red squares on our measured Doppler shifts in the quiet Sun (Fig. 4.8, Chapter 4). In the summary and conclusions Sections of Chapter 4 there are detailed discussions and a comparison between my observation results and the models.

1.5   The footpoint of hot coronal loops: moss

Active regions are the brightest regions (in the VUV and X-ray wavelength ranges) with quite long life times (up to several solar rotations). Figure 1.9 shows the typical structures of an active region (Ugarte-Urra et al. 2009, Viall and Klimchuk 2011):

- **Core region**: contains hot plasma loops with formation temperatures larger than 2 MK (Warren et al. 2010). The AIA/SDO 211 and 335 channels show this region nicely.

- **Warm coronal loops**: these loops surround the core area and have temperatures of about 1 MK (Klimchuk 2006, Warren et al. 2010). The AIA/SDO 171 channel shows these extended warm loops clearly.

- **Warm fan loops**: they are usually found at the edges of active regions and only their legs are visible (<1 MK) (Schrijver et al. 1999, Ugarte-Urra et al. 2009, Young et al. 2012). Like warm coronal loops, this fan loops are visible in AIA/SDO 171 channel.

- **Background emission**: the diffuse emission in the background of every active region observable in all Channels of AIA/SDO. This area does not have any special loop like structures (Klimchuk 2006, Viall and Klimchuk 2011).

- **Moss region**: defined as emission from the footpoints of hot core loops (Berger et al. 1999, Martens et al. 2000, Tripathi et al. 2010a). It is observable nicely in AIA/SDO 193 channel.

It is still unknown whether all of these independent structures are the result of one unique mechanism or there are several different mechanisms responsible for generating them. There is convincing evidence that warm coronal loops are actually bunches of strands that are heated by impulsive events like nanoflares (Warren et al. 2003, Klimchuk 2006, 2009, Ugarte-Urra et al. 2009, Tripathi et al. 2009). On the other hand, the results for core loops are more contradictory. There is some observational evidence that supports impulsive heating and other that supports quasi-steady heating[22].

---

[20]Pressure scale height of chromosphere considered to be 200 km.
[21]Pressure scale height of corona considered to be 50 Mm.
[22]The appropriate references are given in the introduction Section of Chapter 5.
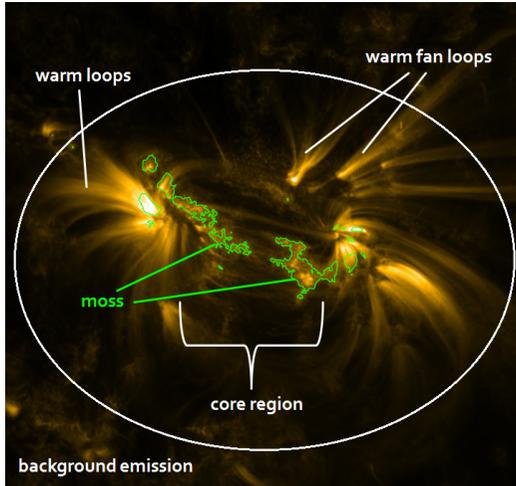
Figure 1.9: The components of active region (NOAA 11243) are shown in 171 AIA/SDO channel. Image taken on 4 July 2011 at 17:00 UTC. The loops filling the core regions are too hot to be visible in the 171 AIA/SDO channel.

Hot coronal loops look fuzzy. This was noticed since 1970s after the launch of Skylab but is was not clear whether this fuzziness is the nature of this hot loops or they just look like this because of the low spatial resolutions of our observing instruments. Recent studies seem to indicate that hot loops are intrinsically fuzzy (e.g., Tripathi et al. 2009). Whatever the truth is, this fuzziness makes the hot loops difficult to single out and study. On the other hand, the footpoint region of these loops, the *"moss"* area, is well visible and its dynamics can provide clues on the heating mechanism operating in hot loops.

The moss is best observed in images taken around Fe XII 195 Å and was described for the first time by Berger et al. (1999) using high resolution TRACE images of Fe IX/X 171Å. Figure 1.10 shows a contour of moss area overplotted on different EIS raster scan images of active region NOAA 10940 (from Warren et al. 2008).

According to Berger et al. (1999) the moss is a confined thin layer (with approximately 1 Mm thickness) that is located at heights of about 2 to 4 Mm above the visible surface of the Sun. They also concluded that while hot coronal loops (3 to 5 MK) cover the cool plage regions, the strong thermal conduction gradient causes the plasma to emit. In other words, the moss is the emission from the top of the transition region. They mentioned the spongy shape of the moss is because of the presence of cooler spicules that eject material upward (from the chromosphere toward the corona) in those regions (Fig. 1.11).

Using TRACE data Fletcher and de Pontieu (1999) found electron densities of 2 to 5 $\times$ 10^9 cm^{-3} at temperature of 1.3×10^6 K. Others (Tripathi et al. 2008, 2010a, Winebarger
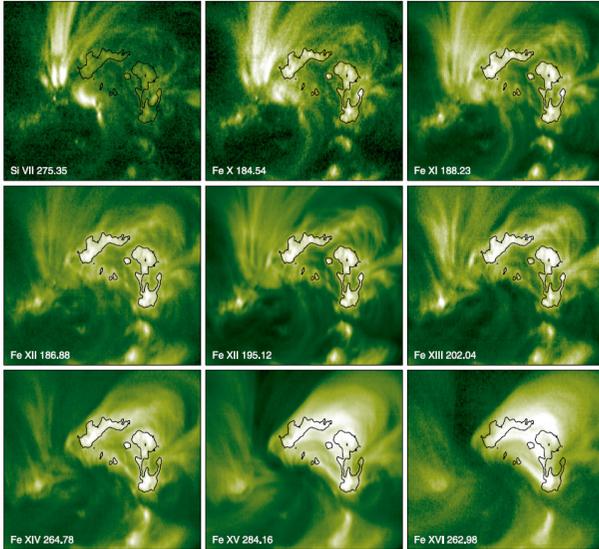
Figure 1.10: Intensity contours of Fe XII 186.88 Å (representing the location of moss) overplotted on EIS raster scans of active region NOAA 10940 in different ions with different formation temperatures (from Warren et al. 2008). The field of view is 196×178 arcsec^2.

et al. 2011) performed density measurements using different Fe XII emission line ratios and obtained larger densities of about 1 to 5×10^{10} cm^{-3}. However, this discrepancy was because of problems in the atomic data of CHIANTI for Fe XII. The problem is solved in the new version of the atomic data base (Del Zanna et al. 2012). Antiochos et al. (2003) studied the brightness and intensities over the moss and found changes in the moss intensity occurs very slowly (only 10 % after several hours). This means that the magnetic field in these regions does not change rapidly. Also the hot coronal loops look to be rooted in unipolar magnetic regions (Brooks et al. 2008). All these events appear to be indications of quasi-steady heating being prevalent in the hot loops.

On the other hand, there are some observations that support the nanoflare scenario as the responsible mechanism for heating in the moss region (Tripathi et al. 2010b, 2011, Viall et al. 2012, Tripathi et al. 2012). Therefore, more observations of moss characteristics (for instance absolute accurate Doppler shifts in the moss region) could provide clues in that issue. Chapter 5 gives more detailed information and discussion about the prevalent heating mechanism based on a recent absolute Doppler shift measurements by Dadashi et al. (2012).
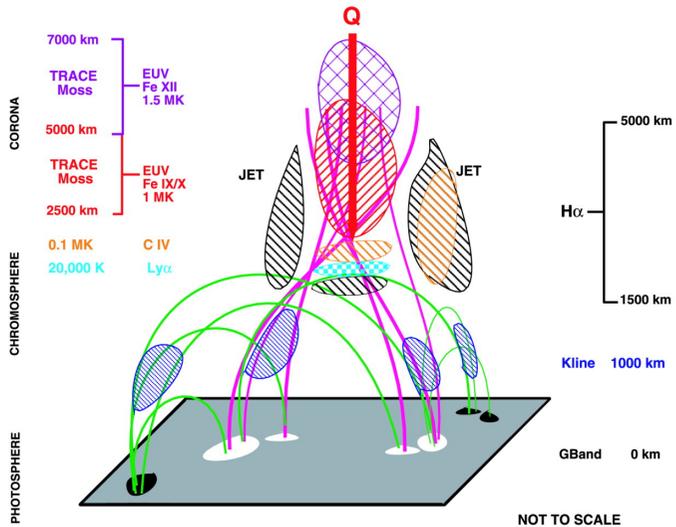
Figure 1.11: A cartoon that shows a snapshot of the whole solar atmosphere layers in an area close to a moss region (courtesy of De Pontieu et al. 2003). White and black patches in the gray phospheric plane show concentration of the magnetic field with different polarities. The green lines are closed magnetic field lines representing hot coronal loops. Looking in the direction of red arrow Q (that shows the conductive heat flux) the moss emission is observed in EUV emission (171 and 195 Å). Spicular jets producing the spongy shape of the moss are shown in the Figure.

2 Instruments

The Solar Ultraviolet Measurements of Emitted Radiation (SUMER) and Extreme ultraviolet Imaging Spectrometer (EIS), are two spectrometers that let us performe spectroscopic research on the solar transition region and corona. The SUMER wavelength range includes many bright transition region and cool coronal lines up to 1 MK, while EIS observes many bright coronal lines formed between 1 and 3 MK. Extreme ultraviolet Imaging Telescope (EIT) and Atmospheric Imaging Assembly (AIA), are two instruments that we have used to provide context images in transition region and coronal lines. This chapter gives a brief introduction of these instruments.

2.1 SUMER/SoHO

The SUMER, vacuum ultraviolet (VUV) spectrometer aboard the Solar and Heliospheric Observatory (SoHO) is designed to study the structures and associated dynamical processes occurring in the chromosphere, transition region, and low corona over the solar disk and off the limb in the inner corona. It has a broad wavelength range (from less than 500 to 1610 Å) and covers a temperature range from 6×10^3 to 2×10^6 K and above (Curdt et al. 2001, 2004) with a spatial resolution of 1 arcsec across the slit and 2 arcsec along the slit (since the spacecraft is located near the L1 point of the Sun-Earth system, 1 arcsec corresponds to 715 km on the Sun.) and temporal resolution down to 1 s.

SUMER was designed and built at the Max Planck Institute for Solar System Research (MPS[1]) with international cooperation from 1987 to 1995. This instrument is part of the SoHO (ESA/NASA) mission launched on 2nd December 1995 and inserted into its halo orbit around L1 on 14 February 1996[2]. The basic characteristics, capabilities and operations of SUMER are well described by Wilhelm et al. (1995) and Lemaire et al. (1997).

The high resolution observations of SUMER permit detailed spectroscopic diagnostics of plasma densities and temperatures in many solar features and have supported detailed studies of underlying physical processes such as plasma flows, turbulence and wave motions, diffusion transport processes, events associated with solar magnetic activity, atmosphere heating, and solar wind acceleration in the inner corona. Specifically, by measuring profiles and intensities of VUV lines, SUMER makes it possible to determine Doppler shifts and line broadenings with high accuracy. This kind of study is important to investigate the presence of any non-radiative mechanical heating mechanism that can reveal

---

[1]Former Max Planck Institute for Aeronomy (MPAE)

[2]The spacecraft is in the Halo orbit around the Sun-Earth Lagrangian point (L1, which is located on the sunward side of the Sun-Earth axis), about 1.5 million km from earth.
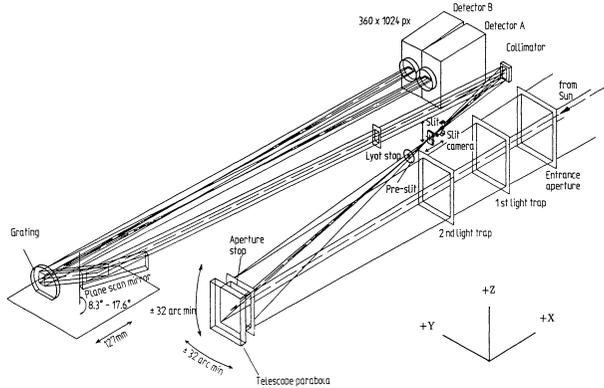
Figure 2.1: The optical design of the SUMER instrument aboard the SoHO spacecraft showing the extreme rays as they propagate through the system. The ranges of the movement of various mechanisms provided to control the positions of the optical components are indicated by arrows. The entrance door and its mechanism are not shown (figure taken from Wilhelm et al. 1995).

itself by velocity fluctuations.

The optical design of SUMER (see Figure 2.1) is based upon two parabolic mirrors, a plane mirror and a spherical concave grating, all made of silicon carbide (SiC) and mounted in an aluminium housing which serves as the optical bench. The first off-axis telescope parabola, which has pointing and scan capabilities of ± 32 arcmin in two perpendicular directions, images the Sun on the spectrometer entrance slit plane. The second off-axis parabola collimates the beam leaving the slit. This beam is then deflected by the plane mirror onto the grating. Two two-dimensional detectors (called A and B), located in the focal plane of the concave grating, collect the dispersed images of the spectrometer entrance slit. The center of detector A is located on the grating normal, while the center of the other detector is off by a quantity $\Delta = 70.4$ mm. Coverage of the full spectral range of the instrument requires a wavelength scan performed by rotating the plane mirror. A baffle system, consisting of an entrance aperture, light traps, an aperture stop, a pre-slit and a Lyot stop, completes the design. A brief summary of the basic SUMER optical characteristics is given in Table 2.1 below (Wilhelm et al. 1995, Teriaca 2001). By rotating the primary mirror in the east-west direction with steps of 0.3763 arcsec, SUMER rasters the selected area of the Sun, thus providing monochromatic images.

Of the two SUMER detectors (A and B), only one can be used at a time. Each detector has 1024 spectral pixels and 360 spatial pixels. When an exposure is taken, either the full (1024 pixels) spectrum, or selected spectral windows (25, 50, 256 or 512 pixels wide) are transmitted to the ground. The central area of the detectors is coated with a potassium

Table 2.1: SUMER optical characteristics (taken from Wilhelm et al. 1997)

Telescope		
	Focal length	1302.77 mm at 75°C
	Plate scale in slit plane	6.316 μm arcsec^{-1}
	Smallest step sizes	0.3763 arcsec
	(N-S and E-W)	
Slits		
	1	4×300 arcsec^2
	2	1×300 arcsec^2
	3	1×120 arcsec^2 (top)
	4	1×120 arcsec^2 (centered)
	5	1×120 arcsec^2 (bottom)
	6	0.3×120 arcsec^2 (top)
	7	0.3×120 arcsec^2 (centered)
	8	0.3×120 arcsec^2 (bottom)
Spectrometer		
	Wavelength ranges	
	Detector A[*]	330 - 805 Å (2nd order)[**]
		660 - 1610 Å (1st order)
	Detector B	330 - 805 Å (2nd order)[**]
		660 - 1490 Å (1st order)
	Collimator focal length	399.60 mm
	Grating radius	3200.78 mm
	Grating spacing	2777.45 Å (3600.42 lines mm^{-1})
	Spectral resolution	45 mÅ
Detectors		
	Array size	1024 (spectral) $\times$ 360 (spatial) pixels
	Mean spectral pixel size	26.6 μm (Det. A); 26.5 μm (Det. B)
	Mean spatial pixel size	26.5 μm (Det. A); 26.5 μm (Det. B)

[*] Detector A got permanently switched off in 2006 because of a failure in readout electronics.

[**] In the range below 500 Å the sensitivity is very low, because of three normal incidence reflections. Strong lines have, however, been observed in this regime during the calibration phase and under operational conditions.

bromide (KBr) layer which increases the detector's quantum efficiency by up to a factor of 10 in the range from 900 Å to 1600 Å (Figure 2.2). Details of detector properties are well described by Teriaca (2001) and Wilhelm et al. (1995). After 11 years of successful operation, detector A was lost in 2006 because of a rapidly progressing damage in the post-anode digital electronics. Since then only detector B has been operated. The data
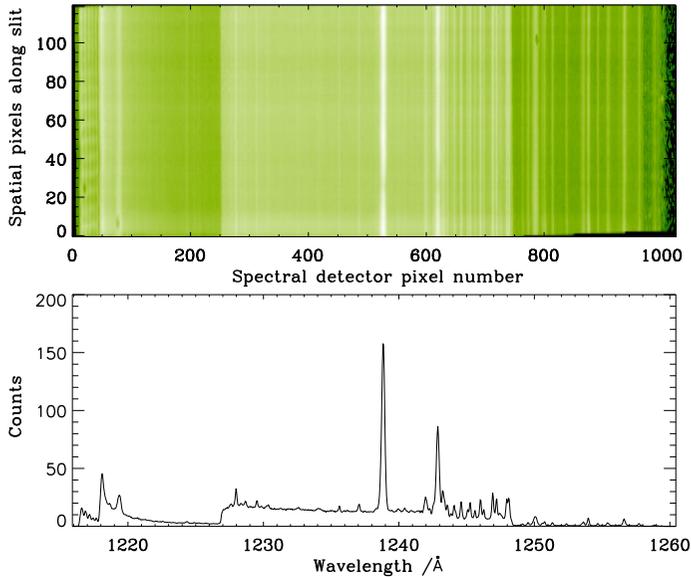
Figure 2.2: Upper panel: SUMER VUV quiet Sun spectrum obtained on 6 April 2007 at disk central (logarithmic scale). Full area of detector B in spectral pixels and central part of it in spatial pixels along the slit (1024×120 pixel^2) is imaged by 1×120 arcsec^2 slit. The difference in the sensitivity of the KBr coated part (from about detector spectral pixel 250 to 750) with the bare part of the detector is clearly seen. Lower panel: shows the spectrum obtained by averaging along the slit.

reduction of SUMER is described in Section 3.1.

2.2   EIS/Hinode

The normal incidence Extreme ultraviolet (EUV) Imaging Spectrometer (EIS) aboard Hinode (a joint Japan/UK/US mission with ESA and Norwegian involvement), is designed to observe upper transition region and solar corona in the wavelength ranges 170-210 Å and 250-290 Å. EIS observes the emission lines of highly ionized elements over a large range of plasma temperature (0.04 MK, 0.25 MK, 1.0 MK < T < 20 MK) to identify the physical processes involved in heating the solar corona. EIS has spatial resolution of about 1 arcsec, and a field of view of up to 560×512 arcsec^2.

The EIS instrument was designed and developed by an international collaboration of
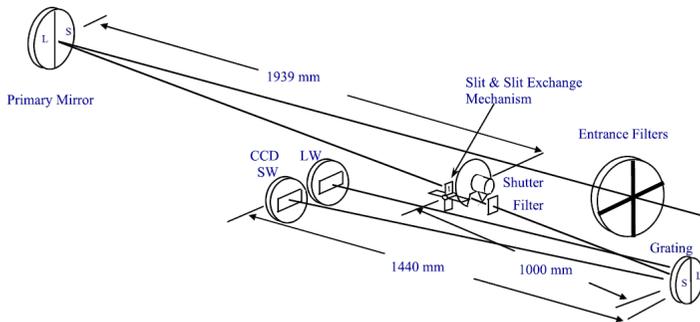
Figure 2.3: The optical design of the EIS instrument aboard Hinode is shown in this figure. Each component is labelled and dimensions are given in mm. S/SW and L/LW corresponds to short and long wavelength bands, respectively (courtesy of Culhane et al. 2007).

Mullard Space Science Laboratory (MSSL), The University of Birmingham, Rutherford Appleton Laboratory (RAL), NASA MSFC/GSFC, NRL Hulbert Center for Space Research, University of Oslo, JAXA, and NAOJ. Hinode (Solar-B) is the follow-up to the Yohkoh (Solar-A) mission and it was launched on the final flight of the M-V-7 rocket from Uchinoura Space Center, Japan on 22 September 2006 and reached a quasi-circular sun-synchronous orbit over the day/night terminator, which allows near-continuous observation of the Sun. On 28 October 2006, the probe's instruments captured their first images and has worked successfully until now.

EIS measures line intensities, Doppler velocities, line widths, temperatures and densities of the plasma in the Sun's atmosphere over the solar disk and off the limb in the inner corona. These measurements made it possible to study different size scale physical processes on the Sun. Special design and suitable multilayer coating allow EIS to operate at $\lambda < 300$ Å with high photon throughput and enhanced spectral and spatial resolution over pervious spectrometers that operated at these wavelengths (Culhane et al. 2007). The optical design and layout of the instrument is shown in Figure 2.3. The telescope is a normal incidence and off-axis paraboloid design, with focal length of 1.9 m. The superpolished mirror of the telescope has usable diameter of 150 mm. The total length of the instrument is 3 m. The spectrometer has a large effective area in two spectral EUV bands (170-210 Å and 250-290 Å) through the use of multilayer coating (Mo/Si: Molybdenum Silicon) of the primary mirror and concave grating. The instrument is mounted in a composite structure with low coefficient of thermal expansion that acts as a stable bench for the optical components. Solar radiation enters through a thin 1500 Å Aluminum filter that stops visible radiation from entering the instrument. This entrance filter is housed in an evacuated place that gives protection from acoustic stress and debris during the launch.

Table 2.2: EIS optical characteristics (Culhane et al. 2007)

Telescope		
	Focal length	1939 mm
	Peak effective areas[a]	0.30 cm^2 and 0.11 cm^2
	Primary mirror	150 mm diameter;
		two Mo/Si multilayer coatings
	Plate scale on slit plane[a]	9.37 μm arcsec^{-1}
	Raster	1 arcsec in 0.7 s[b]
		(Minimum step size: 0.123 arcsec (East-West))
	Field of view	6 arcmin $\times$ 8.5 arc min
		(offset center: $\pm$15 arcmin (East-West))
Slit and slots[a]		
	1	1 $\times$ 512 arcsec^2
	2	2 $\times$ 512 arcsec^2
	3	40 $\times$ 512 arcsec^2
	4	256 $\times$ 512 arcsec^2
Spectrometer		
	Wavelength bands	170-210 Å
		250-290 Å
	Grating	Toroid surface
		Holographic and laminar ruling
		4200 lines mm^{-1}
		Two Mo/Si multilayers
	Grating radius	1182.98 mm (dispersion direction)
		and 1178.28 mm (perpendicular direction)
	Spectral resolution	47 mÅ (FWHM) at 185 Å;
		1 pixel $\approx$ 22.3 mÅ
	Spatial resolution (pixel)	1 arcsec
Detectors[c]		
	Array size	2048 (spectral) $\times$ 1024 (spatial) pixels
	Mean pixel size	13.5 μm (spectral) $\times$ 13.5 μm (spatial)
	CCD frame read time	0.8 s

[a]   Measured values.
[b]   Raster steps occur during CCD readout.
[c]   Two back-thinned e2v CCDs.

Primary mirror focuses the photons onto a slit and then photons incident on a toroidal concave grating (see Figure 2.3). Finally, the diffracted radiation is registered by a pair of thinned back-illuminated 1024 $\times$ 2048 CCD detectors. A Slit/Slot change mechanism lets one of the possible four apertures (1, 2, 40, 266 arcsec) to be chosen. Exposure times are

controlled by a rotating shutter. The EIS optical properties are summarized in Table 2.2. Raster scanning capability is provided by a piezoelectric transducer actuator which rotates the primary mirror. The raster scan covers a field of view of 360 arcsec in the dispersion direction and 512 arcsec in the slit direction. There is a coarse pointing mechanism that allows to offset the mirror by ±15 arcmin from the spacecraft pointing axis in East-West direction. The details of the spectrometer can be found in the Culhane et al. (2007). The data reduction process for EIS spectrometer is described in Section 3.2.

2.3   EIT/SoHO

The Extreme ultraviolet Imaging Telescope (EIT) aboard Solar and Heliospheric Observatory (SoHO) provides wide-field images in four narrow passbands over the solar disk up to 1.5 $R_\odot$ in the temperature range from 6×10^4 K to 3×10^6 K. EIT was built and operated by NASA/Goddard Space Flight Center[3], USA, solar Physics Group at the Royal Observatory[4] of Belgium and Institut d'Astrophysique Spatiale[5] in Orsay, France. The EIT obtained its first images of the Sun on 2 January 1996 and till the end of July 2010 was doing synoptic observations of the low corona. Later on, AIA/SDO images with higher spatial and temporal resolution became available for three out of four EIT wavebands, and four other EUV wavelengths, as well. The scientific goal of EIT was to probe the dynamics and evolution of coronal plasma structures on global scale (over a wide range of time scale, sizes, and temperatures) to achieve new insights about responsible mechanisms of coronal heating and origin of the solar wind acceleration. Since SoHO is

[3]http://sohowww.nascom.nasa.gov/about/instruments.html
[4]http://umbra.nascom.nasa.gov/eit/
[5]http://www.ias.fr/
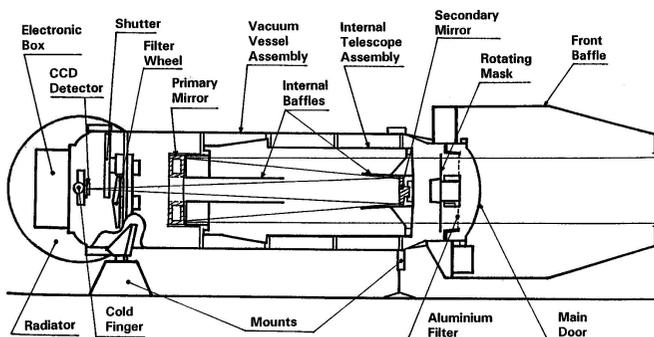
Figure 2.4: Schematic of EIT including its major subsystems (taken from Delaboudinière et al. 1995).
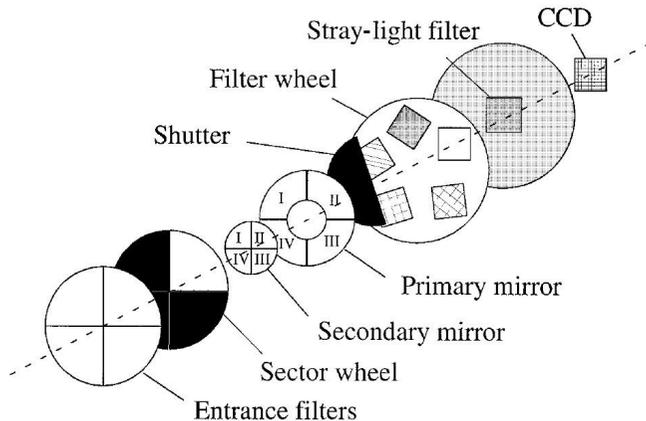
Figure 2.5: Optical layout of EIT (courtesy of Dere et al. 2000).

at the L1 Lagrangian point, EIT could provide a continuous time series of observations that provide a good opportunity for dynamical analyses.

Table 2.3: EIT Band passes (taken from Delaboudinière et al. 1995)

Wavelength	Ion	Peak Temperature	Observational Objective
304 Å	He II	$8.0 \times 10^4 K$	chromospheric network; coronal holes
171 Å	Fe IX-X	$1.3 \times 10^6 K$	corona and transition region boundary; structures inside coronal holes
195 Å	Fe XII	$1.6 \times 10^6 K$	quiet corona outside coronal holes
284 Å	Fe XV	$2.0 \times 10^6 K$	active region

A schematic of EIT is shown in Figure 2.4. The EIT is a Ritchey-Chretien design telescope with a 1024×1024 CCD detector and several filters with 45×45 arcmin^2 field of view and 2.6 arcsec pixels that approximately provides 5 arcsec resolution on the Sun (Delaboudinière et al. 1995). A heat rejection filter (composed of 700 Å of cellulose sandwiched between 1500 Å thick films of Al) covers the EIT entrance aperture. The multilayer Mo-Si coatings (Molybdenum-Silicon tuned to different λs in each quadrant) on the primary and secondary mirrors provide high reflectivity in narrow bands at EUV wavelengths. The mirror coatings have been applied in quadrants and different coatings applied in each quadrant to select four wavelength bands near 171, 195, 284, and 304

Å (Table 2.3).

Table 2.4: EIT optical properties (taken from Delaboudinière et al. 1995)

Telescope (Ritchey-Chretien)		
	Mirrors	Multilayer-coated Zerodur
	Multilayers	Mo-Si tuned to different λs in each quadrant
	Bandpass centers	171 Å, 195 Å, 284 Å, and 304 Å
	Bandpass selection	Rotatable open quadrant shutter
	Effective focal length	165.2 ± 0.2 cm
	Primary diameter	12 cm
	Geometrical area per quadrant	13 cm^2
CCD detectors (cooled to about -80 C)		
	Array size	1024×1024 pixels (45×45 arcmin)
	Mean pixel size	21 $\mu m \times 21 \mu m$ (2.6 arcsec)
	Readout rate	5×10^4 pixels sec^{-1}
	Full frame readout time	21 s
Filters		
	Entrance Filter	1500 Å Al/700 Å cellulose/1500 ÅAl
	Filter wheel: Pos. 0	1500 Å Al
	Pos. 1	1500 Å Al/700 Å cellulose/1500 ÅAl
	Pos. 2	CCD bottom third blocked, top 1500 Å Al
	Pos. 3	Open, no filter
	Pos. 4	CCD top third blocked, bottom 1500 Å Al
	CCD stray light Filter	1500 Å Al adjacent to CCD

Images of coronal lines shows coronal loops and their magnetic topology. The He II transition region images indicate the magnetic footpoints of the coronal loops and outline the bases of coronal holes which are the locations of open magnetic fields where high speed solar wind streams originate.

At a time, only one of the quadrates can be used. There is a rotating mask in front of the telescope that makes this selection. A schematic of the EIT optical layout is shown in Figure 2.5. There are several filters in the design of the instrument: entrance filters (that

consist of thin aluminum coatings on both sides of a celluloid film supported by a metal grid), five filters on a filter wheel (two are thin aluminum filters which block roughly half of the filter aperture. The remaining three filters on the filter wheel include a clear aperture, an aluminum/celluloid filter as on the entrance aperture, and a pure aluminum filter), and a final stray light filter (made of pure aluminum) immediately in front of the CCD detector (Dere et al. 2000). The effective focal length of the telescope is about 165 cm and each quadrant has geometrical area of 13 cm^2. Further details of EIT[6] are given in Table 2.4. The telescope is well described by Delaboudinière et al. (1995).

In the thesis, I have used Fe xii 195 Å line solar disk images to co-align it with EIS Fe xii 195 Å images. In Section 3.3 the data reduction of EIT is described.

2.4   AIA/SDO

The Atmospheric Imaging Assembly (AIA) aboard Solar Dynamics Observatory (SDO) is designed to provide multiple simultaneous high resolution full-disk images of the transition region and corona up to 1.5 R$_\odot$ in seven EUV and three UV-visible channels with 1.5 arcsec (4096 × 4096 pixel images) spatial resolution and 12 second temporal resolution. SDO spacecraft was launched on 11 February 2010 from Cape Canaveral Air Force Station. It has operated essentially continuously since 28 April 2010. The AIA instrument is designed and developed at LMSAL (Lockheed Martin Solar and Astrophysics Labo-

---

[6]EIT images are available on 'http://umbra.nascom.nasa.gov/eit/eit-catalog.html'
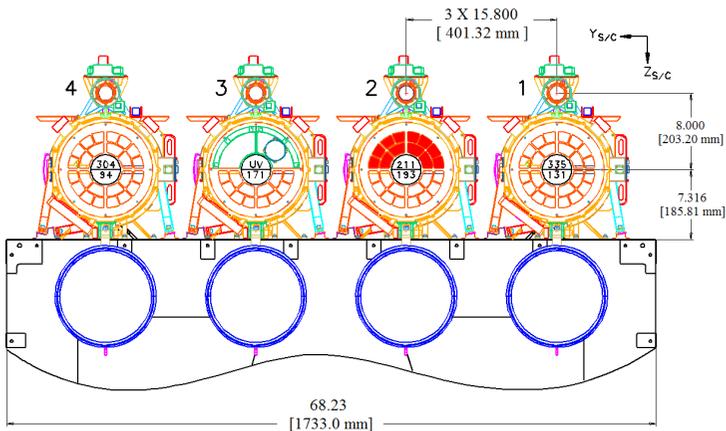

Figure 2.6: Drawing of the AIA Instrument showing four telescopes and their wavebands (courtesy of Podgorski et al. 2009).

ratory), Palo Alto, CA; (PI: Alan Title, LMSAL). The SAO (Smithsonian Astrophysical Observatory) plays a major role in the AIA program.

The primary goal of the AIA science investigation is to use these data, together with data from other SDO instruments and from other observatories, to significantly improve our understanding of the physics behind the activity displayed by the Sun's atmosphere, which drives space weather in the heliosphere and in planetary environments. To have a better understanding of the dynamics of the solar atmosphere, it is necessary to look at the whole solar disk and the adjacent corona with high spatial resolution and cadence. Because of the technology limitations in the design of the earlier solar missions, only one of these two main operational strategies was selected to design and build the instruments (For instance, EIT/SoHO was designed to observe the entire solar disk to enable studies of global coronal dynamics but it sacrifices spatial and temporal resolution required to make detailed studies. In other hand, TRACE project (Handy et al. 1999) designed to capture the dynamics of the corona in high temporal and spatial resolution but it was forced to have limited field of view.). However, both of these parameters are reflected in the instrumental design of AIA and enabled it to take high resolution pictures of different layers in the Sun's atmosphere to further understand how changing solar magnetic fields release the energy that heats the solar corona and creates flares.

Table 2.5: The primary ions observed by AIA. Many are species of iron covering more than a decade in coronal temperatures (from Podgorski et al. 2009, Lemen et al. 2012).

Telescope	Position	Center wavelength	Primary ion(s)	Region of atmosphere	log(T)
1	Top	335 Å	Fe xvi	active-region corona	6.4
1	Bottom	131 Å	Fe viii, xxi	transition region, flaring corona	5.6, 7.0
2	Top	211 Å	Fe xiv	active-region corona	6.3
2	Bottom	193 Å	Fe xii, xxiv	corona and hot flare plasma	6.2, 7.3
3	Top	4500 Å	continuum	photosphere	3.7
3	Top	1700 Å	continuum	temperature minimum, photosphere	3.7
3	Top	1600 Å	C iv+cont.	transition region, upper photosphere	5.0
3	Bottom	171 Å	Fe ix	quiet corona, upper transition region	5.8
4	Top	304 Å	He ii	chromosphere, transition region	4.7
4	Bottom	94 Å	Fe xviii	flaring corona	6.8

This instrument consists of four normal incidence Cassegrain telescopes with multilayer coated optics that optimize the selected EUV wavelengths of interest in order to
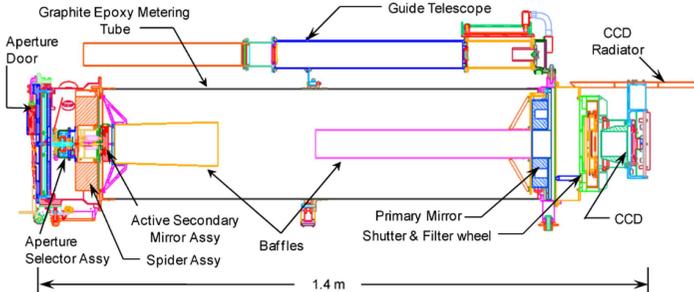
Figure 2.7: Schematic layout of an AIA telescope assembly. The aperture door protects the entrance filters during launch operations. Each of the four AIA telescopes has its own guide telescope, which provides a signal for the active secondary to stabilize the image on the CCD (taken from Lemen et al. 2012).

observe solar emissions from the transition region and corona. Each of these telescopes is divided to two sections and each section images in a different waveband (Fig. 2.6).

Different multilayer coatings were applied to each half of each telescope optic to achieve the desired central wavelength. These EUV wavebands centered on specific lines: Fe xviii (94 Å), Fe viii, xxi (131 Å), Fe ix (171 Å), Fe xii, xxiv (193 Å), Fe xiv (211 Å), He ii (304 Å), and Fe xvi (335 Å). Top section of telescope number 3 observes C iv (near 1600 Å) and the nearby continuum (1700 Å) and has a filter that observes in the visible to enable coalignment with images from other telescopes. Table 2.5 listed the different sections of the four telescopes with the corresponding lines and multilayer coatings.

The design of these four telescopes are identical in most regards. Internal view of an AIA Telescope is shown in Figure 2.7. The light enters the telescope through the aperture of the telescope, passes the filter aperture assembly and goes toward the primary mirror. Then it reflects toward the secondary mirror, which reflects the light toward the focal plane. There is a shutter and filter wheel near the focal plane. The shutter controls the exposure time. The filter wheel places the desired filter in the light path, thus controlling the spectral content of the incoming light. Since the mirror coatings act as narrow bandpass filters, the focal plane filters effectively select which channel of the telescope is sending light to the detector (Cheimets et al. 2009). At the focal plane are back-thinned CCD sensors with 4096×4096 pixels, each 12-μm pixel corresponds to 0.6 arcsec. Entrance filters at the telescope aperture block visible and IR radiation. Key parameters of AIA are given in Table 2.6. Further details about AIA can be found in Lemen et al. (2012). Section 3.4 summarizes the data reduction steps of AIA.

Table 2.6: The AIA instrument characteristic (Lemen et al. 2012)

Telescope (Ritchey-Chretien)		
	Mirrors	Multilayer-coated Zerodur
	Multilayers	94 (Mo/Y),
		131 (Mo/Si),
		304 and 335 (SiC/Si) Å
		171, 193 and 211 (Mo/Si) Å
		three UV-visible channels (Al/MgF$_2$)
	Effective focal length	4.125 m
	Primary diameter	20 cm
		(with a 4.5 cm diameter center hole)
	Geometrical area of UV channel	30.8 cm^2
CCD detectors[*]		
	Array size	4096 × 4096 pixels (41 arcsec^2)
	Mean pixel size	12 μm × 12 μm (0.6 arcsec^2)
	Readout rate	2 × 10^6 pixels sec^{-1}
	Full frame readout time	8 wavelengths in 10 to 12 seconds
	All telescopes	
Filters		
	Entrance Filter	1500 Å Al/700 Å cellulose/1500 ÅAl
	Filter wheel: Pos. 0	1500 Å Al
	Pos. 1	1500 Å Al/700 Å cellulose/1500 ÅAl
	Pos. 2	CCD bottom third blocked, top 1500 Å Al
	Pos. 3	Open, no filter
	Pos. 4	CCD top third blocked, bottom 1500 Å Al
	CCD stray light Filter	1500 Å Al adjacent to CCD

[*] Back thinned & back illuminated

3 Observations and data reduction

This chapter summarizes the data reduction process for the different instruments (SUMER, EIS, EIT, and AIA) that we have used for this thesis work.

3.1 SUMER/SoHO

The Solar Ultraviolet Measurements of Emitted Radiation, SUMER, is a spectrograph that observes over the wavelength range 450 Å to 1610 Å. Part of the payload of the Solar and Heliospheric Satellite (SoHO), launched in 1995, SUMER, has a spatial resolution of 1 arcsec across and 2 arcsec along the slit and a spectral scale of $\approx$ 43 mÅ/pix at 1240 Å (first order) (Wilhelm et al. 1995, Lemaire et al. 1997), that is high enough to measure small line shifts down to 1 km s^{-1} (see Section 2.1). Reduction of SUMER spectra consists of the following steps:

- Dead time and local gain correction

- Flat-field correction (in order to correct for the non-uniform sensitivity of the detector on scales of less than 20 pixels.)

- Geometrical distortion (caused by the detectors' read-out electronics and resulting in a distortion of the spectral images that is stronger at the detector edges. This correction is not too accurate near the edges of the detectors.)

- Radiometric calibration (in order to pass from counts px^{-1} s^{-1} to erg cm^{-2} s^{-1} sr^{-1} Å^{-1} and to correct for the differences in sensitivity between KBr-coated and bare microchannel plate.)

The details of these corrections can be found in the thesis of Teriaca (2001). After correcting the data for the mentioned effects, we can go ahead and perform the wavelength calibration.

Accurate measurements of Doppler velocities need an accurate wavelength calibration to be performed on the data. In the following, we first describe the wavelength calibration steps and then show in detail three examples of Doppler shift measurements of EUV transition region and low coronal emission lines in a quiet Sun area at disk center: N v 1238 Å and N v 1242 Å lines with formation temperature of (log(T/[K]) = 5.24) are transition region lines and Mg x 625 Å is a warm coronal line with formation temperature of (log(T/[K]) = 6.00).

3.1.1 Wavelength calibration

To measure the Doppler shift of each line, special attention should be paid to the wavelength calibration. Wavelength calibration produces a wavelength scale that correlates detector pixel positions to wavelength values. There are different ways to perform the wavelength calibration:

- One of the ways is to mount a calibration source on the instrument directly. However, this is usually not a viable solution for space-borne spectrometers such as SUMER and EIS. The reasons, in short, are difficulty in finding useful materials to build the lamp window, weakness of the EUV spectrum produces by the gases inside the lamp, and the large needed power to produce the EUV spectrum (look to Appendix A, Young et al. 2012).

- Another way, that is useable for SUMER spectra, is to calibrate the spectrum with respect to a set of chromospheric lines which are already present in the wavelength range of study and are close to the line of which we want to measure the Doppler shift. Some examples of suitable chromospheric lines are those from Si I, S I and C I atoms. The first two are forming at temperatures around 6500 K, and the last forms at a temperature around 10000 K. All these cool chromospheric lines typically show only rather small average Doppler shifts that allow us to consider them as at rest. This is confirmed by observations of Hassler et al. (1991). They used data from an EUV coronal spectrometer mounted on a rocket flight mission[1] containing an on-board calibration lamp and found the Doppler shifts of cool chromospheric lines are very small (close to zero) and therefore negligible. Moreover, results from a balloon-based experiment analysed by Samain (1991) showed a small average net red shift of 1 km s^{-1} for cool chromospheric lines. Since the transition region and coronal lines have much larger velocities (Doschek et al. 1976, Brekke 1993, Brekke et al. 1997, Chae et al. 1998, Teriaca et al. 1999a, Peter and Judge 1999, Dadashi et al. 2011), with a very good approximation we can consider the chromospheric lines to be at rest. An example of using this method to obtain the Doppler shifts is provided by Brekke et al. (1997). In this thesis work we have used this method for wavelength calibration. The detail of this technique is described in the following.

- The last method is to compare to spectra of quiet areas above the limb, where it can be assumed that the horizontal bulk flows on average cancel out. Then all measurements are done relative to the off-limb data. An example of this method is provided by Doschek et al. (1976) using the SKYLAB solar spectra and Peter and Judge (1999) using the SUMER spectra.

In the second method (using chromospheric lines for calibration), in choosing the chromospheric lines three important points should be considered:

1. The chromospheric lines should be narrow and come from neutral and singly ionized atoms, formed around the temperature minimum or lower chromosphere.

---

[1]called LASP and launched on 27 July 1987

2. The selected lines should be fairly strong and unblended.

3. The wavelengths at rest of these lines must be known with adequate accuracy (better than 1 km s^{-1} or 0.0041 Å at 1240 Å).

We should remember that all the absolute velocity measurements made with SUMER will be relative to these chromospheric lines. In theory, only two chromospheric lines are sufficient to establish a wavelength scale. In reality a larger number of lines (ideally at least four or five) is necessary to provide robustness against errors in the rest wavelengths and/or unknown blends that may affect some of the lines. To perform wavelength calibration we have to follow three main steps:

1. Identify the spectral lines by using a preliminary wavelength scale derived from the information inside the data header and compare with laboratory wavelength values and solar reference spectra such as those of, e.g., Curdt et al. (2001).

2. Find the exact pixel position of each line, by fitting a single Gaussian curve plus a constant background to the line profiles.

3. Find a dispersion relation by a polynomial fit (possibly linear) of the centroids (in pixels) to the laboratory wavelength values.

Using the dispersion relation, an accurate wavelength scale could be established. The first step in wavelength calibration is very important. The identification of these chromospheric reference lines is sometimes difficult because the spectrum is crowded of such lines, several of which are still unidentified. Moreover, not all transitions listed in atomic databases are producing a visible emission line under the conditions present in the solar atmosphere.

In the following, we describe three examples of measuring the Doppler shift of transition region and coronal lines over the quiet Sun at disk center. The SUMER dataset that we used was obtained on 6 April 2007 between 03:26 to 04:31 UTC. It consists of 40 slit position with step size of 1.87 arcsec and exposure time of 100 s. The 1" × 120" arcsec^2 slit is used to obtain the spectra in the range of 1210 Å to 1270 Å. The dataset is an array of 1024 × 40 × 120 elements showing spectral, temporal/spatial (direction perpendicular to slit direction, or solar X) and spatial (along the slit direction or solar Y) pixels, respectively. To increase the number of the counts to have better statistics, first we sum the total of the counts along the spatial Y (along the slit from pixel 20 to 100) and also along the whole spatial X (time). We use this average (more precisely total) spectrum for line identification, wavelength calibration and to measure the observed wavelength of N v and Mg x. Figure 3.1 shows the average spectrum with the first order wavelength scale (1210-1270 Å). To avoid the residual errors of the geometric distortion correction near the edges of the detector, we have considered only the central part of the spectrum (1225-1260 Å).

3.1.1.1 Line identification

By comparing the position of the lines (obtained by Gaussian fitting) with the laboratory wavelengths listed by Kelly (1987), and by comparing the spectra with reference lists of
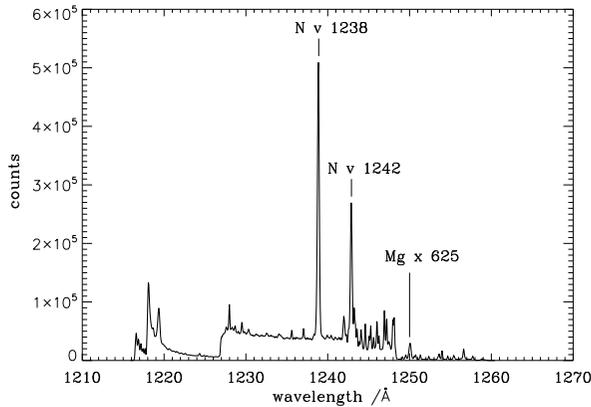
Figure 3.1: SUMER averaged spectrum with the first-order wavelength scale (1216-1260 Å). To avoid the residual errors of the geometric distortion correction near the edges of the detector, we have studied the central part of the spectrum (1225-1260 Å).

identified solar lines (e.g. Brekke et al. 1997), we have identified the chromospheric lines. In the first step, 49 lines are identified which are listed in the sixth column of Table 3.1. This first-look identification for some of the lines could be wrong since it is based on the accuracy of the preliminary wavelength scale and also because some of these lines are (or seems to be) blended. Therefore, to achieve the best line identification, some refinement process is needed. By looking at the residuals of the fit result, we will have an estimation about the correctness of selecting those identified lines. This is explained in more detail in the example Sections 3.1.3 and 3.1.4.

3.1.1.2   Finding the line centers

Figure 3.2 shows the average spectrum with respect to the pixel positions (from 0 to 1023). We have performed a Gaussian fit with a constant background to each line of the spectrum. The exact pixel position of the center of the Gaussian curves and the corresponding errors are listed in the second and third columns of Table 3.1.

3.1.1.3   Establishing an accurate wavelength scale

For every identified line present in Table 3.1, we have a set of x and δx (as the center of the Gaussian fit and its error) and a laboratory wavelength λ from the Kelly (1987) reference database. By performing a first (for the spectral region around the N v lines) or second (for the spectral region around the Mg x line) order polynomial fit, we have found the best dispersion relation that leads us to establish the most accurate possible calibrated wavelength scale.
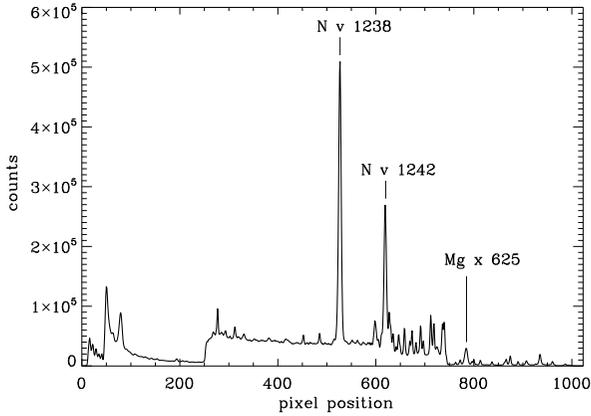
Figure 3.2: SUMER averaged spectrum in pixel position.

○ **Linear fit (used for N v lines)**:

Equations 3.1 and 3.2 are showing a linear relation between the position of a observed line in pixel (x) and the laboratory wavelength (λ). To avoid large errors on q, we have subtracted the minimum value of the λ (called λ_{min}) from the whole laboratory wavelengths of Kelly (1987) before performing the linear fit. This value will be added after the linear fit processes is performed.

$$x = m\lambda + q \tag{3.1}$$

$$\lambda = \frac{1}{m}x - \frac{q}{m} \tag{3.2}$$

The error on the λ value at a position x (determined with an uncertainty δx) is obtained by error propagation as[2]:

$$\delta\lambda = \delta(\frac{1}{m})x + \frac{1}{m}\delta x + \delta(\frac{1}{m})q + \frac{1}{m}\delta q \tag{3.3}$$

$$\delta\lambda = (\frac{\delta m}{m^2})x + \frac{1}{m}\delta x + (\frac{\delta m}{m^2})q + \frac{1}{m}\delta q \tag{3.4}$$

A weighted (by considering the uncertainties on the line centroids) first order polynomial fitting procedure gives m, δm, q, and δq as results of the regression. Entering these four values in equations 3.2 and 3.4, for every measured point of x with uncertainty δx, gives us the Sun measured wavelength with its corresponding error ($\lambda \pm \delta\lambda$).

---

[2]The variables are considered to be dependent, being coupled by the regression. This is a conservative estimate that is used here. If the variables considered to be independent, the error became smaller. For instance, the error for N v 1238 Å (shown in Table 3.4) shrinks to 0.36 km s^{-1}.
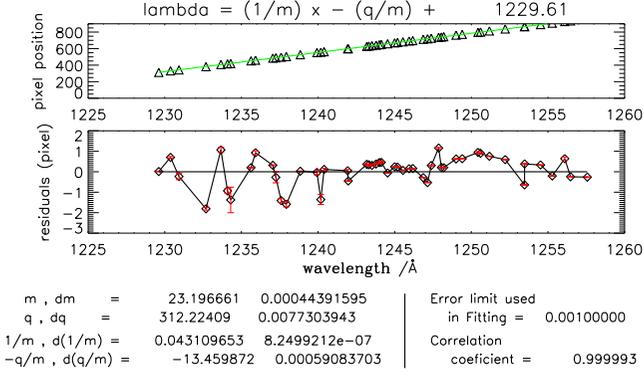
Figure 3.3: First order dispersion relation with all 49 lines, (λ = 0.043109653 x + 1216.1482). All the fitting coefficients and their corresponding errors are summarized at the bottom of the plot.

○ **Second order polynomial fit (used for Mg x line):**

For the part of the spectrum that contains the Mg x line, we have performed a second order polynomial fit. Equation 3.5 shows a second order polynomial relation between λ and x. Solving this equation gave two values[3] for λ which is represented by Eq. 3.6. Similar to the linear fit case, to avoid large errors on q, we have subtracted the λ_{min} value from the whole laboratory wavelengths of Kelly (1987) before applying the second order polynomial fit. This value will be added afterward.

$$x = n\lambda^2 + m\lambda + q \tag{3.5}$$

$$\lambda = \frac{-m \pm \sqrt{m^2 - 4n(q - x)}}{2n} \tag{3.6}$$

The error on the λ value at a position x (determined with an uncertainty δx) is obtained by error propagation as:

$$\delta x = \delta(n\lambda^2) + \delta(m\lambda) + \delta q \tag{3.7}$$

$$\delta x = (\delta n)\lambda^2 + 2\lambda(\delta\lambda)n + (\delta m)\lambda + m(\delta\lambda) + \delta q \tag{3.8}$$

$$\delta\lambda = \frac{(\lambda^2\delta n + \lambda\delta m + \delta q) + \delta x}{2\lambda n + m} \tag{3.9}$$

By considering the uncertainties on the center of the lines, a weighted second order polynomial fit was performed that gives n, δn, m, δm, q, and δq as its result. Using these six values in equations 3.6 and 3.12, for every measured point of x with uncertainty δx, gives us the Sun measured wavelength with its corresponding error ($\lambda \pm \delta\lambda$).

---

[3]Only one of them is positive and therefore has physical meaning.
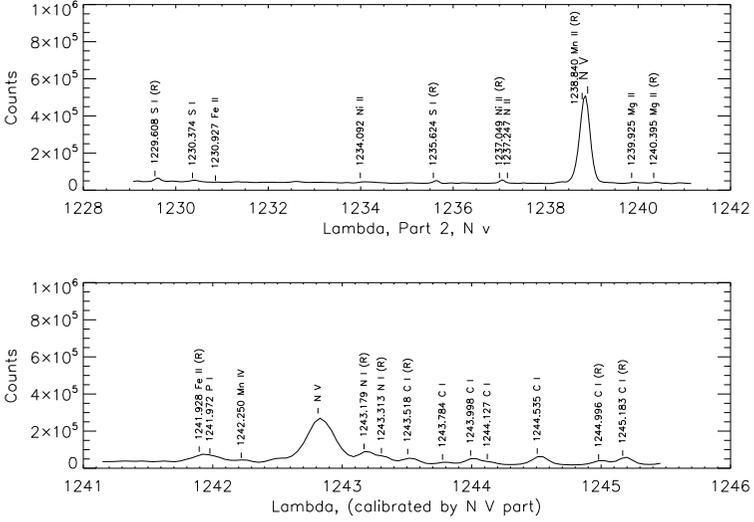
Figure 3.4: Preliminary identified lines for part 1 of the spectrum, containing N v. The finally chosen chromospheric lines to establish the wavelength scale are marked with R.
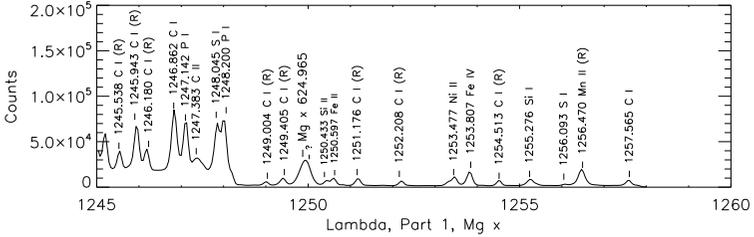
Figure 3.5: Preliminary identified lines for part 2 of the spectrum, containing Mg x. The finally chosen chromospheric lines to establish the wavelength scale are marked with R.

3.1.2 Calculating the Doppler Shift

After establishing the precise wavelength scale, we fit a Gaussian curve to the lines of which we want to measure the shifts using the calibrated wavelength vector and measure the accurate center of the lines (λ_{Sun}) and their corresponding errors ($\delta\lambda_{Sun}$). The Doppler shifts, v_D, are obtained using Eq. (3.10):

$$v_D = 3 \times 10^5 (\frac{\lambda_{Sun} - \lambda_{rest}}{\lambda_{rest}}) \qquad [\text{km s}^{-1}] \tag{3.10}$$

47

and errors by Eq. (3.11):

$$\delta v_D = 3 \times 10^5 (\frac{\delta \lambda_{\text{Sun}}}{\lambda_{\text{rest}}}) \qquad [\text{km s}^{-1}] \qquad (3.11)$$

where λ_{rest} is the rest wavelength of the lines of which we want to measure the shifts. Rest wavelength values are obtained either by laboratory measurements or based on Solar measurements techniques. The accuracy of rest wavelength measurements have a very important influence on the obtained Doppler shifts. Therefore, special care should be considered in selecting the rest wavelengths. We have used the values of Edlén (1942), Kelly (1987), Dammasch et al. (1999a), and Peter and Judge (1999) for the rest wavelengths and compare the results in Sections 3.1.3.5 and 3.1.4.6.

3.1.3   Example 1 and 2 (N v 1238 Å and 1242 Å)

The wavelength interval around the **N v 1238 Å** and **N v 1242 Å** lines are shown in the top and lower panel of Figure 3.4. These two lines are the strongest lines in this spectral range and are recorded on the KBr coated area of the detector. As it is mentioned in Section 2.1, the KBr coating greatly enhances the sensitivity of the detector to lines observed in the first order with respect to those observed in the second order. This allows studying the properties of first order spectral lines with good statistics (high signal to noise ratios) and, at the same time, minimizes potential blending with second order lines.

The next four Subsections are describing the process of choosing the suitable chromospheric reference lines to perform an accurate wavelength calibration for the N v lines and the fifth Subsection describes the results of Doppler shift measurements for these lines.

3.1.3.1   First step: linear fitting of 49 reference lines

Using the technique described in Subsection 3.1.1.1, we have first identified 49 chromospheric lines (summarized in Table 3.1) in the studied wavelength range without considering strict restrictions on weakness or blendings of the lines. Applying a linear fit to the line central positions versus the laboratory wavelengths of the identified lines listed by Kelly (1987), a dispersion relation is obtained:

$$\lambda = 0.043109653 \, x + 1216.1482$$

where λ is the calibrated wavelength in Å, and x is the pixel position of the lines. The obtained values of λ (called λ_{Sun}) are listed in the fifth column of Table 3.1. Figure 3.3 shows the result of this linear fit with the remaining residuals and all the fit coefficients.

As it is shown in Figure 3.3, the residuals are large (between $\pm$ 2 pixels that corresponds to errors of about 20 km s^{-1}). To make a more reliable wavelength scale, we have divided the spectrum into two parts and study each part separately:

- **Part 1** that contains the N v line (1225 to 1246 Å) along with 27 chromospheric lines (lines numbered 23 to 49 in Table 3.1, Figure 3.4).

- **Part 2** which contains the Mg x line (1246 to 1260 Å) along with 22 chromospheric lines (lines numbered 1 to 22 in Table 3.1, Figure 3.5).
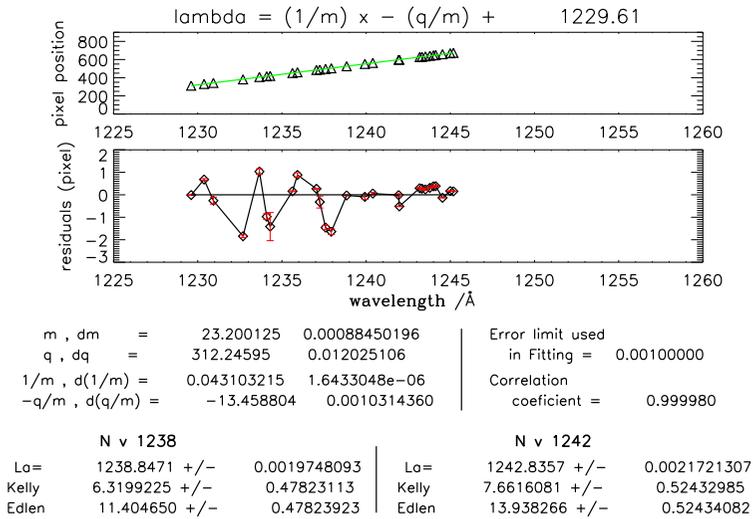
Figure 3.6: A linear fit (top panel) of 27 reference lines in the part of the spectrum (part 1) containing the N v lines with residuals up to 2 pixels (bottom panel) and the dispersion relation of ($\lambda = 0.043103215\,x + 1216.1492$). All the coefficients and their corresponding errors are summarized at the bottom of the figure. The Doppler shifts obtained by using the rest wavelengths of Kelly (1987) and Edlén (1942) for the N v lines with the above dispersion relation are also listed at the bottom of this figure.

In the following, we first focus on the first part of the spectrum to obtain the Doppler shift of the N v 1238 Å and 1242 Å lines and then we move to the second part to calculate the Doppler shift of Mg x 625 Å.

3.1.3.2 Part 1 [1225-1246 Å]: linear fitting of 27 reference lines

Figure 3.6 shows the result for the linear fitting of the 27 identified chromospheric lines in the part 1 of the spectrum. The new dispersion relation is:

$$\lambda = 0.043103215\,x + 1216.1492$$

These 27 lines are listed in Table 3.1 (lines numbered 23 to 49). By looking to the residuals in Figure 3.6, nine lines (marked with ⋆ signs in Table 3.1) look to be very far from the linear fitting. Besides some always possible mis-identification, the most likely reason for the deviation from the expected position is some level of blending with unidentified/unknown spectral lines. We check these deviating lines for any possible sign of blending. A part obvious cases, where a double component can be easily seen, we should make sure that:

1. Wings of the fitted profiles should be well symmetric.
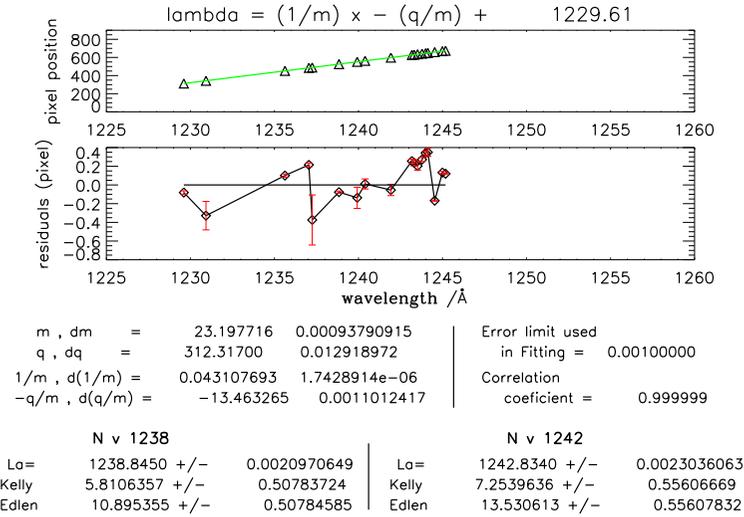
Figure 3.7: A linear fit (top panel) of 18 reference lines in the part of the spectrum (part 1) containing the N v lines with residuals up to 0.5 pixel (bottom panel) and the dispersion relation of ($\lambda = 0.043107693\ x + 1216.1448$). All the coefficients and their their corresponding errors are summarized at the bottom of the figure. The Doppler shifts obtained by using the rest wavelengths of Kelly (1987) and Edlén (1942) for the N v lines with the above dispersion relation are also listed at the bottom of this figure.

2. Typical Doppler width (thermal plus non-thermal) of the lines should be consistent with the typical observed width of these lines. The thermal Doppler width of an optically thin spectral line is given by

$$\Delta\lambda_{\text{Doppler}} = \frac{\lambda}{c} \sqrt{\frac{2KT}{m}} \tag{3.12}$$

where c is the speed of light in vacuum, K is the Boltzman constant, T is the temperature of line formation and m is the mass of the atom. The non-thermal broadening of these cold lines is usually around 10 km s^{-1}.

3. Moreover, the line should be strong enough with respect to the other lines and respect to the background emission.

The results of checking those nine deviated lines that are marked by ⋆ in Table 3.1 are summarized below:

- **P I (λ1241.972)**: very weak with respect to the other lines. Therefore, we have took this line out of our list.

- **Fe** II (λ**1237.930**), **Mn** II (λ**1237.590**), **Si** II (λ**1235.920**), **N** I (λ**1234.300**), **Fe** II (λ**1233.661**), and **P** I (λ**1232.687**) lines are also too faint and not easily observable in Figure 3.4. Then we have deleted them from the list.

- **Ni** II (λ**1234.092**) is very faint and blended with another line.

- **S** I (λ**1230.374**) line looks too wide (respect to the other normal chromospheric lines). It very likely because of blending with an unknown line, so we have excluded this line.

3.1.3.3   Part 1 [1225-1246 Å]: linear fitting of 18 reference lines

The remaining eighteen lines are listed in Table 3.2. Performing a linear fit, the dispersion relation becomes (Figure 3.7):

$$\lambda = 0.043107693\ x + 1216.1448$$

Corresponding λ values are presented in the fifth column of the Table 3.2 (called λ_{Sun}). The residuals are between $\pm$ 0.6 pixels (6 km s^{-1}). Residual curves are still large for eight more lines (marked by $\star$ in the seventh column of Table 3.2). These lines are studied from the mentioned point of views and we have decided to ignore them from the list of suitable chromospheric lines used for wavelength calibration. The reasons are listed below:

- **C** I (λ**1244.535**) line does not have a good fitted Gaussian shape (the apex of the curve is more flat).

- **C** I (λ**1244.127**) and **C** I (λ**1243.998**) are blended with each other.

- **C** I (λ**1243.784**), **N** II (λ**1237.247**), and **Fe** II (λ**1230.927**) are faint compare to the rest of the spectral lines.

- **Mg** II (λ**1239.925**) and **Mn** II (λ**1238.840**) lines are blended with each other and are faint.

3.1.3.4   Part 1 [1225-1246 Å]: linear fitting of 10 reference lines

Using the remaining ten chromospheric lines (listed in Table 3.3), the dispersion relation for the part of the spectrum that contains N v lines becomes (Figure 3.8):

$$\lambda = 0.043091817\ x + 1216.1491$$

The values of λ are shown in the fifth column of Table 3.3 (called λ_{Sun}). Figure 3.8 shows the residuals that are less than $\pm$ 0.2 pixels ($\sim$ 2 km s^{-1}). This is the maximum accuracy that we can apply to this part of the spectrum. Therefore, this set of chromospheric lines is the best set for calibration of this part of the spectrum (containing the N v lines). Using this dispersion relation, the accurate wavelength scale could be derived and made it possible to measure the accurate absolute Doppler shifts of N v lines.
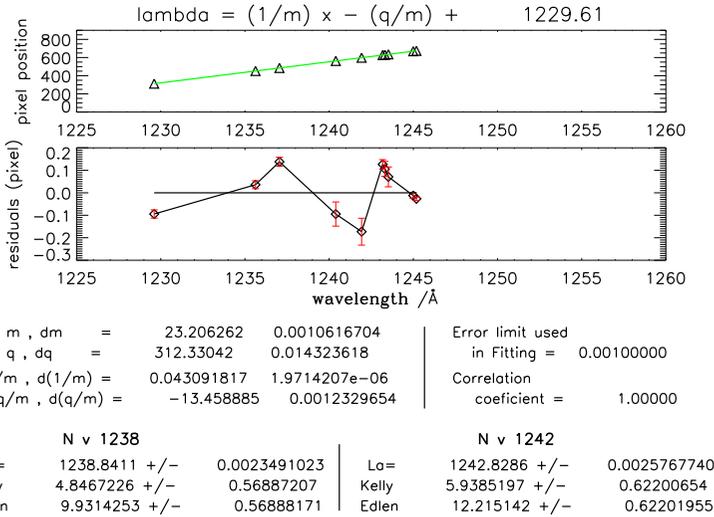
Figure 3.8: A linear fit (top panel) of 10 reference lines in the part of the spectrum (part 1) containing the N v lines with residuals up to 0.2 pixel (bottom panel) and the dispersion relation of ($\lambda = 0.043091817\ x + 1216.1491$). All the coefficients and their their corresponding errors are summarized at the bottom of the figure. The Doppler shifts obtained by using the rest wavelengths of Kelly (1987) and Edlén (1942) for the N v lines with the above dispersion relation are also listed at the bottom of this figure.

3.1.3.5   Measured Doppler shift of N v lines

Using the wavelength scale obtained in the last Section, we have performed a Gaussian curve fit to both N v lines to obtain their positions (λ_{Sun}) as explained in Section 3.1.2. For λ_{rest} values, we have used the corresponding laboratory wavelength listed by Kelly (1987) and Edlén (1942). Using Eqs. 3.5 and 3.6, the Doppler shifts and the corresponding errors are obtained and summarized in Table 3.4.

The observed position of N v 1238 Å line is λ_{Sun} = 1238.841 Å. The corresponding average line-of-sight Doppler shift of this line by using Edlén (1942) reference value (1238.800 Å), becomes +10 km s^{-1} red shifted (downward motions), and by using Kelly (1987) reference value (1238.821 Å), becomes +5 km s^{-1} red shifted. Peter and Judge (1999) reported a red shifted Doppler shift of +8 km s^{-1} for this line.

The observed position of N v 1242 Å line is 1242.828 Å. The corresponding average Doppler velocity of this line by using Edlén (1942) reference value (1242.778 Å), becomes +12 km s^{-1}, and by using Kelly (1987) reference value (1242.804 Å), becomes +6 km s^{-1}. Chae et al. (1998) reported a Doppler shift of +11 km s^{-1} for this line (using Kelly (1987) reference value). However, Brekke et al. (1997) for this line, using Edlén (1942) reference value, reported +11 km s^{-1} Doppler shift. Peter and Judge (1999) using the same rest wavelength, reported a Doppler velocity of +10 km s^{-1} for this line. Also

Teriaca et al. (1999a) using the Edlén (1942) reference value obtained a red shift of 10 km s^{-1}.

Although the rest wavelength listed by Kelly (1987) is more recent than Edlén (1942), it gives quite smaller Doppler shifts with respect to those obtained from other lines formed at similar temperatures[4], as also suggested by Brekke and Hassler (1995). Adopting this rest wavelength for the two N v lines, we obtained the Doppler velocities of +10 to +12 km s^{-1} that are very well in agreement with the Doppler shift of the other lines formed at similar temperatures (Brekke et al. 1997, Peter and Judge 1999, Teriaca et al. 1999a).

3.1.4 Example 3 (Mg x 625 Å)

This Section is focussed on the part 2 of the spectrum which contains the Mg x line (1246 to 1260 Å). This wavelength interval is shown in Fig. 3.5. The Mg x line is observed in second order on the bare part of the detector. This line looks very strong compared to the other first order lines. Preliminary line identification has result in finding 22 chromospheric lines that are listed in Table 3.1, lines 1 to 22, and shown in Fig. 3.5). The steps of refinement for choosing the best reference lines to establish the calibrated wavelength scale are shown below.

3.1.4.1 Part 2 [1246-1260 Å]: linear fitting of 22 reference lines

Using these 22 lines for calibration, the dispersion relation becomes:

$$\lambda = 0.043081109\,x + 1216.1708$$

As it is shown in the lower panel of Fig. 3.9, the residuals are less than ± 1 pixels (10 km s^{-1}). The lines that are marked by ⋆ in Table 3.1) are deviating from the linear fit. For instance,

- C I (λ1253.430 Å) line is heavily blended with a faint **Ni II** (λ1253.484 Å) line. It also has larger Doppler width with respect to what is expected from Eq. 3.12 (Figure 3.10).

- C I (λ1247.911 Å) is strongly blended with **S I** (λ1248.048 Å).

These two lines are not suitable to be used as chromospheric reference lines for wavelength calibration and will not be further considered.

3.1.4.2 Part 2 [1246-1260 Å]: linear fitting of 20 reference lines

We have applied a linear fit to the remaining 20 lines of part 2 of the spectrum. The dispersion relation becomes (Figure 3.11):

$$\lambda = 0.043076287\,x + 1216.1745$$

The list of lines and the calculated values of λ are recorded in Table 3.5 (called λ_{Sun}). The residuals are in the range of ± 0.8 pixel (∼ 8 km s^{-1}). There are four lines that look to be far from the fitted curve:

---

[4]The formation temperature of the two N v lines is $10^{5.24}$ K.

m , dm	=	23.212030	0.00072810865	Error limit used	
q , dq	=	681.67106	0.0031172377	in Fitting =	0.00100000
1/m , d(1/m) =		0.043081109	1.3513565e−06	Correlation	
−q/m , d(q/m) =		−29.367145	0.0010554747	coeficient =	0.999984

Mg x 625

Lo=	1249.9490 +/−	0.0026371612
Dammash	3.1094550 +/−	0.63295107
Peter−Judge	4.5450971 +/−	0.63295410
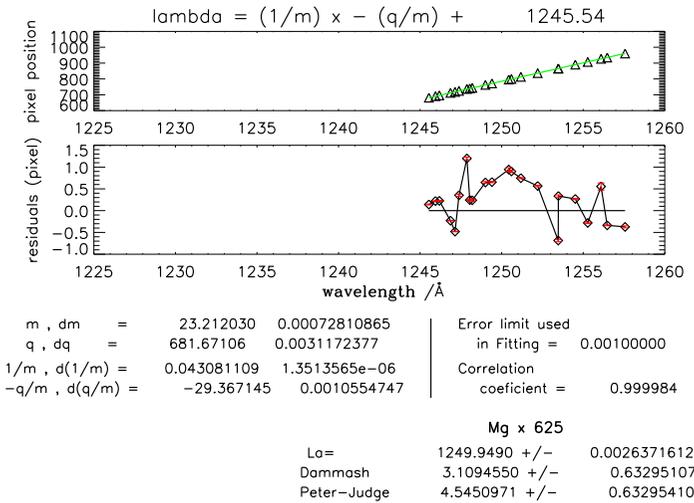
Figure 3.9: Part 2, Mg x, 22 reference chromospheric lines, ($\lambda = 0.043081109\ x + 1216.1708$)

- The **S** I ($\lambda1256.110$ Å) line is very weak and a bit blended with a strong **Mn** II line.

- **The Si** I ($\lambda1255.257$ Å) has some asymmetry on its right wing.

- **P** I ($\lambda1247.114$ Å) and **C** I ($\lambda1246.845$) lines are blended together and with an asymmetric **C** II ($\lambda1247.391$ Å) line. Therefore, these two lines are also not reliable (Fig. 3.5).

These four lines are marked with ⋆ in Table 3.5) and will be ignored.

3.1.4.3   Part 2 [1246-1260 Å]: linear fitting of 16 reference lines

Using the remaining 16 lines listed in Table 3.6 we have performed a linear fit that results in a dispersion relation of (Figure 3.12):

$$\lambda = 0.043126656\ x + 1216.1256$$

The values of λ are listed in the fifth column of Table 3.6 (called λ_{Sun}). The residuals look smaller (about ± 0.7 pixels or 7 km s^{-1}), but still not very satisfactory. A careful inspection of the line profiles reveals that lines numbered 1, 4, 7, 8, 11, 12, and 13 in Table 3.6 may not be suitable for wavelength calibration:

- **C** I ($\lambda1257.542$ Å) is blended with **P** I.

- **Ni** II ($\lambda1253.484$ Å), is the green curve in Figure 3.10. Its profile clearly shows a blend with **C** I ($\lambda1253.430$ Å) line. The blending is too close to be resolved. A

54
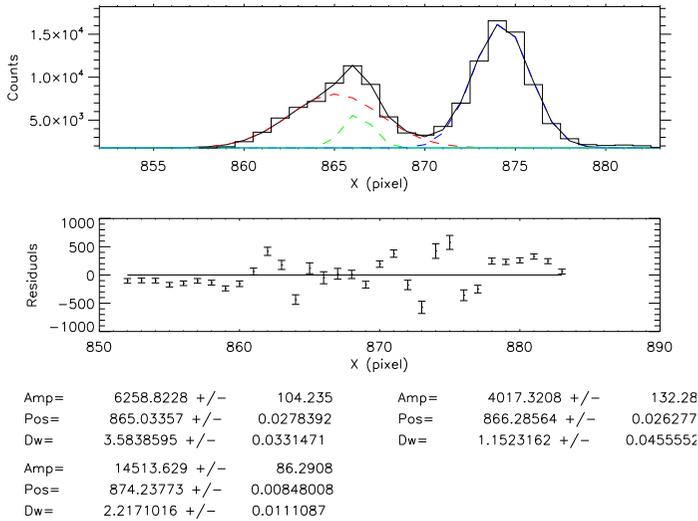
Figure 3.10: Gaussian fitting of C I (λ1253.430 Å) line: In the top panel, the red curve represents the C I (λ1253.430 Å) line which looks very broadened. Green curve is Ni II (λ1253.484 Å) and looks weak. The blue curve is Fe IV. The histogram shows the raw counts while the solid black line shows the sum of the individual Gaussian profiles fitted to the data. Lower panel represents the residuals of the fitting. The amplitudes, pixel positions, and the Doppler widths of these three lines are listed at the bottom of this plot.

double gaussian fit is highly unreliable in this case and because of this reason we excluded this line.

- **Fe** II (λ1250.629 Å) and **Si** II (λ1250.467 Å) are blended with each other and are not strong enough.

- **P** I (λ1248.203 Å) and **S** I (λ1248.048 Å) lines are blended together and the profile is affected by the edge of the coated part of the detector (Figure 3.5).

- **C** II (λ1247.391 Å) line is very asymmetric on its right wing and located between two groups of strong lines.

Because of the mentioned reasons we have decided to exclude all these lines.
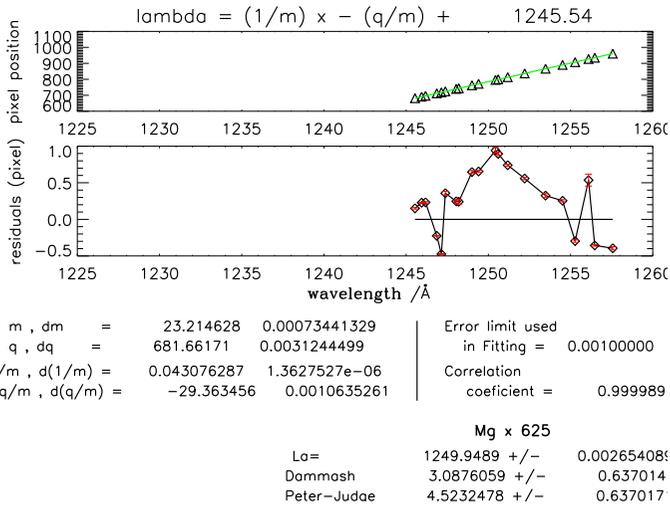
Figure 3.11: Part 2, Mg x, 20 reference chromospheric lines, ($\lambda = 0.043076287\,x + 1216.1745$)

3.1.4.4   Part 2 [1246-1260 Å]: linear fitting of 9 reference lines

Using the remaining 9 lines and performing a linear fit gives a dispersion relation of (Fig. 3.13):

$$\lambda = 0.043128624\,x + 1216.1232$$

The values of λ are listed in the fifth column of Table 3.7 (called λ_{Sun}). Residuals are between $\pm$ 0.6 pixels (6 km s^{-1}). If we choose a subset of these lines and perform the linear fit again, the residuals will not improve any more. Eight neutral lines of C I and one single ionized Mn II are chosen to be the chromospheric lines for calibration at this level. As it is shown in Figure 3.13, the residuals looks to have a parabolic shape. Therefore, we tried to fit a second order polynomial curve to see if there is any improvement in the residuals.

3.1.4.5   Part 2 [1246-1260 Å]: second order polynomial fitting of 9 reference lines

A second order polynomial curve fit to those nine lines leads to a dispersion relation like (Eqs. 3.5 and 3.6):

$$x = -0.026987775\,(\lambda - 1245.5380)^2 + 23.467392\,(\lambda - 1245.5380) + 681.78118$$

$$\lambda = \frac{-23.467392 + \sqrt{550.71849 + 0.10795110(681.78118 - x)}}{-0.053975549} + 1245.5380$$
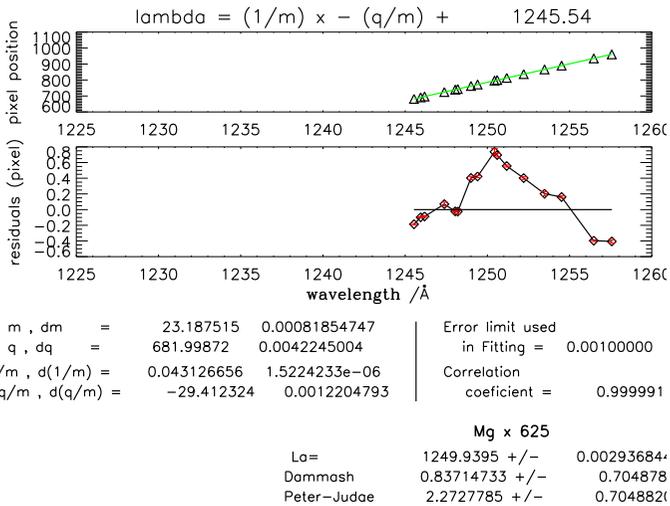
Figure 3.12: Part 2, Mg x, 16 reference chromospheric lines, (λ = 0.043126656 x + 1216.1256)

The list of λ values are represented in the sixth column of Table 3.7 (called λ_{Sun}). Figure 3.14 shows the residuals decreased by a factor of 10 and in the range of ± 0.05 pixels (0.5 km s^{-1}). It looks reasonable to accept this second order polynomial fit as our final and best calibration scale. These final reference lines for calibration are marked by sign (R) in the Fig. 3.5.
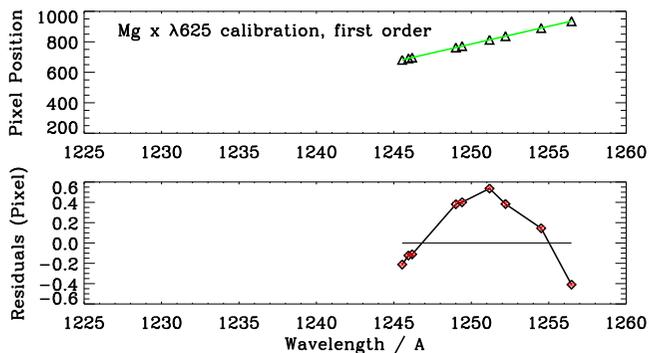
Figure 3.13: Part 2, Mg x, 9 reference chromospheric lines, (λ = 0.043128624 x + 1216.1232)
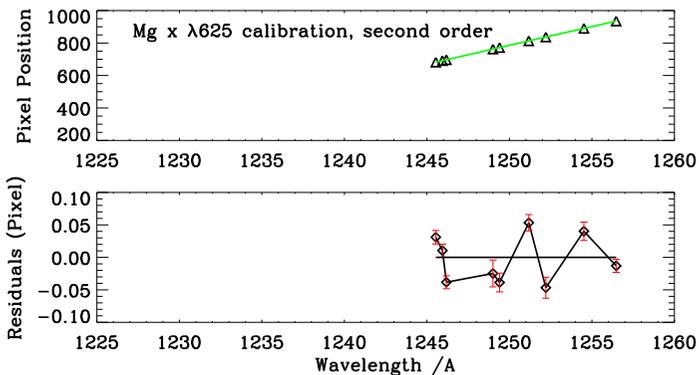

Figure 3.14: Part 2, Mg x, 9 reference chromospheric lines, second order polynomial fitting

3.1.4.6 Measured Doppler shift for Mg x line

As described in Section 3.1.2, using the wavelength scale obtained in the last Section (by performing a second order polynomial fit), the Doppler shift of Mg x 625 Å line and its measured uncertainty are obtained using Eqs. 3.10 and 3.11, respectively. The position of this line, λ_{Sun} is obtained by applying a single Gaussian fit to the spectrum of Mg x line and is 624.963 Å. Having the exact position of the line, the only value that we need to calculate the Doppler velocity is the rest wavelength of the line. There is no accurate laboratory wavelength measurement for the Mg x 625 Å line available. The two rest wavelength values given by Kelly (1987) and National Institute of Standards and Technology (NIST) database (Kaufman and Martin 1991), both are based on solar observations and performed in the early 1970s. Peter and Judge (1999) discussed about the accuracy of these rest wavelength measurements and concluded that those values at disk center are not reliable. Assuming the Mg x line is at rest[5] above the limb in the quiet corona[6], they have obtained a rest wavelength of 624.968 ± 0.007 Å for this line. Using the same assumption Dammasch et al. (1999a) measured a rest wavelength of 624.965 ± 0.003 Å for this line. Using the new obtained rest wavelengths they have obtained a blue shift of few km s^{-1}.

However, Chae et al. (1998) and Brekke et al. (1997) have used the Kelly (1987) rest wavelength (624.950 Å) and have obtained a red shift of few km s^{-1}. Figure 3.15 represents the different results for Mg x 625 line Doppler shifts using different rest wavelengths. Since the rest wavelength measurements done by Peter and Judge (1999) and Dammasch et al. (1999a) are more accurate than those from Kelly (1987), we have used the average of these two values as our final rest wavelength (624.967 Å), and obtained a blue shift of (1.8 ± 0.6 km s^{-1}) for the Mg x line. This result is in agreement with the Doppler shift obtained by Peter (1999), Peter and Judge (1999), Dammasch et al. (1999a). If we would accept the rest wavelength of Kelly (1987), our result would be in agreement with findings of Brekke et al. (1997), Chae et al. (1998).

Brekke et al. (1997) has discussed the possibility of blending in the right wing of the Mg x line from Si ɪɪ 1250.089 Å and concluded that the effect is negligible. Dammasch et al. (1999a) also reported and considered the presence of this blending on their off-limb spectra. Chae et al. (1998) also reported the presence of some asymmetry in the spectra of Mg x and performed a double Gaussian curve fit to find the position of this line. They mentioned that the closest laboratory wavelength to this observed line position is either Si ɪɪ 1250.089 Å (first order) or Si ɪɪɪ 624.997 Å (second order) but none of these two lines give a reasonable Doppler shift that matches with the typical Doppler shifts of lines formed at their formation temperature. They mentioned the identification of this line is uncertain.

Though our Mg x profile was well symmetric, we have also applied a double Gaussian fit to the Mg x line spectrum to check the possibility of any blending. We did not find a significant change between single and Double Gaussian fits and residuals of the fitting. Therefore, we conclude that we do not see any significant blending on the Mg x line. Table 3.8 summarizes the difference between the Doppler shifts obtained by different rest

---

[5]having zero line-of-sight Doppler shift off-limb since the bulk motions out of the plane of sky cancel out each other.

[6]A region void of prominent structures (i.e., prominences or loops) and away from active regions.

wavelengths.
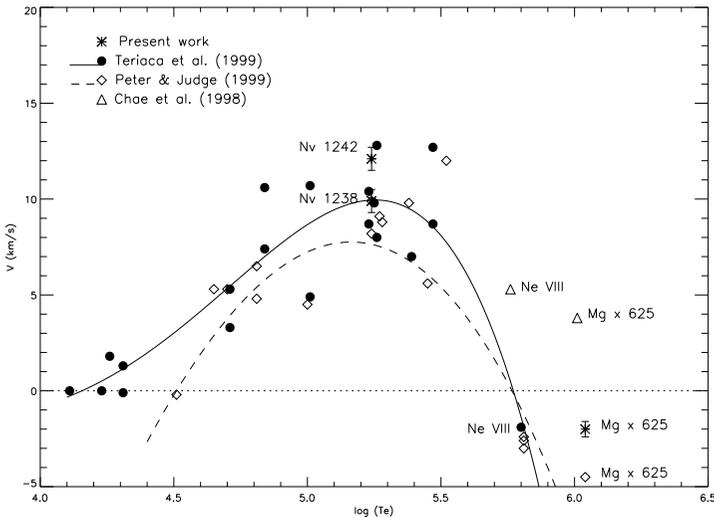
Figure 3.15: Variation of Doppler shift on the quiet sun disk center for various ions measured from SUMER spectra. Filled circles are values from Teriaca et al. (1999a) and diamonds represent the results of Peter and Judge (1999). Triangles show the Doppler shift of Mg x and Ne VIII ions from Chae et al. (1998). Solid and dashed lines represent the fourth order polynomial curve fitted to the Teriaca et al. (1999a) results, and the third order polynomial curve fitted to the Peter and Judge (1999) results, respectively. The difference in choosing the rest wavelengths between Peter and Judge (1999) and Chae et al. (1998) causes this large difference between the corresponding measured Doppler shifts for Mg x line (same happens to the Ne VIII line, as well). Asterisks show our present results. For N v 1238 Å and 1242 Å lines we have used the rest wavelengths measured by Edlén (1942). The Doppler shift of Mg x 625 Å is measured with a rest wavelength of (624.967 Å) which is the average of the rest wavelengths obtained by Peter and Judge (1999) and Dammasch et al. (1999a). No significant blending is observed for this line in our measurements.

3.2   EIS/Hinode data: analysis and co-alignment

The Extreme ultraviolet Imaging Spectrometer (EIS), observes the upper transition region and corona of the Sun in the two wavelength ranges (170-210 Å and 250-290 Å). EIS has a wider field of view up to 560×512 arcsec[2] with spatial resolution of 1 arcsec (see Section 2.2). EIS spectra are used to measure the average Doppler shift of coronal lines with formation temperatures between 1MK and 2MK over the quite Sun (see Chapter 4)

and a moss region (see Chapter 5). EIS data are saved as FITS files that can be retrieved from the instrument web page[7].

EIS Y-offset

$y = +8.72e\text{-}02*x -1.70e\text{+}01$

EIS Y-offset

$y = +7.68e\text{-}02*x -3.49e\text{+}00$
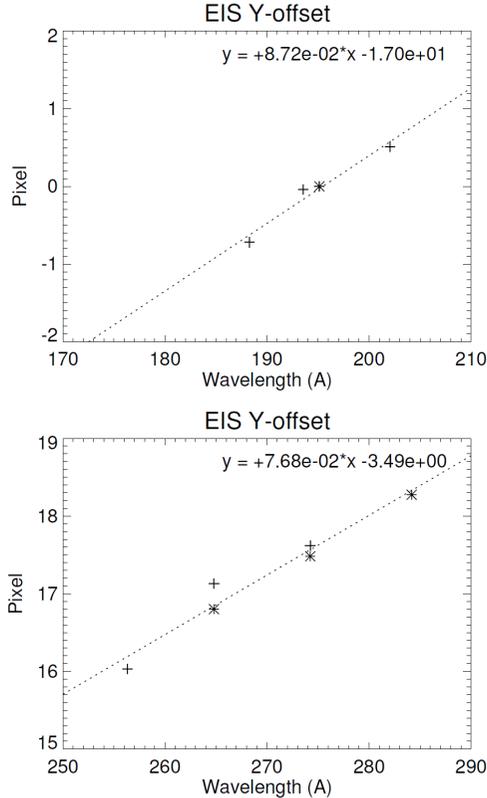
Figure 3.16: The offset of EIS CCDs in Y direction with respect to Fe XII 195.12 Å wavelength, which is a function of the wavelength (courtesy of Suguru Kamio and Hirohisa Hara 2008).

Using the standard EIS data reduction routine (in SolarSoft, SSW, software library) **eis_prep.pro** we calibrate the raw level 0 EIS data and create the level 1 data that can be used for scientific studies. The level 1 EIS data have been corrected by:

- Subtraction of the dark current

- Removing cosmic rays and hot pixels

[7]http://msslxr.mssl.ucl.ac.uk:8080/SolarB/SearchArchive.jsp

61

- Radiometric calibration to convert DN values to intensity units (erg cm^{-2} s^{-1} sr^{-1} Å^{-1})

The details are described in an EIS software note[8] (author P. Young). After applying **eis_prep.pro** to obtain level 1 EIS data, we still need to do some corrections on the data set. In the next Subsections we will describe these points.

3.2.1   Slit tilt

As mentioned in Section 2.2, the EIS spectrometer has four slits (1", 2", 40" and 266"). The slits, the grating rules, and the CCD rows are not perfectly aligned. This fact causes the center of the spectral lines to deviate when going up along the solar Y axis. Since to obtain the Doppler shifts we need to measure the exact center of the lines, correcting this systematic error in line position along the slit becomes very important[9]. Kamio et al. (2010), by performing a linear fit to the measured line centers of the Fe XII 195.120 Å (which is the brightest line of the EIS) along the slit, obtained the corresponding tilt for each Y pixel position of the slits. This amount of the tilt could be corrected automatically by using the SSW routine **eis_slit_tilt.pro**.

3.2.2   Orbital variation

The orbit of the EIS aboard the Hinode spacecraft is a Sun-synchronous one with a period of 98.5 minutes that enables Hinode to observe the Sun almost continuously. The Hinode's orbit around the Earth causes the temperature of the EIS spectrometer to change during each revolution[10]. This thermal change shifts the spectral line positions quasi-periodically. Correcting this effect in velocity measurement studies is very important. Kamio et al. (2010), using an artificial neural network, developed an empirical model to correct the spectrum for this effect. The SSW routine **eis_wave_corr.pro** removes this effect automatically. However, in our technique to obtain the Doppler shifts (see Section 4.4) since we are measuring the difference between the line positions (not the position of a single line), removing this effect is neither necessary, nor important.

3.2.3   Spatial offset of the two EIS CCDs in X direction

Between emission lines registered in the SW band (170-210 Å) and the ones on LW band (250-290 Å) in X direction, there was an offset of about 2 arcsec. As it is mentioned by Young et al. (2007b), it means that during the raster scanning process over a target area on the Sun a reference feature first appears on the short wavelength (SW) band, and later appears in the long wavelength (LW) band. The reason is that, the two images forming on SW and LW bands are originating from different halves of the primary mirror and the focal points of these halves are not exactly the same. After adjusting the position of the slit on 24 August 2008, the amount of this offset decreased to about 0.5 arcsec[11].

---

[8] ftp://sohoftp.nascom.nasa.gov/solarsoft/hinode/eis/doc/eis_notes/01_EIS_PREP/eis_swnote_01.pdf

[9] ftp://sohoftp.nascom.nasa.gov/solarsoft/hinode/eis/doc/eis_notes/04_SLIT_TILT/eis_swnote_04.pdf

[10] ftp://sohoftp.nascom.nasa.gov/solarsoft/hinode/eis/doc/eis_notes/05_WAVELENGTH_CORRECTION/eis_swnote_05.pdf

[11] http://msslxr.mssl.ucl.ac.uk:8080/eiswiki/Wiki.jsp?page=CCDOffsetX

3.2.4 Spatial offset of the two EIS CCDs in Y direction

While tracking a feature on the two SW and LW bands, we have to be careful about the average 16 arcsec offset of the two CCDs in Y direction. Suguru Kamio and Hirohisa Hara[12] 2008 using the Mercury transit seen by EIS slot observations showed that this offset is a function of wavelength. Figure 3.16 shows the result of their work. The offset of the EIS CCDs in Y direction with respect to Fe XII 195.12 Å is represented there. They introduced the Eqs. (3.13) and (3.14) to calculate the amount of Y offset (Y) with respect to Fe XII 195.12 Å for each wavelength (X) on SW and LW bands, respectively.

$$Y = +8.72 \times 10^{-2}X - 17.00, \qquad (3.13)$$

and

$$Y = +7.68 \times 10^{-2}X - 3.49. \qquad (3.14)$$

3.2.5 co-alignment of EIS and SUMER

Using the intensity contours of a pair of lines that have similar formation temperature (like N v 1238 Å and He II 256 Å, or Mg x 625 Å and Fe x 184 Å), the co-alignment of SUMER and EIS spectrometers are performed with an accuracy of about 1 arcsec (Fig. 4.4). Details are described in Section 4.3.2.

3.2.6 Wavelength calibration and Doppler shift measurements

EIS does not have any on-board calibration lamp and it also does not cover the cool chromospheric lines. A possible method would be to use off-limb spectra along with the solar disk data and to assume that the line-of-sight Doppler shift off-limb is zero on average. This is only possible if the off-limb and the on-disk data are taken with the same exposure. If the exposures off-limb and on-disk are taken separately, due to the orbital thermal variation of EIS the conditions will change and a calibration is not possible (look to Appendix A, Young et al. 2012).

Because of all these limitations, the most common way to calibrate the EIS spectra is to calibrate it with respect to the quiet Sun spectrum which is recorded simultaneously along with the on-disk active region data (both quiet Sun and target area on-disk should be within a same exposure along the slit). It is only possible if the EIS field of view is large enough to contain both quiet and active on-disk areas. Then by adding up the quiet Sun average Doppler shifts obtained using data at longer wavelengths (where suitable chromospheric lines are observed) such as those from SUMER (i.e., Teriaca et al. 1999a, Peter and Judge 1999), the absolute Doppler shifts could be obtained (Young et al. 2012). As mentioned by Young et al. (2012), this way is also not very accurate because the quiet Sun in transition region temperatures is highly dynamic and the Doppler shift pattern of the quit Sun studied by Teriaca et al. (1999a) and Peter and Judge (1999) could be very different from the one studied later on (and in close proximity to an active region) using EIS spectrometer.

Using the simultaneous observations of EIS and SUMER over a target area on-disk, together with recording the EIS off-limb spectrum over a quiet corona we have developed

---

[12]http://msslxr.mssl.ucl.ac.uk:8080/eiswiki/attach/CCDOffset/yoffset.pdf

a novel method to establish an absolute wavelength scale (with respect to the chromospheric lines). The method is described in detail in Section 4.3.2 and allows us to calculate the absolute Doppler shifts of EIS coronal lines (described in Section 4.4).

3.3   EIT/SoHO

The Extreme ultraviolet Imaging Telescope (EIT), provides full disk images of the Sun in four UV narrow passbands with spatial resolution of about 5 arcsec (see Section 2.3). We have used the Fe XII 195 Å images of EIT to find our target area in the quiet sun study. The study is fully described in chapter 4. EIT level zero fits files are accessible through the EIT WWW catalog[13]. Using **eit_prep.pro** SSW routine, the calibration steps are applied[14], such as:

- Subtracting the dark current

- De-gridding to correct the shadow of the supporting grid of the aluminum filter that falls on the CCD detector and creates a modulation pattern

- Normalization of the filter

- Normalization of the exposure time

- Flat field correction

- Correction for cosmic rays

The details of each correction is described in detail by Delaboudinière et al. (1995), Dere et al. (2000). The closest full Sun EIT image in time, with respect to the time of Quite Sun observation during EIS-SUMER campaign (HOP 3), is chosen (04:12:09 UTC). Intensity contours of Fe XII 195 Å are plotted on top of the EIS raster image to perform the co-alignment of the two instrument (Figure 3.17). Left panel represents a wide view image of quite Sun taken by the EIT telescope in Fe XII 195 Å line. The light blue box shows the SUMER field of view during this campaign. Right panel is a blow up of the light blue box scanned by EIS in the Fe XII 195 Å line during HOP3.

3.4   AIA/SDO

The Atmospheric Imaging Assembly (AIA) is a EUV telescope that provides high resolution (spatial resolution of 1.5 arcsec) images of the full solar disk with the cadence of 12 seconds (see Section 2.4). The images of AIA in different channels are used here to get an idea about the structure of NOAA active region 11243 (specially its' moss region), with respect to the temperature. The details of the study is described in chapter 5. The initial calibration of AIA is described by Boerner et al. (2012). More detailed information

---

[13]http://umbra.nascom.nasa.gov/eit/eit-catalog.html
[14]http://umbra.nascom.nasa.gov/eit/eit_guide/calibration.htm
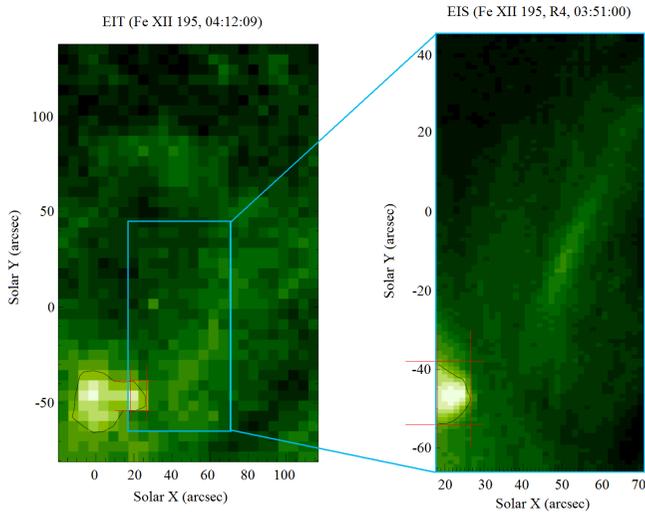
Figure 3.17: Left panel shows the quite Sun image in the Fe XII 195 Å line taken by EIT. Black line is a contour of high intensity area in the EIT image over-plotted on both panels (both, images taken by EIT and EIS). Light blue box shows the field of view of SUMER. Right panel shows the same field of view as the light blue box but scanned by EIS in the Fe XII 195 Å line during HOP3.

about AIA calibration could be found on the instrument web page[15]. The AIA has three different data levels[16]:

- Level 0 which is the raw telemetry data.

- Level 1.0 that is corrected for bad pixels, despiking (removing spikes formed because of the collisions of high energy particles – e.g., cosmic rays – with the detectors), and flat field.

- The different channel images have different roll angles, and different plate scales. The **aia_prep.pro** SSW routine corrects these effects and creates the level 1.5 AIA data.

The AIA data is accessible from the web[17].

---

[15]https://www.lmsal.com/sdodocs/doc/dcur/SDOD0060.zip/zip/entry/
[16]http://solar-center.stanford.edu/sdo/SDO_Guide.pdf
[17]http://www.lmsal.com/get_aia_data/
http://jsoc.stanford.edu/data/aia/

Table 3.1: First step identified chromospheric reference lines. Laboratory wavelengths are from Kelly (1987).

	Line Pixel position	$\pm\delta x$ (in pixels)	Doppler width (in pixels)	λ_{Sun} Å	λ_{lab}(Reference) Å	ID	
1	960.46924	0.02267	2.07463	1257.588	1257.565	C I	
2	935.08850	0.00956	2.84256	1256.494	1256.470	Mn II	
3	927.22809	0.08155	3.05576	1256.154	1256.093	S I	
4	907.42865	0.01665	2.83624	1255.300	1255.276	Si I	
5	890.26746	0.01412	1.67294	1254.560	1254.513	C I	
6	866.28564	0.02628	1.15232	1253.526	1253.484	Ni II	
7	865.03357	0.02874	3.58388	1253.471	1253.430	C I	★
8	837.06140	0.01618	1.91583	1252.265	1252.208	C I	
9	813.28583	0.01254	2.02121	1251.239	1251.176	C I	
10	800.00006	0.02407	1.66606	1250.666	1250.597	Fe II	
11	796.23853	0.04022	2.02314	1250.504	1250.433	Si II	
12	772.08740	0.01449	2.33583	1249.462	1249.405	C I	
13	762.77032	0.02067	1.65779	1249.060	1249.004	C I	
14	743.69977	0.03138	1.58518	1248.237	1248.200	P I	
15	740.10773	0.00951	1.39782	1248.082	1248.045	S I	
16	736.92926	0.03142	4.51424	1247.945	1247.867	C I	★
17	724.84985	0.02465	3.25374	1247.424	1247.383	C II	
18	718.42310	0.00579	1.90772	1247.147	1247.142	P I	
19	712.17297	0.00485	2.19386	1246.877	1246.862	C I	
20	696.79791	0.00975	1.63620	1246.214	1246.180	C I	
21	691.29150	0.00586	2.04333	1245.977	1245.943	C I	
22	681.81219	0.01039	1.75633	1245.568	1245.538	C I	
23	673.74139	0.00774	1.77795	1245.220	1245.183	C I	
24	669.41620	0.01261	1.82201	1245.033	1244.996	C I	
25	658.42096	0.00561	1.95439	1244.559	1244.535	C I	
26	649.47412	0.04367	1.46446	1244.173	1244.127	C I	
27	646.47467	0.01961	1.80746	1244.043	1243.998	C I	
28	641.43951	0.02202	2.14205	1243.826	1243.784	C I	
29	635.20032	0.04423	2.05543	1243.557	1243.518	C I	
30	630.47852	0.03317	1.71452	1243.353	1243.313	N I	
31	627.38904	0.02090	1.73144	1243.220	1243.179	N I	
32	598.57794	0.01316	3.70517	1241.977	1241.972	P I	★
33	598.05859	0.05987	0.88820	1241.955	1241.928	Fe II	
34	562.56183	0.05374	2.85791	1240.423	1240.395	Mg II	
35	551.51062	0.11342	2.72369	1239.947	1239.925	Mg II	
36	526.40210	0.01118	4.08751	1238.864	1238.840	Mn II	

http://sdo.gsfc.nasa.gov/data/aiahmi/
http://www.mps.mpg.de/projects/seismo/GDC-SDO/data.htm

37	503.67737	0.12817	1.14373	1237.883	1237.930	Fe II	★
38	495.97427	0.09392	1.35912	1237.551	1237.590	Mn II	★
39	489.14981	0.26798	1.55724	1237.257	1237.247	N II	
40	485.14609	0.02001	1.90823	1237.084	1237.049	Ni II	
41	459.56906	0.09602	1.39232	1235.981	1235.920	Si II	★
42	451.97525	0.01749	1.87671	1235.653	1235.624	S I	
43	419.68594	0.62493	5.80050	1234.260	1234.300	N I	★
44	415.30487	0.13115	2.77911	1234.071	1234.092	Ni II	★
45	407.30722	0.12337	1.56746	1233.726	1233.661	Fe II	★
46	381.83755	0.06355	3.19651	1232.627	1232.687	P I	★
47	342.58646	0.15205	1.29201	1230.934	1230.927	Fe II	
48	330.69598	0.04057	3.29772	1230.421	1230.374	S I	★
49	312.23608	0.01824	2.15175	1229.625	1229.608	S I	

Table 3.2: The 18 identified chromospheric lines in the part of the spectrum containing the N v lines. Laboratory wavelengths are from Kelly (1987).

	Line pixel position	±δx (in pixels)	Doppler width (in pixels)	λ_{Sun} Å	λ_{lab}(Reference) Å	ID	
1	673.74139	0.00774	1.77795	1245.185	1245.183	C I	
2	669.41620	0.01261	1.82201	1244.999	1244.996	C I	
3	658.42096	0.00561	1.95439	1244.525	1244.535	C I	★
4	649.47412	0.04367	1.46446	1244.139	1244.127	C I	★
5	646.47467	0.01961	1.80746	1244.010	1243.998	C I	★
6	641.43951	0.02202	2.14205	1243.793	1243.784	C I	★
7	635.20032	0.04423	2.05543	1243.524	1243.518	C I	
8	630.47852	0.03317	1.71452	1243.321	1243.313	N I	
9	627.38904	0.02090	1.73144	1243.187	1243.179	N I	
10	598.05859	0.05987	0.88820	1241.924	1241.928	Fe II	
11	562.56183	0.05374	2.85791	1240.394	1240.395	Mg II	
12	551.51062	0.11342	2.72369	1239.918	1239.925	Mg II	★
13	526.40210	0.01118	4.08751	1238.836	1238.840	Mn II	★
14	489.14981	0.26798	1.55724	1237.230	1237.247	N II	★
15	485.14609	0.02001	1.90823	1237.058	1237.049	Ni II	
16	451.97525	0.01749	1.87671	1235.628	1235.624	S I	
17	342.58646	0.15205	1.29201	1230.914	1230.927	Fe II	★
18	312.23608	0.01824	2.15175	1229.606	1229.608	S I	

Table 3.3: Final chosen chromospheric lines for wavelength calibration in the part of the spectrum containing the N v lines. Reference wavelengths are from Kelly (1987).

	Line pixel position	$\pm\delta x$ (in pixels)	Doppler width (in pixels)	λ_{Sun} Å	λ_{lab}(Reference) Å	ID
1	673.74139	0.00774	1.77795	1245.182	1245.183	C I
2	669.41620	0.01261	1.82201	1244.995	1244.996	C I
3	635.20032	0.04423	2.05543	1243.521	1243.518	C I
4	630.47852	0.03317	1.71452	1243.317	1243.313	N I
5	627.38904	0.02090	1.73144	1243.184	1243.179	N I
6	598.05859	0.05987	0.88820	1241.920	1241.928	Fe II
7	562.56183	0.05374	2.85791	1240.391	1240.395	Mg II
8	485.14609	0.02001	1.90823	1237.055	1237.049	Ni II
9	451.97525	0.01749	1.87671	1235.626	1235.624	S I
10	312.23608	0.01824	2.15175	1229.604	1229.608	S I

Table 3.4: Average Doppler shift for N v lines. The second and third columns represent the results of the linear wavelength calibration with the 10 suitable chromospheric lines (listed in Table 3.3).

	Kelly (1238.821 Å, 1242.804 Å)	Edlén (1238.800 Å, 1242.778 Å)
N v 1238 Å	4.81 ± 0.59	9.89 ± 0.59
N v 1242 Å	5.86 ± 0.64	12.14± 0.64

Table 3.5: The 20 identified chromospheric lines in the part of the spectrum containing the Mg x line. Laboratory wavelengths are from Kelly (1987).

	Line pixel position	±δx (in pixels)	Doppler width (in pixels)	λ_{Sun} Å	λ_{lab}(Reference) Å	ID	
1	960.46924	0.02267	2.07463	1257.541	1257.542	C I	
2	935.08850	0.00956	2.84256	1256.448	1256.470	Mn II	
3	927.22809	0.08155	3.05576	1256.109	1256.110	S I	★
4	907.42865	0.01665	2.83624	1255.256	1255.257	Si I	★
5	890.26746	0.01412	1.67294	1254.517	1254.513	C I	
6	866.28564	0.02628	1.15232	1253.484	1253.484	Ni II	
7	837.06140	0.01618	1.91583	1252.225	1252.208	C I	
8	813.28583	0.01254	2.02121	1251.201	1251.176	C I	
9	800.00006	0.02407	1.66606	1250.629	1250.629	Fe II	
10	796.23853	0.04022	2.02314	1250.467	1250.467	Si II	
11	772.08740	0.01449	2.33583	1249.426	1249.405	C I	
12	762.77032	0.02067	1.65779	1249.025	1249.004	C I	
13	743.69977	0.03138	1.58518	1248.203	1248.203	P I	
14	740.10773	0.00951	1.39782	1248.049	1248.048	S I	
15	724.84985	0.02465	3.25374	1247.391	1247.391	C II	
16	718.42310	0.00579	1.90772	1247.116	1247.114	P I	★
17	712.17297	0.00485	2.19386	1246.845	1246.845	C I	★
18	696.79791	0.00975	1.63620	1246.183	1246.180	C I	
19	691.29150	0.00586	2.04333	1245.946	1245.943	C I	
20	681.81219	0.01039	1.75633	1245.537	1245.538	C I	

Table 3.6: The 16 identified chromospheric lines in the part of the spectrum containing the Mg x line. Laboratory wavelengths are from Kelly (1987).

	Line pixel position	±δx (in pixels)	Doppler width (in pixels)	λ_{Sun} Å	λ_{lab}(Reference) Å	ID	
1	960.46924	0.02267	2.07463	1257.541	1257.542	C I	★
2	935.08850	0.00956	2.84256	1256.447	1256.470	Mn II	
3	890.26746	0.01412	1.67294	1254.515	1254.513	C I	
4	866.28564	0.02628	1.15232	1253.481	1253.484	Ni II	★
5	837.06140	0.01618	1.91583	1252.221	1252.208	C I	
6	813.28583	0.01254	2.02121	1251.196	1251.176	C I	
7	800.00006	0.02407	1.66606	1250.623	1250.629	Fe II	★
8	796.23853	0.04022	2.02314	1250.461	1250.467	Si II	★
9	772.08740	0.01449	2.33583	1249.420	1249.405	C I	
10	762.77032	0.02067	1.65779	1249.018	1249.004	C I	
11	743.69977	0.03138	1.58518	1248.196	1248.203	P I	★
12	740.10773	0.00951	1.39782	1248.041	1248.048	S I	★
13	724.84985	0.02465	3.25374	1247.384	1247.391	C II	★
14	696.79791	0.00975	1.63620	1246.174	1246.180	C I	
15	691.29150	0.00586	2.04333	1245.937	1245.943	C I	
16	681.81219	0.01039	1.75633	1245.528	1245.538	C I	

Table 3.7: The 9 identified chromospheric lines in the part of the spectrum containing the Mg x line. Laboratory wavelengths are from Kelly (1987).Kelly (1987).

	Line pixel position	±δx (in pixels)	Doppler width (in pixels)	λ_{Sun} Å (linear fit)	λ_{Sun} Å (quadratic fit)	λ_{lab} Å (Reference)	ID
1	935.08850	0.00956	2.84256	1256.452	1256.469	1256.470	Mn II
2	890.26746	0.01412	1.67294	1254.519	1254.515	1254.513	C I
3	837.06140	0.01618	1.91583	1252.225	1252.206	1252.208	C I
4	813.28583	0.01254	2.02121	1251.199	1251.178	1251.176	C I
5	772.08740	0.01449	2.33583	1249.422	1249.403	1249.405	C I
6	762.77032	0.02067	1.65779	1249.020	1249.003	1249.004	C I
7	696.79791	0.00975	1.63620	1246.175	1246.178	1246.180	C I
8	691.29150	0.00586	2.04333	1245.938	1245.943	1245.943	C I
9	681.81219	0.01039	1.75633	1245.529	1245.539	1245.538	C I

Table 3.8: Average Doppler shift for Mg x line using different rest wavelengths.

	Doppler shift (km s^{-1})
Peter and Judge (1999) (624.968 Å)	-2.51 ± 0.39
Dammasch et al. (1999a) (624.965 Å)	-1.08 ± 0.39
Kelly (1987) (624.950 Å)	6.13 ± 0.39
Dadashi et al. (2011) (624.967 Å)	-1.80 ± 0.59

4 The quiet Sun average Doppler shift of coronal lines up to 2 MK[1]

4.1 Abstract

The average Doppler shift shown by spectral lines formed from the chromosphere to the corona reveals important information on the mass and energy balance of the solar atmosphere, providing an important observational constraint to any models of the solar corona. Previous spectroscopic observations of vacuum ultra-violet (VUV) lines have revealed a persistent average wavelength shift of lines formed at temperatures up to 1 MK. At higher temperatures, the behaviour is still essentially unknown.

Here we analyse combined SUMER (Solar Ultraviolet Measurements of Emitted Radiation)/SoHO (Solar and Heliospheric Observatory) and EIS (EUV Imaging Spectrometer)/Hinode observations of the quiet Sun around disk centre to determine, for the first time, the average Doppler shift of several spectral lines formed between 1 and 2 MK, where the largest part of the quiet coronal emission is formed. The measurements are based on a novel technique applied to EIS spectra to measure the difference in Doppler shift between lines formed at different temperatures. Simultaneous wavelength-calibrated SUMER spectra allow establishing the absolute value at the reference temperature of $T \approx$ 1 MK.

The average line shifts at 1 MK $< T < 1.8$ MK are modestly, but clearly bluer than those observed at 1 MK. By accepting an average blue shift of about (-1.8 ± 0.6) km s^{-1} at 1 MK (as provided by SUMER measurements), this translates into a maximum Doppler shift of (-4.4 ± 2.2) km s^{-1} around 1.8 MK. The measured value appears to decrease to about (-1.3 ± 2.6) km s^{-1} at the Fe xv formation temperature of 2.1 MK. The measured average Doppler shift between 0.01 and 2.1 MK, for which we provide a parametrisation, appears to be qualitatively and roughly quantitatively consistent with what foreseen by 3-D coronal models where heating is produced by dissipation of currents induced by photospheric motions and by reconnection with emerging magnetic flux.

4.2 Introduction

Ultraviolet observations of the Sun near disk centre show a systematic net red shift of emission lines from the transition region (TR). Several vacuum ultra-violet (VUV: 16 to 200 nm) spectrometers with different spatial resolutions such as HRTS and those flown on

---

[1]This chapter is published as Dadashi et al. 2011.

Skylab, OSO 8, and SMM have revealed this phenomenon since the 1970s (e.g., Doschek et al. 1976, Hassler et al. 1991, Brekke 1993, Achour et al. 1995). Systematic red shifts have also been observed in spectra of late type stars (e.g., Ayres et al. 1988, Wood et al. 1996, Pagano et al. 2004), indicating that this phenomenon is not unique to the Sun.

In these earlier investigations (before the launch of SoHO in 1995), the magnitude of the red shift was found to increase with temperature, reaching a maximum at $T = 0.1$ MK and then decreasing toward higher temperatures. However, these observations were, with few exceptions, restricted to temperatures below 0.2 MK.

Observations from SOHO extended the observable temperature range up to about 1 MK. In the quiet Sun near disk centre, Doppler shifts in the range of 10 to 16 km s^{-1} were confirmed in lines formed from $T = 0.1$ MK to 0.25 MK (e.g., Brekke et al. 1997, Chae et al. 1998, Peter and Judge 1999, Teriaca et al. 1999a).

At higher temperatures (0.6 to 1 MK), the interpretation of the measurements proved to be more controversial. Brekke et al. (1997) and Chae et al. (1998) reported red shifted (downward) average Doppler velocities of 6.0 and 3.8 km s^{-1} for Mg x λ625 ($T = 1.0$ MK) and of 5.0 and 5.3 km s^{-1} for Ne vⅢ770 ($T = 0.63$ MK). These Doppler velocities were derived by using the reference rest wavelengths of 770.409 Å and 624.950 Å compiled by Kelly (1987) (based on solar observations, see discussion in Peter and Judge 1999), affected by high uncertainties (high in relation to the Doppler shifts under discussion).

Peter and Judge (1999) and Dammasch et al. (1999a,b) took another approach and obtained accurate rest wavelengths for the above lines by assuming that the average Doppler velocity is around zero above the solar limb (motions along the line of sight cancel out on average in an optically thin plasma). With these new rest wavelengths, average *blue shifts* of a few km s^{-1} were found for both lines near disk centre (Peter 1999, Peter and Judge 1999, Dammasch et al. 1999a,b, Teriaca et al. 1999a). These results suggest that there is a transition from red to blue shifts above 0.5 MK. This transition is an important observational constraint to distinguish between different models of the solar transition region.

Several hypotheses to explain the observed shifts of TR and coronal lines have been discussed in the literature. Since spicules carry an upward mass flux about 100 times larger than carried out by the global solar wind, it was suggested that the TR emission is dominated by downflowing, cooling plasma injected into the corona by spicules (Pneuman and Kopp 1978, Athay and Holzer 1982, Athay 1984). Lack of direct observational evidence (Withbroe 1983) and failure of theoretical models to reproduce observations (Mariska 1987) have led to a general dismissal of this hypothesis. However, recent analysis of spectroscopic and imaging VUV data with high sensitivity and spatial resolution has revived interest in the role of spicules in the mass and energy balance of the solar corona (e.g., De Pontieu et al. 2009, McIntosh and De Pontieu 2009a,b, De Pontieu et al. 2011).

Much effort has also been put into modelling the effect of energy deposition (e.g., mimicking the effect of magnetic reconnection in different regions of the solar atmosphere) on line profiles. Cheng (1992) showed that impulsive energy release in the photosphere generates a shock train that propagates upward and lifts and heats the chromosphere and TR, giving rise to an average downward material velocity. However, Hansteen and Wikstol (1994) demonstrated that, contrary to observations, the resulting line emission is nevertheless blue shifted. Instead of upward propagating waves, Hansteen (1993)

interpreted the observed red shift as caused by downward propagating acoustic waves. Nanoflares releasing relatively small amounts of energy near the top of the magnetic loops give rise to disturbances running downward along the loop legs. In a later study Hansteen et al. (1997) included the effect of reflection in the chromosphere of downward propagating MHD waves. This increases the red shifts in the TR, although coronal blue shifts become too high. An investigation by Judge et al. (1998) lends observational support to the picture of downward running waves or disturbances.

More generally, models of energy deposition at TR temperatures in 1-D loops have managed to reproduce the observed TR red shifts and low corona blue shifts relatively well (Teriaca et al. 1999b, Spadaro et al. 2006).

Recently, three-dimensional (3-D) comprehensive numerical models of the solar atmosphere (from photosphere to corona) have been developed. In the model described by Peter et al. (2004, 2006), coronal heating is caused by the Joule dissipation of the currents that are produced when magnetic field is stressed and braided[2] by photospheric motions. This model does produce red shifts at TR temperatures but also in the low corona, where blue shifts are instead observed. Hansteen et al. (2010) extended that work and added the effects of episodic injections of emerging magnetic flux that reconnects with the existing field. Rapid, episodic heating of the upper chromospheric plasma to coronal temperatures naturally produces downflows in TR lines and slight upflows in low coronal lines. As suggested by the authors, the localised heating events occurring in the chromosphere generate high-speed flows in a wide range of temperatures that may be related to the high-speed upflows that have been deduced from significant blueward asymmetries in EIS/Hinode observations of many TR and coronal lines (Hara et al. 2008b, De Pontieu et al. 2009, McIntosh and De Pontieu 2009b,a) that have been linked to spicules (i.e., De Pontieu et al. 2011).

With the launch of the Extreme Ultraviolet Imaging Spectrograph (EIS, Culhane et al. 2007, Korendyke et al. 2006) aboard Hinode, high spectral and spatial resolution observations in intense spectral lines formed at temperatures above 1 MK have finally become available. In this work, by using combined SUMER (Solar Ultraviolet Measurement of Emitted Radiation)/SoHO and EIS/Hinode observations of the quiet Sun and a novel technique, we have characterised the Doppler shift versus temperature behaviour up to 2.1 MK.

In Section 4.3 of this chapter, we describe the SUMER data and their analysis. In addition, we determine the Doppler velocity for N v λ1238, N v λ1242, and Mg x λ625 lines in the quiet Sun near disk centre. We also discuss the EIS/Hinode data, their analysis, and their co-alignment with the SUMER data. In Section 4.4 of this chapter, we present our method to measure the average Doppler velocity of hot coronal ions using SUMER/SoHO and EIS/Hinode data. The rest Sections of this chaper (4.5 and 4.6), present results and conclusions, respectively.

---

[2]Spatially resolved magnetic braids has been very recently observed in the corona by Cirtain et al. (2013) using a very high resolution EUV telescope, Hi-C (The High resolution Coronal Imager). Hi-C was launched by a sounding rocket from MSFC/NASA, Harvard-Smithsonian CfA, Lockheed Martin, UCLan, and Lebedev Physical Institute. This instrument has 0.2 arcsec spatial resolution and 360×360 arcsec^2 field of view with cadence of 5.4 s.
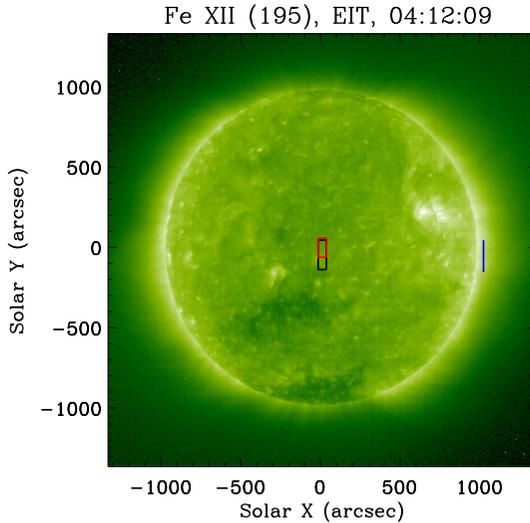
Figure 4.1: Fe xii 195 Å EIT image. The areas observed on the disk by SUMER (smaller red box) and EIS (larger black box) are shown. They are located near disk centre in a quiet region. The off-limb pointing of the EIS slit (about 50 arcsec above the west limb) is indicated by the vertical black line.

4.3   Observations and data analysis

Spectra of a quiet region near disk centre were taken on 6 April 2007 from 00:00 to 06:00 UTC during the first EIS-SUMER campaign (HOP 3). Figure 4.1 shows the Sun on the day of observations as recorded by the Extreme Ultraviolet Telescope EIT (Delabou-dinière et al. 1995) aboard SOHO. The quiet Sun areas observed by SUMER and EIS are visible near disk centre.

4.3.1   SUMER data: Doppler shift of Mg x and N v

SUMER is a normal incidence spectrograph operating over the wavelength range 450 Å to 1610 Å. It is a powerful UV instrument capable of making measurements of bulk motions in the chromosphere, TR, and low corona with a spatial resolution of 1 arcsec across and 2 arcsec along the slit and a spectral scale of ≈ 43 mÅ/pix at 1240 Å (first order) (Wilhelm et al. 1995, Lemaire et al. 1997), which is high enough to measure line shifts down to 1 km s^{-1}. Spectral images have been decompressed, wavelength-reversed, corrected for dead time, flat-field, and detector electronic distortion.

Since SUMER does not have an on-board calibration source, we derive the wavelength scale by using a set of chromospheric lines assumed to have negligible or low average Doppler shift on the quiet Sun. In short, calibrating takes three main steps:

Table 4.1: Doppler velocity of N v and Mg x lines:

ions (log (T/[K]))	rest wavelength [Å]	v [km s^{-1}]	δv [km s^{-1}]
N v (5.24)	1238.800	9.9	0.6
N v (5.24)	1242.778	12.1	0.6
Mg x (6.00)	624.967	-1.8	0.6

1. Identify the spectral lines by using the preliminary wavelength scale.

2. Find the exact pixel position of the lines by fitting Gaussian curves.

3. Perform a polynomial fit to find the dispersion relation.

To perform an accurate calibration we have to choose fairly strong and unblended lines from neutral and singly ionised atoms. For instance, Si i, S i, and C i transitions, occurring at temperatures between 6500 and 10000 K, are very suitable calibration lines, since lines formed at such temperatures show, on average, no substantial Doppler shifts (Samain 1991).

The SUMER data analysed here consist of a raster formed by 40 slit positions with a step size of 1.87 arcsec taken between 03:26 and 04:31 UTC by exposing through the 1 × 120 arcsec slit for 100 s. Recorded spectra cover the 1210 Å to 1270 Å range containing the N v lines at 1238.8 Å and 1242.8 Å (log(T/[K])=5.24) and the Mg x line at 625 Å (log(T/[K])=6.00). The above spectral range also contains a forbidden line of Fe xii at 1242 Å that would be ideal for a combined study with EIS. However, on the quiet Sun this line is weak and blended with chromospheric lines from Ca ii and S i (see Dammasch et al. 1999a) and, for this reason, it is not possible to derive its average Doppler shift with the accuracy needed for our study.

After checking that there are no significant instrumental drifts in the position of the spectral lines (either along the slit either in time across the raster) we have obtained a high signal to noise spectrum to be calibrated in wavelength. We have selected ten suitable reference lines in the part of the spectrum which contains the N v lines. A first-order polynomial fit of their positions in pixels versus their laboratory wavelengths, leaves residuals of less than ± 0.2 pixels (less than 2 km s^{-1}, see Fig. 4.2).

For the part of the spectrum containing the Mg x line, we have selected nine suitable reference lines. If we use a first-order polynomial fit to the line positions, the residuals up to ± 0.6 pixels (top panel of Fig. 4.3). The residuals clearly show the need for a second-order polynomial fit that yields residuals of ± 0.05 pixels (bottom panel of Fig. 4.3). The need for the higher order fit comes most likely from residuals in the correction of the electronic distortion of the detector image.

From the above analysis, for the N v $\lambda1238$ and $\lambda1242$ lines we find net red shifts of (9.9 ± 0.6) km s^{-1} and (12.1 ± 0.6) km s^{-1} by assuming the rest wavelengths to be 1238.800 Å and 1242.778 Å (Edlén 1934). These velocities agree with those from lines formed at similar temperatures reported in the literature (e.g., Brekke et al. 1997, Chae et al. 1998, Peter and Judge 1999, Teriaca et al. 1999a).
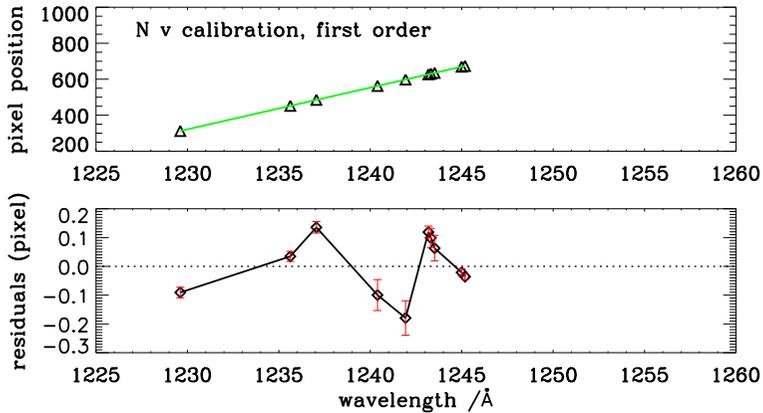
Figure 4.2: Upper panel: first-order polynomial fit to pixel positions versus rest wavelengths of 10 suitable reference lines around the N v lines. Lower panel: fit residuals are under 0.2 pixels (less than 2 km s^{-1}).

In the case of the Mg x λ625 line (observed in the second-order of diffraction), we use 624.967 Å as rest wavelength (average between the values of (624.965 ± 0.003) Å (Dammasch et al. 1999a) and (624.968 ± 0.007) Å (Peter and Judge 1999)), obtaining a Doppler velocity of (−1.8 ± 0.6) km s^{-1} (Table 4.1). With the above rest wavelength, the Doppler shifts measured in Mg x by Brekke et al. (1997) and Chae et al. (1998) would result in velocities of about 0 km s$^-$1 and −2 km s$^-$1, respectively.

Brekke et al. (1997) discuss a possible blend in the red wing of the Mg x λ625 line with a first-order Si II 1250.089 Å line and conclud that it has a negligible effect on the derived line shifts in spectra taken on the KBr-coated part of the SUMER detector. Teriaca et al. (2002) also discuss the relevance of blending from first-order lines to the Mg x line in the quiet Sun, concluding that they account for about 10% to 15% of the signal in the observed profile when observed on KBr (mostly from the Si II 1250.089 Å line) and to 1% to 2% when observed on the uncoated detector (due to the low sensitivity to first-order lines with respect to the KBr-coated parts). Since our observations were obtained on the uncoated part of the SUMER detector, we consider blends from first-order lines as entirely negligible.

Blends from second-order lines such as S x 624.70 Å, O IV 624.617 Å, and 625.130 Å are potentially more dangerous. However, these lines are far enough from the centre of the Mg x line and would produce detectable "shoulders" in the observed profile. Moreover, constrained double Gaussian fits show no significant improvement in line fitting over fits with a single Gaussian. This speaks against significant blending in the Mg x λ625 line also from second-order lines.
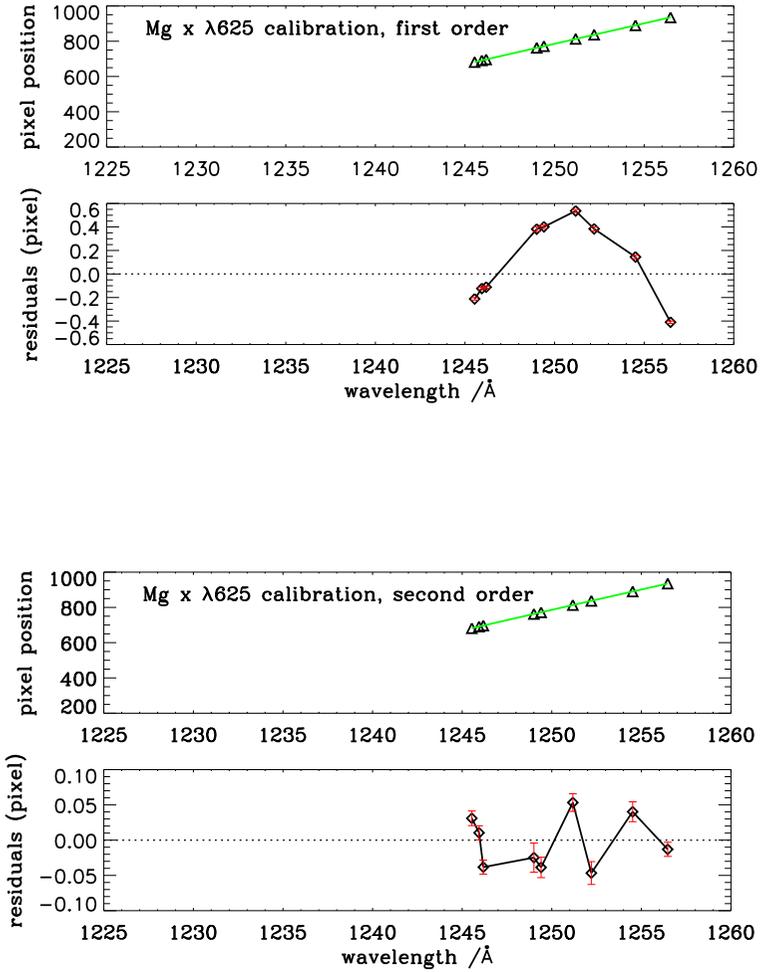
Figure 4.3: Top pair of panels: first-order polynomial fit to pixel positions versus rest wavelengths of 9 suitable reference lines around the Mg x lines. Residuals are large, up to 0.6 pixels. Bottom pair of panels: second-order polynomial fit to pixel positions versus rest wavelengths. Residuals lie within ± 0.05 pixels.

4.3.2 EIS data: analysis and co-alignment

The EIS instrument on Hinode produces high-resolution stigmatic spectra in the wavelength ranges of 170 to 210 Å and 250 to 290 Å. The instrument has 1 arcsec spatial pixels and 0.0223 Å spectral pixels. More details are given by Culhane et al. (2007) and Korendyke et al. (2006).

Our EIS data consist of four raster scans and one sit-and-stare sequence. The four scans were taken at disk centre on the same target area as observed by SUMER, whereas the sit-and-stare sequence was obtained above the limb. EIS rasters are obtaining by scanning from west to east, in the opposite direction to the SUMER data discussed here. Raster 4 is the closest in time to the SUMER scan. Data were reduced by using the software provided within SolarSoft.

After accounting for the offset between the short and the long wavelength ranges of EIS, we use pairs of radiance maps obtained in lines from similar (at least not too different) temperatures to perform a co-alignment between scans made by the two instruments with an accuracy of roughly 1 arcsec (see Fig. 4.4). The employed line pairs include N v λ1238 (log(T/[K])=5.24, SUMER) and He II λ256 (log(T/[K])=4.7, EIS), as well as Mg x λ625 (log(T/[K])=6.00, SUMER) and Fe x λ184 (log(T/[K])=6.00, EIS).

Since the wavelength range covered by EIS does not contain any suitable neutral or singly ionised line (He II λ256, besides being optically thick, is formed at too high a temperature to be un-shifted), an absolute wavelength calibration is not possible using the EIS data alone. We, therefore, take the approach of finding spectral lines recorded by the two instruments that are formed roughly at the same temperature by assuming that their average quiet Sun velocities are the same. Specifically, we assume that the average velocities of Mg x and Fe x ions are the same in the common observed area and equal to (-1.8 ± 0.6) km s^{-1}.

The above assumption requires some further consideration as it cannot be immediately excluded that the different ions have different velocities. In fact, mechanisms that can selectively heat and accelerate ions, such as ion-cyclotron resonance absorption of Alfvén waves (see, e.g., Tu and Marsch 1997, Marsch and Tu 1997), have long been considered as candidates for the solar wind acceleration. This mechanism is usually considered for low-density, open field regions such as coronal holes. However, Peter and Vocks (2003) claim that it may also operate at the base of open funnels in the quiet Sun, some 2 to 10 Mm above the photosphere. Since Fe x and Mg x have substantially different mass-to-charge ratios (6.2 and 2.7, respectively), the Fe x ions could be accelerated more (due to the lower gyro-frequency) and at lower heights (due to the expected fall-off of the magnetic field strength with height) than the Mg x ions. Thus, we may be underestimating the Fe x average outflow speed by taking it to be equal to that of Mg x. On the other hand, at slightly higher temperatures, we obtain very consistent results from lines of Fe xII and Si x that also have different mass-to-charge ratios (5.1 and 3.1), although the difference is smaller.

It should also be noted that Fe and Mg have very similar first ionisation potentials (FIP), excluding eventual differences in the average flows due to the fractionation processes believed to occur in the chromosphere (see, e.g., Laming 2004).

From the above considerations, we conclude that assuming the average velocity of Fe x ions to be equal to that of Mg x ions is justified and should not result in a systematic
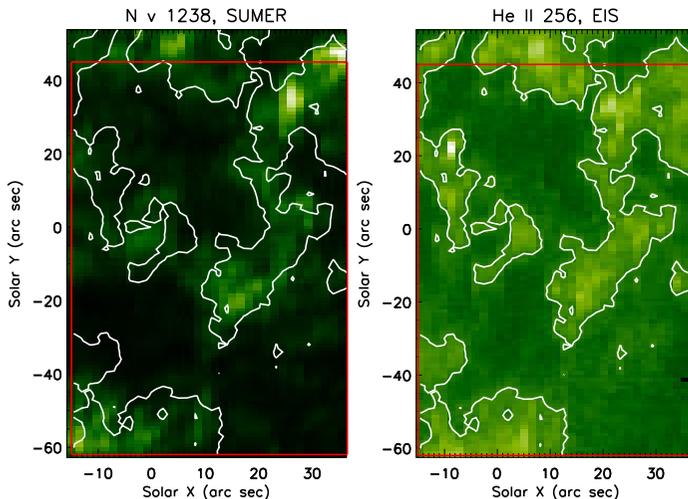
Figure 4.4: Radiance maps of the common area of study in N v λ1238 Å (SUMER, left) and He II λ256 Å (EIS, right). Contours of He II λ256 are plotted on both maps. The red boxes show the area in common to SUMER and the short and long wavelength ranges of EIS.

error that would be large enough to change our results and conclusions substantially. Therefore, in the following, we take Fe x λ184 as our reference line with respect to which the average Doppler shift of the remaining spectral lines recorded by EIS is determined.

4.4   A method of measuring the Doppler velocity of EIS coronal lines

Above the limb we assume that spectral lines have, on average, no Doppler shift (motions out of the plane of sky cancel out on average). This is verified by plotting histograms of velocity (with respect to the average) and histograms of the distance in wavelength between a line and the reference Fe x λ184 line. These histograms are very narrow, nearly Gaussian, and have an FWHM of 3 km s^{-1} to 4 km s^{-1} (Figs. 4.5, 4.6).

From the above assumptions[3] [4], the average of the off-limb line-distance histogram is

---

[3]To be precise, the quantity $\overline{\Delta\lambda_{\text{off}}}$ we measure from the histogram of the distance in (off-limb) wavelength should be corrected for the effect of solar rotation before being used at disk centre. This requires the right-hand side of Eq. 4.1 to be multiplied by $1 + v_{\text{rot}}/c$. In the case of the Sun, $v_{\text{rot}} \approx 2$ km s^{-1} and the term is practically equal to one.

[4]Also the gravitational red shift plays no role here. In fact, with EIS we are comparing distances between spectral lines on the disk and above the limb, and the effect, because the gravitational red shift is the same

then

$$\overline{\Delta\lambda_{\text{off}}} = \lambda_0 - \lambda_0^{\text{Ref}}, \tag{4.1}$$

where λ_0^{Ref} and λ_0 are the rest wavelengths of the reference line and of the line whose shift we want to measure.

On the disk we measure the quantity $\Delta\lambda = \lambda - \lambda^{\text{Ref}}$ at each pixel or group of pixels (where λ^{Ref} is the wavelength of the reference line). This can be written as

$$\Delta\lambda = \lambda_0 + \delta\lambda - \lambda_0^{\text{Ref}} - \delta\lambda^{\text{Ref}} = \overline{\Delta\lambda_{off}} + \delta\lambda - \delta\lambda^{\text{Ref}}, \tag{4.2}$$

where $\delta\lambda$ and $\delta\lambda^{\text{Ref}}$ are the line Doppler shifts. Considering that $v = c\frac{\delta\lambda}{\lambda_0}$, we have

$$\Delta\lambda = \overline{\Delta\lambda_{\text{off}}} + \frac{v}{c}\lambda_0 - \frac{v^{\text{Ref}}}{c}\lambda_0^{\text{Ref}}. \tag{4.3}$$

If we call $\delta v = v - v^{\text{Ref}}$, the difference between the velocities measured in the two lines, then δv becomes

$$\delta v = \frac{c}{\lambda_0}\left(\Delta\lambda - \overline{\Delta\lambda_{\text{off}}}\left(1 + \frac{v^{\text{Ref}}}{c}\right)\right). \tag{4.4}$$

Considering now the average value of v^{Ref}, $\overline{v^{\text{Ref}}}$, we can write

$$\overline{\delta v} = \frac{c}{\lambda_0}\left(\overline{\Delta\lambda} - \overline{\Delta\lambda_{\text{off}}}\left(1 + \frac{\overline{v^{\text{Ref}}}}{c}\right)\right). \tag{4.5}$$

We measure $\overline{\Delta\lambda}$ by taking the average of the distribution of wavelength differences between the two lines . Then, using equation (4.5) we calculate the relative velocity $\overline{\delta v}$ of hot coronal ions with respect to Fe x $\lambda184$ that we assume to have an average Doppler velocity $\overline{v^{\text{Ref}}}$ equal to the average Doppler velocity of Mg x $\lambda625$ (-1.8 ± 0.6 km s^{-1}).

Because of thermal variation along the 98.5 min Hinode orbit, there is a shift in the spectral line positions with time that needs to be corrected before using EIS data. Routines for correcting this variation are provided with the data reduction package and the correction has been applied to our data. However, we are not sure that the above correction (based on the data itself) is reliable down to the accuracy needed for the measurements discussed here (≈ 2 km s^{-1}). A major advantage of the technique presented in this paper is that we do not rely on this correction because we are just measuring the spectral distances between spectral lines [5]. We only need to make sure that all spectral lines move across the detectors in the same way, i.e., that there are no changes in the image scale with time. The top panel of Fig. 4.7 shows the dependence on time (and solar X) of line positions (averages along the slit, in wavelength units) for three lines (Fe x $\lambda184$, Fe x $\lambda257$, and Fe xii $\lambda193$) when no correction for temporal drifts is introduced. Offsets in wavelength (indicated in the figure) have been subtracted to make the comparison more evident. The behaviour of all the lines is very similar. The bottom panel of the figure

---

at the two places, cancels out. In the case of the SUMER data, the Doppler shift are measured with respect to the chromosphere, which is assumed to be at rest.

[5]This method also ensures that there is no bias from the observed line intensities in the derived average velocity.
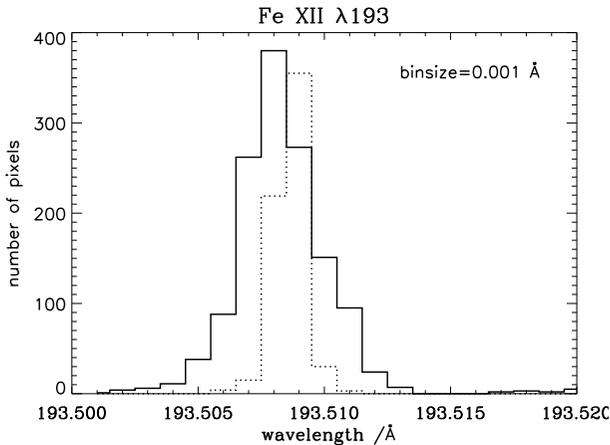
Figure 4.5: The histograms of line position in wavelength for Fe XII λ193 line off-limb (dotted line) and at disk centre (solid line). The off-limb histogram is narrower than the on-disk one because **net mass** motions are essentially absent.

shows line distances (differences in the values in the top panel) versus time and solar X. It can be seen that changes in line distance (wavelength differences) are very small ($\approx$1 mÅ, ≈ 1.5 km s^{-1}) and show no significant dependence with time. Hence our assumption is fulfilled.

To improve the signal-to-noise ratio, before fitting the line profiles we have binned the EIS on-disk spectra over three raster positions and over three pixels along the slit (3×5 binning for the Fe XV λ284, weak on the quiet Sun). A 2×2 binning was used for the off-limb spectra.

4.5   Results

Using the technique discussed in Section 4.4 we have obtained the line of sight velocities from the Doppler shifts of many coronal lines formed at temperatures between 1 MK and 2 MK in the quiet Sun. These lines, their deduced relative (to Fe X λ184) Doppler shifts and the corresponding uncertainties are listed in Table 4.2. In this table, we report the values obtained in the four EIS raster scans together with the estimated errors. Errors are obtained by error propagation analysis of Eq. 4.5, where the error on $\overline{\Delta\lambda_{\text{off}}}$ is given by the width σ of the off-limb line-distance distribution. On the other hand, the on-disk line distance distribution is also broadened by the different Doppler speeds characterising the two lines at different locations. For this reason the error for $\overline{\Delta\lambda}$ is assumed to be equal to that of $\overline{\Delta\lambda_{\text{off}}}$, leading to the same error for a given line in all the rasters. An independent estimate of these errors can be obtained by looking at the standard deviation of the measured values of $\overline{\delta v}$ obtained in the four rasters. From Table 4.2, values of
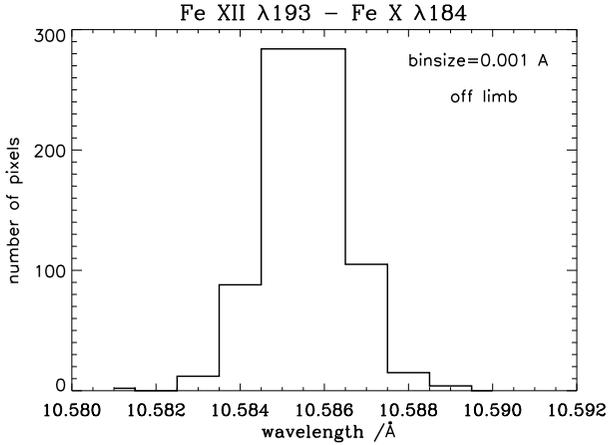
Figure 4.6: The histogram of distance in wavelength between Fe xıı λ195 line and the reference line (Fe x λ184) off-limb. The histogram is nearly Gaussian and with a sigma of ≈ 1.3 km s^{-1}, that can be taken as an estimate of the instrument accuracy in measuring the distance in wavelength.

0.1 km s^{-1} and 0.7 km s^{-1} would be obtained for Fe xıı λ195 and Fe xv λ284, respectively. These values are lower than our estimated errors and indicate the most likely we do not underestimate the errors provided in Table 4.2.

In the following, we take the average of rasters # 3 and # 4 as representative values of the average Doppler shift on the quiet Sun, the closest in time to the SUMER observations. By adding the value of average Doppler velocity of our reference line (Mg x λ625) to these values ($\overline{v} = \overline{v^{\text{Ref}}} + \overline{\delta v}$), the absolute Doppler velocity of lines are calculated (see Table 4.3). The error reported in this table, $\delta(\overline{v})$, is obtained by summing in quadrature the errors on relative line Doppler shifts (reported in Table 4.2), and the error in measuring the average Doppler velocity of our reference line (Mg x λ625). The values in Table 4.3) are plotted in Fig. 4.8 and as a blow-up for temperatures above 1 MK in Fig. 4.9.

Figure 4.8 displays the Doppler shift in the quiet Sun at disk centre of various TR and coronal ions in SUMER and EIS spectra. Positive values indicate red shifts (downflows), while negative values indicate blue shifts (upflows). Values obtained in this investigation (both SUMER and EIS) are marked by stars. In the figure the results of Teriaca et al. (1999a), Peter and Judge (1999), and the theoretical Doppler shifts of Hansteen et al. (2010) are also shown.

The solid and dashed lines respectively represent a by-eye fourth and sixth order polynomial representation of the combination of our present work for TR and coronal lines ($T \leq 2$ MK) and those of Teriaca et al. (1999a). Thus, the v *versus* log(T/[K]) behaviour can be parametrised by the coefficients that are listed in Table 4.4.

At temperatures higher than 1 MK our results show a modest but clear increase of the average blue shift with respect to the value measured around 1 MK (-1.8 km s^{-1}),
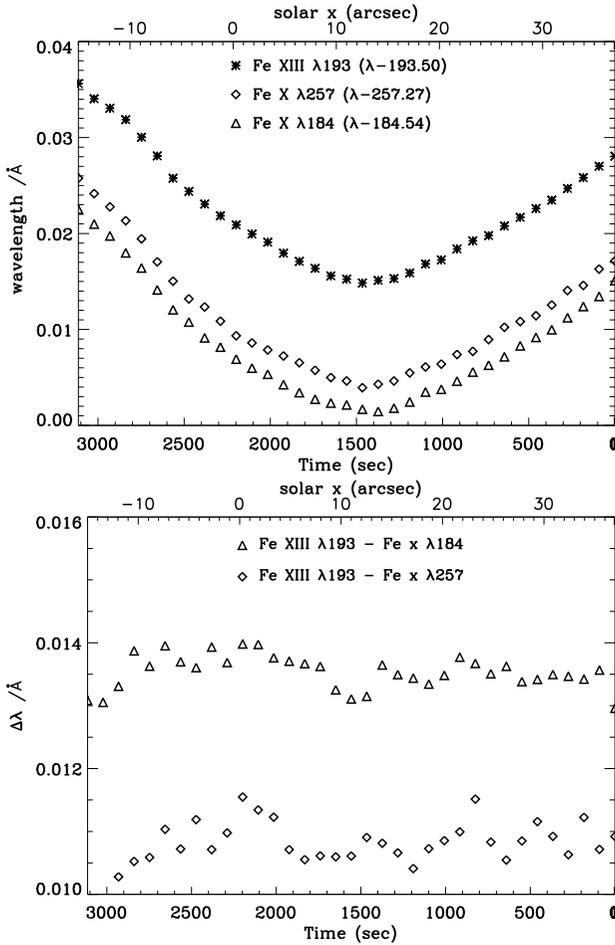
Figure 4.7: Upper panel: line positions, in wavelength units, of the Fe XII λ193, Fe X λ257, and Fe X λ184 lines versus time (and solar X) at disk centre. The wavelength values indicated in the panel have been subtracted to ease comparison. Lower panel: wavelength difference between spectral lines for the data in the upper panel versus time (and solar X). It can be seen that changes in line distances (wavelength differences) are very small ($\approx$1 m$\mathring{A}$, $\approx$ 1.5 km s^{-1}) and show no dependence on time.

Table 4.2: Doppler velocity of ions with respect to Fe x λ184.

line	$\overline{\delta v}$ [km s^{-1}]				$\delta(\overline{\delta v})$ [km s^{-1}]
	# 1	# 2	# 3	# 4	
Fe x 257.262	0.86	0.28	0.52	1.44	2.30
Fe xi 180.401	0.96	1.14	0.76	1.22	2.77
Fe xi 188.216	0.15	-0.71	-0.25	-0.68	1.88
Fe xi 188.299	-1.35	-2.35	-1.41	-1.57	2.14
Si x 258.375	-0.41	-0.87	-1.57	-1.10	2.04
Si x 261.058	-0.96	-0.04	-1.19	-0.73	2.29
Si x 271.990	-1.51	-1.62	-2.06	-2.17	2.07
S x 264.233	0.21	-0.01	-0.47	-0.47	2.09
Fe xii 193.509	-0.64	-0.83	-0.16	-0.46	1.98
Fe xii 195.119	-0.52	-0.67	-0.52	-0.67	1.52
Fe xii 256.925	-0.54	-1.00	-1.70	-0.65	2.76
Fe xiii 202.044	-0.43	-0.73	-0.14	-0.43	2.02
Fe xiii 251.953	-1.54	-3.08	-2.84	-1.42	2.96
Fe xiv 264.787	-2.62	-2.96	-2.27	-2.84	2.13
Fe xiv 274.203	-2.47	-2.14	-3.45	-1.59	2.13
Fe xv 284.160	1.38	0.33	1.28	-0.31	2.56

Columns 2 to 5 list the results for the four different rasters. The last column
last column provides the error, which is equal for all rasters (see text).

reaching a maximum of about -4.4 km s^{-1} at the Fe xiv formation temperature of 1.8 MK. At even higher temperatures, the average line shift appears to decrease again, reaching a value of (-1.3 ± 2.6) km s^{-1} obtained in Fe xv λ284 line at 2.1 MK.

To check if our results are dependent on the choice of our reference line (Fe x λ184), we have used another Fe x line (λ257) and calculated all Doppler velocities with respect to it. The Doppler velocities are found to agree within 1 km s^{-1} with those in Table 4.2.

It is clear that the absolute values of the velocities derived here depend on the value adopted for the reference line (in this case -1.8 km s^{-1}). To check the dependence of our results on the value of the velocity of our reference line (Fe x λ184, which we have supposed to have the same average Doppler velocity of Mg x λ625), we used Eq. 4.5 to calculate the absolute velocity for different values of the rest wavelength of the Mg x line (which ultimately determine the velocity in the reference line). The dependence of the Doppler shift on the Mg x rest wavelength and on the resulting Doppler velocity is shown in Fig. 4.10 for the Si x λ261, Fe xii λ195, Fe xiii λ251, Fe xiv λ264, and Fe xv λ284 lines. It should be noted that using the rest wavelength from Kelly (1987), would result in red shifts for most of the coronal lines studied here.

Table 4.3: Absolute average Doppler velocity of ions (averaged over rasters #3 and #4).

line ($\log(T/[\mathrm{K}])$)	$\bar{v}$ [km s^{-1}]	$\delta(\bar{v})$ [km s^{-1}] [a]
Fe x 184.536 (6.00)	-1.8 [b]	0.6 [b]
Fe x 257.262 (6.00)	-0.82	2.38
Fe xi 180.401 (6.04)	-0.81	2.83
Fe xi 188.216 (6.04)	-2.27	1.97
Fe xi 188.299 (6.04)	-3.29	2.22
Si x 258.375 (6.15)	-3.14	2.13
Si x 261.058 (6.15)	-2.76	2.37
Si x 271.990 (6.15)	-3.92	2.16
S x 264.233 (6.15)	-2.27	2.17
Fe xii 193.509 (6.15)	-2.11	2.07
Fe xii 195.119 (6.15)	-2.40	1.63
Fe xii 256.925 (6.15)	-2.98	2.82
Fe xiii 202.044 (6.20)	-2.09	2.11
Fe xiii 251.953 (6.20)	-3.93	3.02
Fe xiv 264.787 (6.26)	-4.36	2.21
Fe xiv 274.203 (6.26)	-4.32	2.21
Fe xv 284.160 (6.32)	-1.34	2.63

[a] The last column provides the error on the absolute average Doppler velocities (see text)

[b] Absolute velocity and error assumed equal to that of Mg x.

Table 4.4: Coefficients of the fourth and sixth order polynomial representations of the average Doppler velocity versus temperature behaviour of the quiet Sun.

coefficient	4th order	6th order
a_0	7874.8	-185202.25
a_1	-6427.5	223219.47
a_2	1943.26	-111257.36
a_3	-257.766	29345.005
a_4	12.6596	-4319.1993
a_5		336.35535
a_6		-10.827987

All decimals shown here are significant.
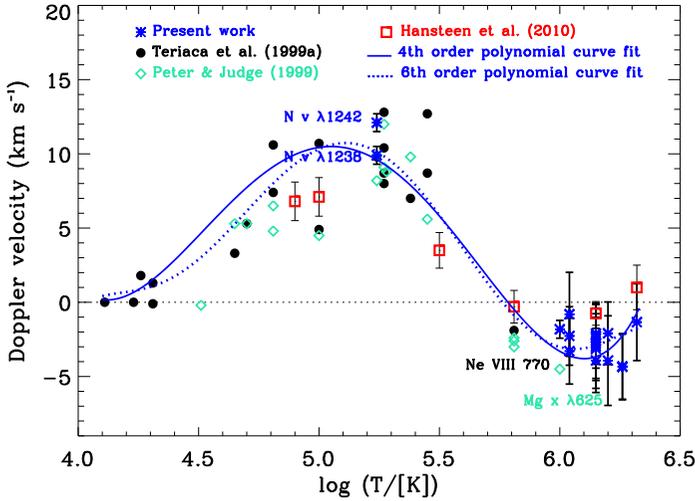
Figure 4.8: Average Doppler shift in the quiet Sun at disk centre of various TR and coronal ions measured from SUMER and EIS spectra. Positive values indicate red shifts (downflows) while negative values indicate blue shifts (upflows). Solid and dashed lines respectively represent fourth and and sixth order polynomial curves by-eye fitted to the combination of the measurements obtained in this work and those of Teriaca et al. (1999a).

4.6   Summary and conclusions

In the present study we measured the Doppler shift of TR and coronal lines on the quiet Sun (see Tables 4.1 & 4.3). We measured the absolute average velocity of Mg x λ625, N v λ1238, and N v λ1242 lines using SUMER data obtaining a blue shifted Doppler velocity of (-1.8 ± 0.6) km s^{-1} for Mg x λ625 and red shifts (downward motions) of (9.9 ± 0.6) and (12.1 ± 0.6) for the N v λ1238 and λ1242 lines. Our results for TR lines agree with previous studies done with SUMER (Brekke et al. 1997, Chae et al. 1998, Peter and Judge 1999, Teriaca et al. 1999a). Our result for the Mg x line is also consistent with the literature, once the differences on the adopted rest wavelength are accounted for (see Section 2.1). Of course, our value for the average shift in the Mg x line depends on the adopted rest wavelength of 624.967 Å (Dammasch et al. 1999a, Peter and Judge 1999, average between the values of). Since the velocities obtained from the EIS lines also depend on the absolute velocity of the Mg x ions, the precise determination of the rest wavelength of Mg x is paramount. The accurate, independent, and highly consistent measurements of Dammasch et al. (1999a) and Peter and Judge (1999) are the best available so far. In any case, Fig. 4.10 allows assessing the effect of a different rest wavelength for the Mg x λ625 line on the resulting Doppler shifts.

By using cospatial and nearly cotemporal SUMER & EIS data we, for the first time, measured the average Doppler shift of several coronal lines with formation temperatures above 1 MK in the quiet Sun near disk centre. We obtained negative Doppler shifts
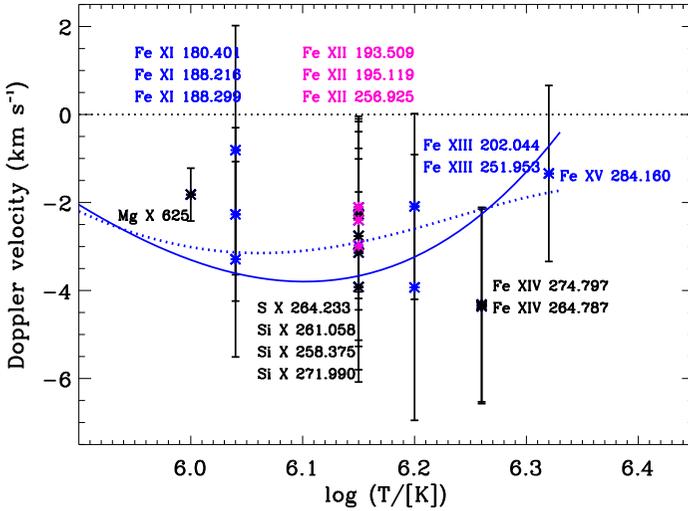
Figure 4.9: Magnification of the high-temperature part of Fig. 4.8 showing the results obtained in this work for coronal lines. Symbols and lines as in Fig. 4.8.

(upward motions) between -2 to -4 km s^{-1} at temperatures between 1 and 1.8 MK. At the highest temperature we can investigate, T = 2.1 MK (Fe xv λ284), we find indications of a reduction of the observed blue shift down to -1.3 km s^{-1}, a value that is compatible with no line shift, but also with a blue shift of up to -4 km s^{-1}.

As discussed in the Introduction, 1-D models assuming energy release in magnetic loops had successfully managed to reproduce the observer red shift at TR temperatures and blue shifts at coronal temperatures (e.g., Teriaca et al. 1999b, Spadaro et al. 2006). However, these models do not explicitly consider the heating mechanism.

More recently, comprehensive 3-D models of the solar atmosphere have been developed. Models assuming that coronal heating is caused by Joule dissipation of currents produced by stressing and braiding of the magnetic field produce red shifts at all temperatures (Peter et al. 2004, 2006), which is contrary to the present results and those of (Peter and Judge 1999) and (Teriaca et al. 1999a).

The addition to the model of episodic injections of emerging magnetic flux that reconnects with the existing field, produces rapid, episodic heating of the upper chromospheric plasma to coronal temperatures (Hansteen et al. 2010). Doppler shifts are computed by these authors for a model with an unsigned magnetic field of $|B_z| \approx 75$ G, which is compatible with the quiet Sun (Trujillo Bueno et al. 2004, Domínguez Cerdeña et al. 2006, Danilovic et al. 2010). The resulting Doppler shifts are roughly consistent with those reported here at all temperatures up to the Fe xiv formation temperature ($\log(T/[K])=6.26$) (see Fig. 4.8). Above this value, the line shifts predicted by the model return to zero and become slightly red shifted at the Fe xv formation temperature ($\log(T/[K])=6.32$).

Our Fe xv observations, instead, yield a blue shifted value. However, the error bar is
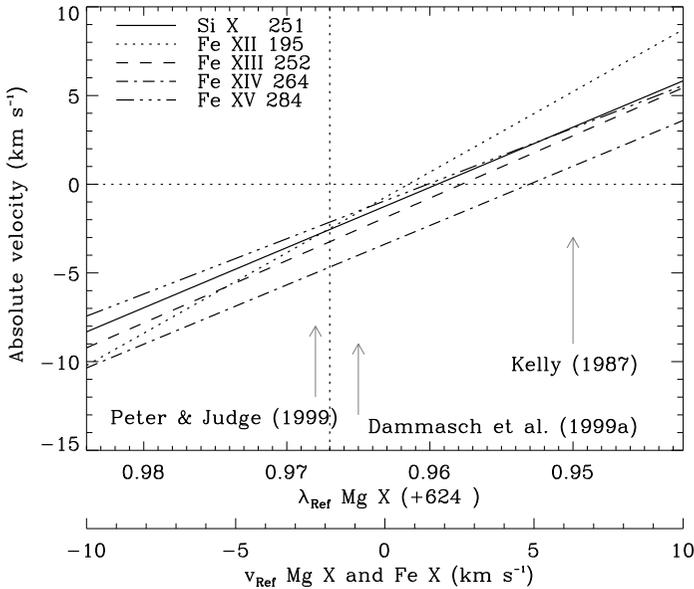
Figure 4.10: Variation in the absolute Doppler velocity of hot coronal ions as a function of the rest wavelength of the Mg x line and, consequently, of the Doppler velocity from the Fe x λ184 reference line. The vertical dotted line corresponds to the adopted rest wavelength of 624.967 Å.

large enough that no firm conclusion can be drawn. A real discrepancy at this temperature between the observations and the model may possibly be due to boundary effects in the adopted computing box or, more simply, to the fact that the turning point to zero or red shifted values occurs in reality at temperatures even higher than those measurable in this study. However, it may also be possible that important ingredients are still missing in the theoretical/numerical description.

Hansteen et al. (2010) suggest that the high speed flows generated by the localised heating events may be related to the high speed upflows that have been deduced from significant blueward asymmetries in Hinode/EIS observations of many TR and coronal lines (Hara et al. 2008b, De Pontieu et al. 2009, McIntosh and De Pontieu 2009a,b) that have been linked to spicules (De Pontieu et al. 2011). Thus, a more accurate introduction of the effect of spicules into the model may be necessary.

The model also foresees a smaller amount of Doppler shifts at both TR (lower red shifts) and coronal temperatures (lower blue shifts). However, this is not surprising (as the model does not specifically attempt to reproduce the solar region studied here), and the model is most likely compatible with our measurement. Since the model does not consider open field lines, this would indicate that the observed line shifts are simply a by-product of the heating of, and related mass supply to, closed loops. This would be

consistent with the finding that the plasma outflows seen on the quiet Sun, such as the Ne VIII blue shift, are largely associated with closed loops (Tian et al. 2008).

However, it cannot also be excluded that hot open funnels significantly contribute to the blue shifted emission observed between 1 and 2 MK. Only a detailed analysis of spatially resolved flows compared to field extrapolations (similar to what was done for the Ne VIII line at lower temperatures by Tian et al. 2008) would shed some light on the question. Given that these hotter lines are weak on the quiet Sun, this analysis is very difficult and will require a VUV spectrometer with much higher throughput than currently available, such as the spectrometer proposed for the Japanese Solar C mission (Teriaca et al. 2011).

5 Doppler shift of hot coronal lines in a moss area of an active region[1]

5.1 Abstract

The moss is the area at the footpoint of the hot (3 to 5 MK) loops forming the core of the active region where emission is believed to result from the heat flux conducted down to the transition region from the hot loops. Studying the variation of Doppler shift as a function of line formation temperatures over the moss area can give clues on the heating mechanism in the hot loops in the core of the active regions. We investigate the absolute Doppler shift of lines formed at temperatures between 1 MK and 2 MK in a moss area within active region NOAA 11243 using a novel technique that allows determining the absolute Doppler shift of EUV lines by combining observations from the SUMER and EIS spectrometers. The inner (brighter and denser) part of the moss area shows roughly constant blue shift (upward motions) of 5 km s^{-1} in the temperature range of 1 MK to 1.6 MK. For hotter lines the blue shift decreases and reaches 1 km s^{-1} for Fe xv 284 Å ($\sim$ 2 MK). The measurements are discussed in relation to models of the heating of hot loops. The results for the hot coronal lines seem to support the quasi-steady heating models for non-symmetric hot loops in the core of active regions.

5.2 Introduction

Active regions dominate the solar emission at EUV and X-ray wavelengths whenever they are present on the solar surface. Moreover they are the sources of most of the solar energetic phenomena. As such, active regions are a privileged target for studies of the solar activity of magnetic origin. Thus, studying the motions and flows over active regions have the potential of setting observational constraints on models of coronal heating and provide some clues to solve this problem (Doschek et al. 2007, Hara et al. 2008a, Del Zanna 2008, Brooks and Warren 2009, Warren et al. 2010).

Recent Observations from Hinode (Culhane et al. 2007) show two different types of active region loops: warm loops ($\sim$1 MK, Ugarte-Urra et al. 2009) and hot loops (> 2 MK, Brooks et al. 2008). There is evidence that the warm loops are multi-stranded structures impulsively heated by storms of nanoflares (Warren et al. 2003, Klimchuk 2006, Tripathi et al. 2009, Ugarte-Urra et al. 2009, Klimchuk 2009).

---

[1]This chapter is published as Dadashi et al. 2012.

However, in the case of hot coronal loops, there is observational support for both steady heating (Antiochos et al. 2003, Warren et al. 2008, Winebarger et al. 2008, Brooks and Warren 2009, Warren et al. 2010, Winebarger et al. 2011) and impulsive heating (Tripathi et al. 2010b, Bradshaw and Klimchuk 2011, Tripathi et al. 2011, Viall et al. 2012). Because of the unresolved nature of hot coronal loops (Tripathi et al. 2009) it is not possible to isolate a single loop and study its characteristics. One of the alternatives is to study the footpoints of the hot coronal loops, in the so-called "moss" areas. The moss is a bright reticulated feature observed in the EUV and was first described by Berger et al. (1999). They concluded that the moss is emission due to heating of low-lying plasma by thermal conduction from overlying hot loops. Thus, studying the spatial and temporal characteristics of observables such as brightness (Antiochos et al. 2003), Doppler shifts (Doschek et al. 2008, Del Zanna 2008, Brooks and Warren 2009, Tripathi et al. 2012, Winebarger et al. submitted, 2012), line widths (Doschek et al. 2008, Brooks and Warren 2009), electron densities (Fletcher and de Pontieu 1999, Tripathi et al. 2008, 2010a, Winebarger et al. 2011) and temperature structure (Tripathi et al. 2010a) in the moss could provide an important constraint on the heating mechanism operating in the hot core loops.

Measuring Doppler shift in the moss region is a powerful diagnostic tool to distinguish between steady heating and impulsive heating models (Brooks and Warren 2009, Del Zanna 2008, Tripathi et al. 2012). Since the detected Doppler shifts in the above mentioned studies were in general not significantly larger than the associated uncertainties the exact behaviour of the flows at temperatures above 1 MK is still debated and needs to be studied with higher accuracy.

Antiochos et al. (2003) found that the intensity inside the moss region varies very weakly (only 10%) over periods of hours. They also found that the magnetic field inside the moss regions changes very slowly. This was the first indication that the heating in the moss region is not due to discrete impulsive flare-like events, but to either steady heating or to low energy, high-frequency events that approximate a quasi-steady process. Heating in symmetric loops foresees no motion and therefore no Doppler shifts because the loops are supposed to be in static equilibrium. Any kind of asymmetry (like pressure difference between the two photospheric footpoints of the loops or in the heating and/or cross section of the loops), can generate steady flows (Noci 1981, Boris and Mariska 1982, Mariska and Boris 1983). Flows produced in this manner by Boris and Mariska (1982) have small velocities of few hundred m s^{-1} unless the asymmetries are extreme (Orlando et al. 1995, Winebarger et al. 2002, Patsourakos et al. 2004). The most common flows produced by these asymmetries are uni-directional (like siphon flow, Noci 1981, Craig and McClymont 1986). This means one of the loop legs should show blue shift and the other red shift. In the case of pressure difference between footpoints, overpressure at one footpoint of the loop drives an upflow moving along the entire loop and drains at the opposite footpoint. The flow accelerates with height due to density decrease in accordance with the continuity equation[2] (Aschwanden 2004).

Heating at both footpoints of the loops can also produce flows if it is significantly concentrated toward the footpoints (Klimchuk et al. 2010, and references therein). The source of the heating could be either truly steady or the frequency of the impulsive heating

---

[2] $\frac{1}{A}\frac{\partial}{\partial s}(nvA) = 0$, where n, v, A, and s are density, velocity, cross section, and length coordinate along the 1-D loop, respectively.

could be sufficiently high that a steady approximation would be valid. The flows are driven because of thermal non-equilibrium. Since the loop has localized heating at both sides, evaporative upflows (blue shifts) should occur from both ends of the loop.

Impulsive heating models consider the active region loops to be composed of many hundreds of small elemental unresolved strands that are randomly heated by storms of nanoflares (Cargill 1994). Some of the strands could show blue shifts (upflows) due to chromospheric evaporation and some of the strands could show red shifts (downflows) due to cooling and condensation of the evaporated plasma. Simulations done by Patsourakos and Klimchuk (2006) have revealed that upflows are faster, fainter and have a shorter lifetime than downflows. The computed line profiles from these strands are found to have a red shifted core with an enhanced blue wing. The red shifts are predicted to decrease with increasing temperature with sufficiently hot lines being blue shifted (Bradshaw & Klimchuk, priv. communication).

Brooks and Warren (2009) measured the Doppler shift, non-thermal width and temporal variation of the Fe xii 195 Å line over a moss region. They obtained a small red shift of about 2 to 3 km s^{-1} with almost no change in Doppler shift and non-thermal velocity with time. They concluded that their result verifies quasi-steady heating models. The value they used as a reference for measuring the Doppler shift, was obtained by averaging over the whole raster. However, this is not an accurate way to measure small velocities because if the emission outside of the moss has a non-zero absolute Doppler shift, which is rather likely, their reported result for the moss Doppler shift could change considerably.

Tripathi et al. (2012), using a more reliable wavelength calibration method developed by Young et al. (2012), studied the Doppler shifts in the temperature range of 0.7 - 1.6 MK. They obtained blue shifts below 2 km s^{-1} for both their coolest (Fe ix 197 Å) and hottest (Fe xiii 202 Å) lines, with an estimated accuracy of 4 to 5 km s^{-1}. They conclude that their result is in agreement with predictions of both steady and impulsive heating scenarios. Since the uncertainties in their work are quite larger than their measured velocities, to reveal the real direction of the motions in the moss area, a more accurate Doppler shift measurements with smaller uncertainties is needed.

In the present paper, we have concentrated on studying bulk flows by measuring Doppler shifts in the moss region using a high precision method which is based on simultaneous observations from the Extreme ultraviolet Imaging Spectrometer (EIS, Culhane et al. 2007) aboard Hinode and the Solar Ultraviolet Measurement of Emitted Radiation (SUMER, Wilhelm et al. 1995) spectrometer aboard the Solar and Heliospheric Observatory (SoHO). The implication of these results on the heating of hot loops rooted in moss areas is discussed.

5.3   Data analysis

Coordinated SUMER and EIS data (HOP193) were taken on 4th July 2011, between 15:50 to 18:53 UTC over NOAA active region 11243 near disk center. A full disk image by the Atmospheric Imaging Assembly (AIA, Lemen et al. 2012) aboard the Solar Dynamics Observatory (SDO) around the time of our observation is shown in Figure 5.1.
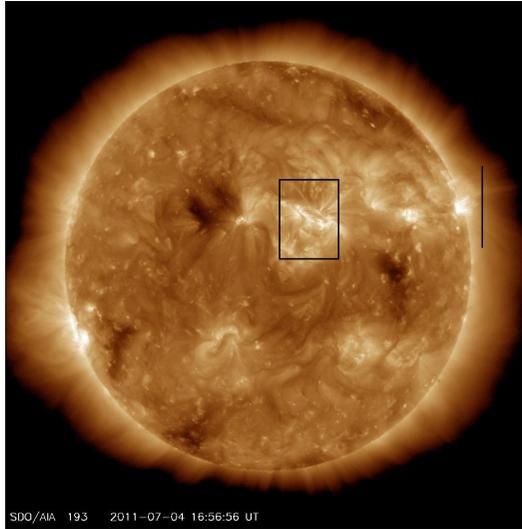
Figure 5.1: Fe XII 193 Å AIA image. The area observed on the disk by EIS is outlined by the black box. The black perpendicular line on the right side of the image represents the EIS slit position off-limb. Only the bottom quarter of the off-limb slit is used for data analysis. The area scanned by SUMER is shown in a closer view in Figure 5.4.

5.3.1   SUMER data: Doppler shift of Mg x

Since 1995 the normal incidence spectrograph, SUMER, operates between 450 Å to 1610 Åwavelength range. This powerful UV instrument is designed to investigate the bulk motions of plasma in the chromosphere, transition region, and low corona. The spatial resolution of SUMER across and along the slit is 1 arcsec and 2 arcsec, respectively. The spectral scale ($\approx$ 43 mÅ/pix at 1240 Å in the first order of diffraction, Wilhelm et al. 1997, Lemaire et al. 1997) is accurate enough[3] to measure the Doppler shift of lines down to 1 km s^{-1}. Corrections for wavelength-reversion, dead-time, flat-field, and detector electronicdistortion are applied to SUMER raw spectral images.

We use SUMER to measure the absolute Doppler shift of one coronal line (Mg x 625 Å) observed in the second order of diffraction around 1250 Å. SUMER does not have an on-board calibration source, hence we obtain the wavelength scale by using a set of chromospheric lines from neutrals and singly ionized atoms (for instance, C I lines with formation temperatures of 10000 K.). These lines are known to have negligible or small average Doppler shifts (Hassler et al. 1991, Samain 1991). The wavelength calibration

---

[3]in case of high signal to noise ratios
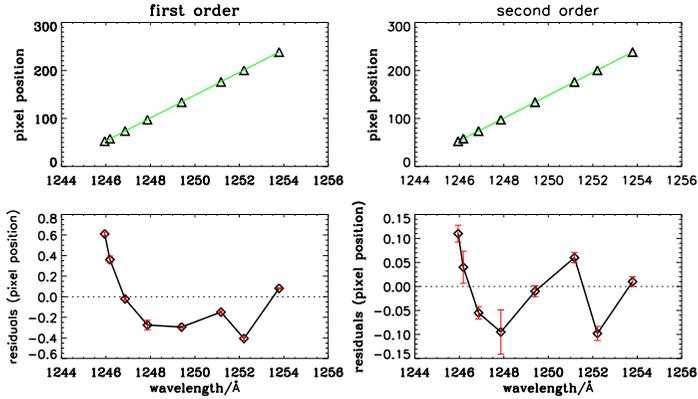
Figure 5.2: Left column: top panel shows the first order polynomial fit to pixel positions versus rest wavelengths of 8 suitable reference lines around the Mg x 625 Å line. Lower panel represents the residuals of the fitting. The residuals are large, up to 0.6 pixels ($\sim$ 6 km s^{-1}). Right column: top and lower panels represent a second order polynomial fit to pixel positions versus rest wavelengths and the residuals of the fitting, respectively. The residuals lie within $\pm$ 0.1 pixels (about 1 km s^{-1}).

has three main steps: identifying the lines by using a preliminarily wavelength scale, fitting the Gaussian curves to the spectral lines to find the exact pixel position of the lines, performing a polynomial fit to obtain the dispersion relation.

The SUMER data that we have used here consist of a sit-and-stare[4] sequence near disk center over a moss area within active region NOAA 11243. The acquired spectra (1245 Å to 1255 Å containing the Mg x 625 Å line, log T/[K]=6.00) are obtained by exposing for 75 s through the 1×300 arcsec^2 slit. The sequence consists of 48 spectra and results in a small, 10 arcsec wide, drift scan by solar rotation. We have checked the data to be sure that there are no significant instrumental drifts in the position of the spectral lines (either along the slit or as a function of time across the raster). A high signal to noise spectrum is obtained by averaging over the region of interest. Then, by choosing eight suitable reference lines (from relatively strong and unblended lines of neutral or singly ionized atoms) we have performed the wavelength calibration. A linear fit of their positions in pixels versus their laboratory wavelengths results in residuals of less than $\pm$ 0.6 pixels (see left column of Figure 5.2). The residuals clearly show the need for a second-order polynomial fit that leaves residuals of $\pm$ 0.1 pixels (less than 2 km s^{-1}). This is demonstrated in right column of Figure 5.2. Dadashi et al. (2011) also used a second order polynomial fit to obtain the velocity of the same line over a quiet Sun area. We believe the need for the higher order fit comes from residual errors in the correction of the electronic distortion of the detector image.

To obtain the Doppler shift map of the Mg x 625 Å line, we have used 624.967 Å as rest wavelength. This is the average between the values of (624.965 $\pm$ 0.003) Å given by

---

[4]The slit stays fixed in space and let the Sun rotates beneath.
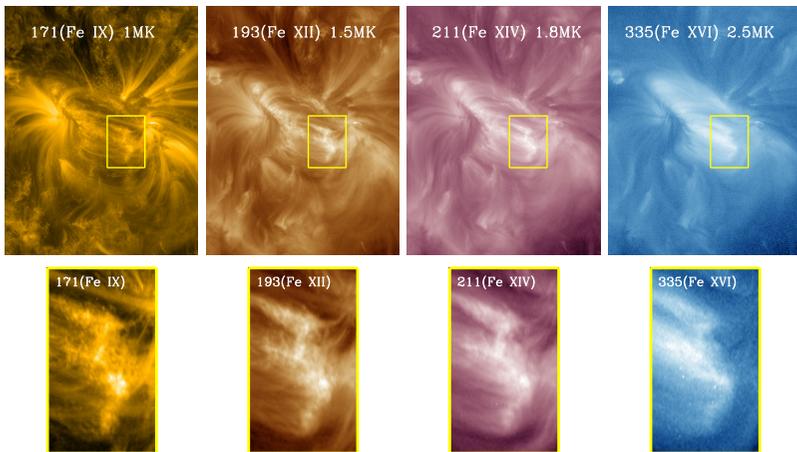
Figure 5.3: The NOAA active region 11243 is shown in different wavelength bands of AIA/SDO (top panels). The images are taken on 4th July 2011 at 17:00 UTC. The yellow boxes show the moss area studied in this work. Lower panels are blow ups of the corresponding yellow boxes.

Dammasch et al. (1999a) and (624.968 ± 0.007) Å given by Peter and Judge (1999). The reasons for this selection of the above rest wavelength are described in detail in Dadashi et al. (2011).

5.3.2   EIS data: analysis and co-alignment

The EIS instrument produces high-resolution stigmatic spectra in the wavelength ranges of 170 to 210 Å and 250 to 290 Å. The instrument has 1 arcsec spatial pixels and 0.0223 Å spectral pixels. More details are given in Culhane et al. (2007) and Korendyke et al. (2006).

EIS data consists of one raster scan (1 arcsec step size and 30 s exposure time) of the active region taken nearly simultaneously to the SUMER data, followed by one sit-and-stare sequence taken above the limb. Both observations were obtained using the 1 arcsec wide slit. The area of study (NOAA active region 11243) is shown in different wavelength bands of AIA/SDO in Figure 5.3. The over-plotted yellow box on each panel of this Figure shows the moss area that we had studied here. The eis_prep.pro routine, which is the standard EIS data reduction routine available in the SolarSoft (SSW) package, is used. This routine subtracts the dark current, removes the cosmic rays and hot pixels, and does radiometric calibration. The slit tilt and orbital variation effects are removed from the data by using the SSW eis_wave_corr.pro routine. The orbital variation caused by the thermal effects on the instrument does not play an important role in our study, since the technique we employ is based on the measurement of the line separations (the distance between the line of which we want to measure the shift and a reference line), a quantity
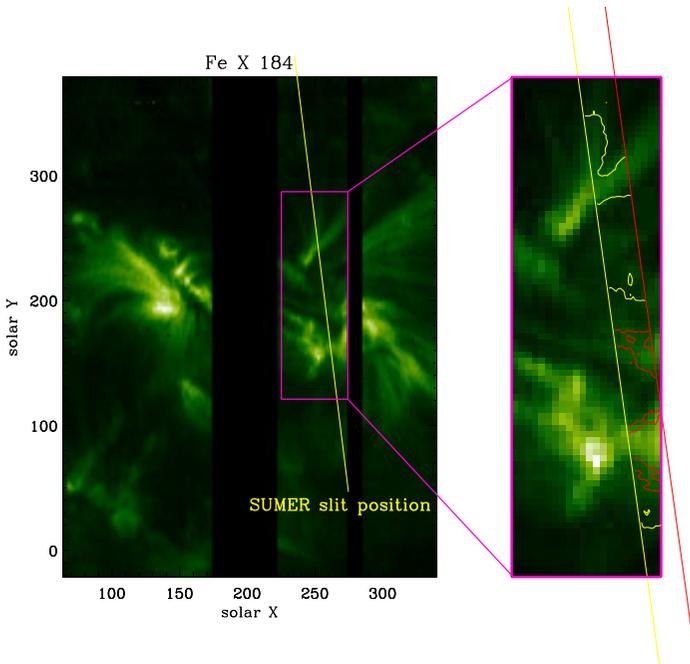
Figure 5.4: Left panel: the position of the SUMER slit at the start of the drift scan over-plotted on the EIS Fe x 184 Å intensity image raster. The SUMER slit crosses the moss area that we have studied in this paper. Right panel: blow up of the pink box in the left panel. Intensity contours of Mg x 625 Å are plotted on top of the intensity map of the Fe x 184 Å line.

that does not change during the relatively short duration of our observations (for further details see Dadashi et al. 2011).

After removing the offset between the SW and LW detectors, we co-align the two instruments (SUMER and EIS) by using a pair of radiance maps obtained in lines formed at similar temperatures: Mg x 625 Å (SUMER) and Fe x 184 Å (EIS). The left panel of Figure 5.4 shows the position of the SUMER slit at the beginning of the drift scan over-plotted on the EIS Fe x 184 Å image raster. The SUMER slit crosses the moss area that we have studied in this paper. The right panel of Figure 5.4 is a blow-up of the pink box shown in the left panel. The area scanned by SUMER is placed between red and yellow inclined lines. Intensity contours of Mg x 625 Å plotted on top of the intensity map of Fe x 184 Å allow us to co-align the image with an accuracy of roughly 1 arcsec.

5.3.3   Method of measuring absolute Doppler shifts

Since there are no suitable cool chromospheric lines in the EIS wavelength range, it is not possible to use the same calibration technique as with SUMER.

One of the alternatives is to measure "relative" Doppler shifts of hot coronal lines by comparing to observations of quiet Sun areas that are present in the same raster scan containing the target active region. To obtain "absolute" Doppler shifts with this technique, Young et al. (2012) have used the average absolute velocities in the quiet Sun measured by Peter and Judge (1999) using SUMER spectra. However, there is some degree of uncertainty and arbitrariness in identifying what is quiet Sun near an active region, leading to a substantial uncertainty of the absolute velocity.

Dadashi et al. (2011) have introduced a novel technique to obtain "absolute" Doppler shifts of hot coronal lines using simultaneous observation of EIS and SUMER. The technique is based on two important assumptions:

- First, above the limb of quiet regions without obvious structures, the spectral lines have, on average, no Doppler shift because the motions out of the plane of sky cancel out on average.

- Second, Mg x 625 Å (SUMER) and Fe x 184 Å (EIS) lines, which have similar formation temperature, have the same average Doppler shift in the common area of study[5].

Following Dadashi et al. (2011), we consider the EIS Fe x 184 Å line as the reference line and obtain all other coronal line velocities respect to this line.

$$\overline{\delta v} = \frac{c}{\lambda_0} \left(\overline{\Delta \lambda} - \overline{\Delta \lambda_{\text{off}}} \left(1 + \frac{\overline{v^{\text{Ref}}}}{c} \right) \right). \tag{5.1}$$

Then, the absolute Doppler shifts are obtained as

$$\overline{v} = \overline{\delta v} + \overline{v^{\text{Ref}}}, \tag{5.2}$$

where $\overline{\delta v}$ and $\overline{v}$ are the relative (to Fe x) and absolute average Doppler shift of each line and $\overline{v^{\text{Ref}}}$ is the average Doppler shift of the Mg x line measured by SUMER (see Fig. 5.5), assumed to be equal to that of the reference line (Fe x). c and λ_0 are the speed of light in vacuum and the rest wavelength of the line of which we want to measure the shift. Since λ_0 is not used to calculate the shift of the spectral line due to the Doppler effect, it does not need to be known with high accuracy.

$\overline{\Delta \lambda}$ and $\overline{\Delta \lambda_{\text{off}}}$ are the average of the distribution of wavelength separation of the two lines (the line of which we want to measure the shift and the reference line) on disk and off-limb, respectively. In this work we use this technique to measure the absolute Doppler shift of hot coronal lines in the moss region of NOAA active region 11243. To have a higher signal-to-noise ratio, before fitting the line profiles, we have binned the on-disk spectra over two raster positions and over two pixels along the slit (2×2 binning). In the case of off-limb spectra we have used a binning of 3×20 (3 in solar X and 20 in solar Y direction).

[5]Reasons are described in Dadashi et al. (2011).
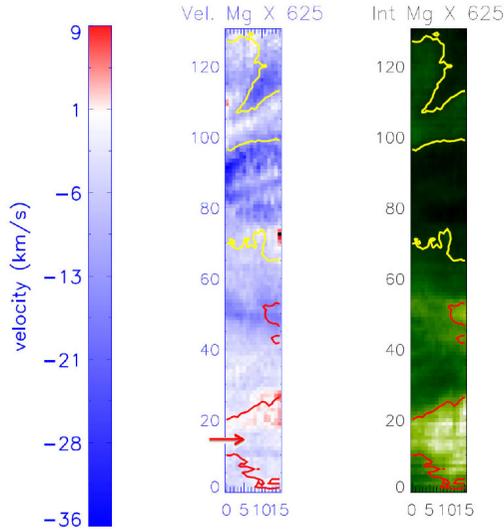
Figure 5.5: Intensity and velocity maps of Mg x 625 Å obtained by the sit-and-stared SUMER observations. Contours of Fe x 184 Å are plotted on both maps. The area that is marked by the red arrow corresponds to region **b** in the moss area (defined in the left panel of Figure 5.6). The average Doppler velocity of Mg x 625 Å is of -6.6 km s^{-1} inside region **b** and of (-5.50 ± 0.55) km s^{-1} over the whole area shown here.

This way, maps of relative Doppler shift were first obtained for Fe xi 188 Å, Fe xii 192 Å, Fe xiii 202 Å, Fe xiv 270 Å, and Fe xv 284 Å lines. The absolute Doppler shift map of Fe x 184 Å was obtained by imposing as rest wavelength a value that gives the same velocity pattern as Mg x 625 Å in the common observed area. After this, all relative Doppler maps were easily converted into absolute Doppler maps.

5.3.4   Moss identification

Figure 5.6 shows three different contours of the intensity of the Fe xii 192 Å line dividing the whole area of study into 4 different regions. We consider the middle intensity contour as a threshold to identify moss (regions **a** and **b** together, as marked in the left panel of Fig. 5.6).

The intensity ratio of Fe xii 192.39 Å and Fe xii 195.18 Å is density-sensitive. Using the CHIANTI atomic database (Landi et al. 2012), we have derived the intensity ratio of these two lines as a function of density (Fig. 5.7). Smaller intensity ratios correspond to higher densities. Right panel of Fig. 5.6 shows the map of the intensity ratio of the above Fe xii lines. Brighter intensity contours of Fe xii 192.39 Å line, which determine the moss
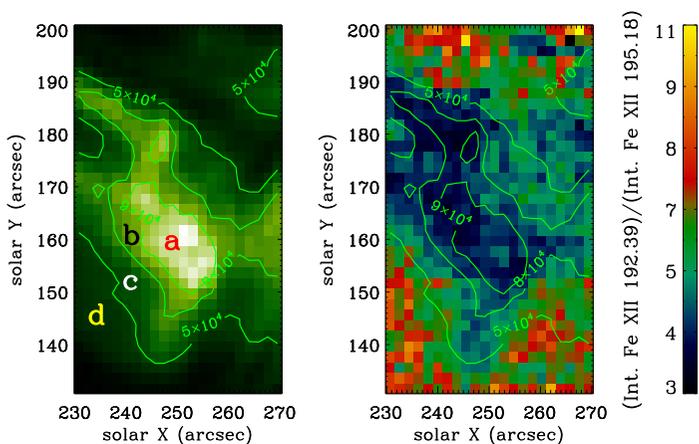
Figure 5.6: Left panel: Intensity map of Fe XII 192 Å. Right panel: The intensity ratio of Fe XII 192 Å and Fe XII 195.2 Å lines. Smaller ratios correspond to higher electron densities. The identified moss area (regions **a** and **b**) lie in the regions with higher density, as expected. Contours of intensity of the Fe XII 192 Å line are plotted on both maps.
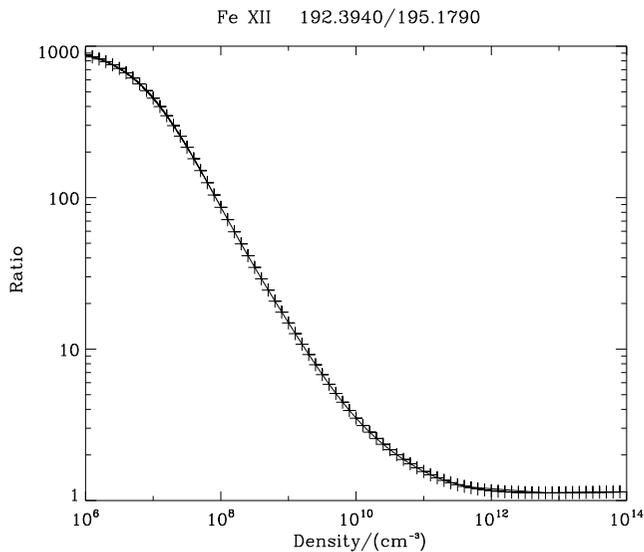

Figure 5.7: Intensity ratio of Fe XII 192 Å and Fe XII 195.18 Å lines as a function of density. Smaller intensity ratios correspond to higher densities.

Table 5.1: The Fe XII density average over the different regions defined in the left panel of Figure 5.6.

region	average density (cm^{-3})
a	7.27×10^9
b	6.31×10^9
c	4.84×10^9
d	3.39×10^9

region, are plotted on both maps. The identified moss region is characterized by higher density, as expected. The average electron density for regions **a**, **b**, **c**, and **d** are listed in Table 5.1. The average moss density (average of regions **a** and **b**) is about 6.6×10^9 cm^{-3}, which is a bit larger than 4.2 to 5.3×10^9 cm^{-3} reported by Fletcher and de Pontieu (1999). On the other hand, Tripathi et al. (2010a) obtained larger electron densities of about 10 to 30×10^9 cm^{-3} using the Fe XII 195.12 Å and 186.88 line ratio. However, we should consider that the densities obtained by Fe XII lines are overestimated in high density regions. The new Fe XII calculations by Del Zanna et al. (2012) show that there was some problem with the atomic data which has now been resolved.

5.4 Result and discussion

Using the technique introduced by Dadashi et al. (2011), and summarized in Section 5.3.3, we have obtained the line of sight Doppler shifts of hot coronal lines in a moss area of the active region NOAA 11243. In the first step of our study, we have defined the moss area by intensity contours of Fe XII 192 Å. Based on these contours, four different areas are defined in that region (left panel of Fig. 5.6). Table 5.2 lists the Doppler shift values for each of these regions with the corresponding uncertainties. Positive and negative values of velocity represent downflows (red shifts) and upflows (blue shifts), respectively.

The error reported in this Table $\delta(\overline{v})$ is obtained by error propagation analysis of Eqs. 5.1 and 5.2. The error on $\overline{\Delta\lambda_{0ff}}$ is given by the width σ of the off-limb line-separation distribution. Since the on-disk line separation distribution is also broadened by the different Doppler speeds characterizing the two lines at different temperatures, the error for $\overline{\Delta\lambda}$ is assumed to be equal to that off-limb. This leads to the same error for a given line in all different regions on disk.

Figure 5.8 shows the average Doppler shift for the four regions defined by intensity contours of the Fe XII 192 Å as a function of temperature. The Doppler shifts of the lines in the temperature range from 1 to 1.6 MK over regions **a**, **b**, and **c** show constant blue shifts or upward motions of about 5 km s^{-1}. For hotter lines the upward motions decrease down to about 1 km/s for Fe XV. Region **a**, which corresponds to the highest electron densities and intensities of the Fe XII 192 Å line, shows a somewhat smaller blue shift than the other regions for temperatures below 1.8 MK. Region **d**, that has the smallest intensity and density values, shows almost constant and stronger blue shift of about 8 km s^{-1}, in the temperature range from 1 to 2 MK.

For hotter lines (1.6 to 2 MK) there is almost no prevalent motion in regions **a**, **b**, and

Table 5.2: The average Doppler shift of hot coronal lines in the different regions defined in the left panel of Fig. 5.6. Positive and negative values of velocity represent downflows (red shifts) and upflows (blue shifts), respectively.

| line (log(T/[K]))	$\bar{v}$ [km s^{-1}]				$\delta(\bar{v})$ [km s^{-1}]
	# a	# b	# c	# d	
Fe XI 188.216 (6.04)	−2.83	−5.14	−5.51	−6.45	2.27
Fe XII 192.394 (6.15)	−3.70	−5.06	−5.50	−8.57	2.51
S X 264.233 (6.15)	−4.48	−5.39	−5.05	−7.31	2.06
Fe XIII 202.044 (6.20)	−3.78	−4.67	−3.93	−8.57	1.96
Fe XIV 270.519 (6.26)	−1.04	−1.82	−1.60	−6.81	2.15
Fe XV 284.160 (6.32)	−1.52	−0.36	−0.46	−7.75	2.08
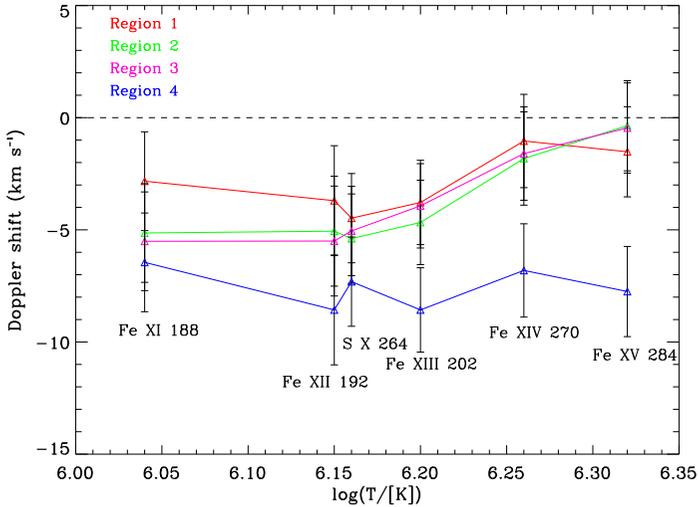
Figure 5.8: The average Doppler shift of hot coronal lines in different regions defined in the left panel of Fig. 5.7, plotted as a function of formation temperature. Fe XII and S X have nearly the same formation temperature, but are plotted a bit separated for better readability. Positive and negative values of velocity represent downflows (red shifts) and upflows (blue shifts), respectively.
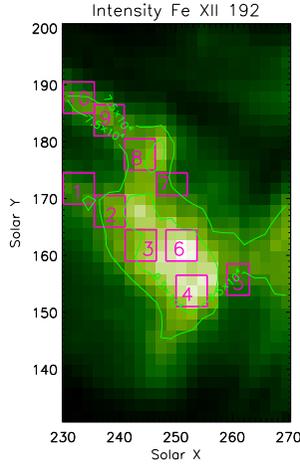
Figure 5.9: Ten different small square areas selected to study the Doppler velocities therein, overplotted on a map of Fe XII 192 Å intensity. Green contours are intensity contours of Fe XII 192 Å.
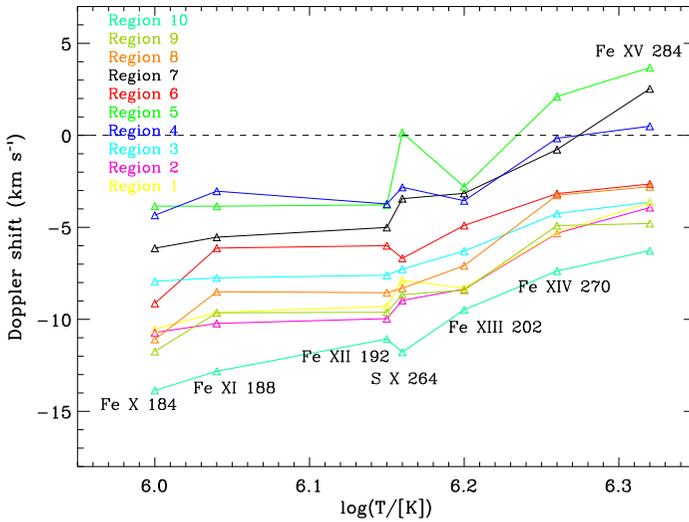
Figure 5.10: The Doppler shift as a function of temperature for the ten boxes defined in Fig. 5.9. Fe XII and S X have the same formation temperature but are plotted a bit separated for better readability.

105
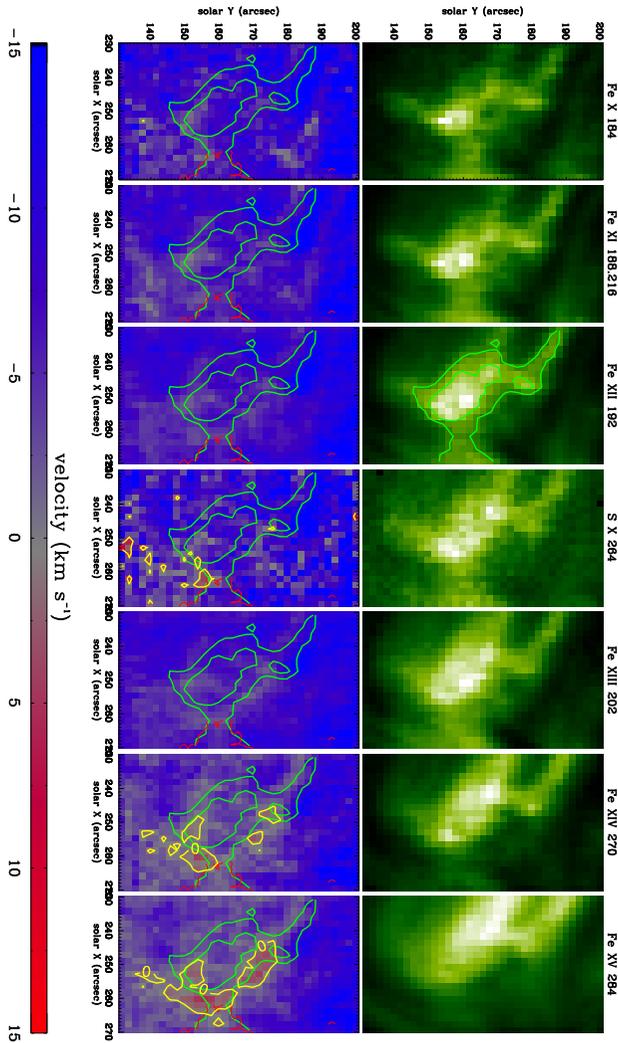
Figure 5.11: Intensity (upper panels) and velocity maps (lower panels) for Different ions with different formation temperatures. Green contours are intensity contours of Fe xii 192 Å plotted on top of intensity (top row) and velocity maps (bottom row) of different ions. Yellow contours on velocity maps outline red shifted pixels. Red contour is the brightest area which is common in both EIS and SUMER field of views and is used for velocity calibration.

c (0 to 2 km s^{-1}, with velocities never diverging by more than 2σ from zero). Region **d** at the same temperature shows strong blue shift.

To have a better understanding of the behaviour, we have selected ten small boxes at different locations of the area of interest (shown in Fig. 5.9) and calculated the average absolute Doppler shifts inside each box. Figure 5.10 displays the average absolute Doppler shifts of different ions as a function of their formation temperatures in the ten selected areas.

The same general behaviour of velocity is observed with respect to temperature in all regions. Doppler shifts are essentially constant up to temperatures of about 1.6 MK. Above this value, upward velocities decrease and almost stop at a temperature of about 2 MK except for the loop legs and the parts of the moss with lower electron densities (e.g. regions 1, 2, 3, 9, and 10). The inner (brighter and denser) part of the moss shows smaller upflows (regions 4 and 5). In contrast, regions 1, 2 and 8, 9, which are on the legs of the hot coronal loops (as suggested also by magnetic field extrapolations, see Fig. 5.12), show larger blue shift (upward motions) of about 10 km s^{-1} between 1 MK and 1.6 MK. This suggest that as the plasma rises higher along the loop leg, it accelerates. This conclusion is further illustrated by region 10, which lies further up in the loop leg and is associated with higher upflows of about 13 to 14 km s^{-1}). In all regions, colder lines sense stronger upflows (the colder, the more shifted to the blue).

Hotter lines like Fe XIV 270 Å and Fe XV 284 Å in the brighter and denser part of moss reveal no significant motions (the only exception is region 5 that shows a small red shift (downward motion) of about 3 km s^{-1} at this temperature). The intensity and corresponding Doppler shift maps of all these hot coronal lines are plotted in Fig. 5.11. The red shifted area of Fe XIV and Fe XV lies within the yellow contours overplotted on the corresponding velocity maps.

Our results for Fe XII are based on the unblended Fe XII line at 192 Å. However, we have also obtained the velocity from the Fe XII 195.120 line which is one of the brightest lines recorded by EIS. This line is blended by Fe XII 195.180 Å in its red wing. The density sensitive ratio, 195.180/195.120, increases with increasing density. Considering both components, performing a double Gaussian fit will result in redder velocities than the other unblended Fe XII lines[6] (Young et al. 2009). Here we find that considering a double Gaussian profile for Fe XII 195 Å on average results in a velocity redder than Fe XII 192 Å by about 2.2 km s^{-1} .

To have a more precise idea about the orientation of the hot coronal loops, we have extrapolated the photospheric field into the solar corona by using photospheric vector magnetograms obtained by the Helioseismic and Magnetic Imager (HMI, Schou et al. 2012) aboard Solar Dynamics Observatory (SDO). The nonlinear force-free coronal magnetic field extrapolation technique used here is described in detail by Wiegelmann et al. (2012). Figure 5.12 shows the magnetic field lines plotted over an AIA/SDO image taken at 17:00 UTC, which lies within the time frame of our study. The field of view for applying nonlinear coronal magnetic field extrapolation (the whole window of Fig. 5.12) is chosen in order to fulfill consistency criteria:

- The vector magnetogram should be almost perfectly flux balanced.

[6]http://msslxr.mssl.ucl.ac.uk:8080/eiswiki/Wiki.jsp?page=EisDiscussion
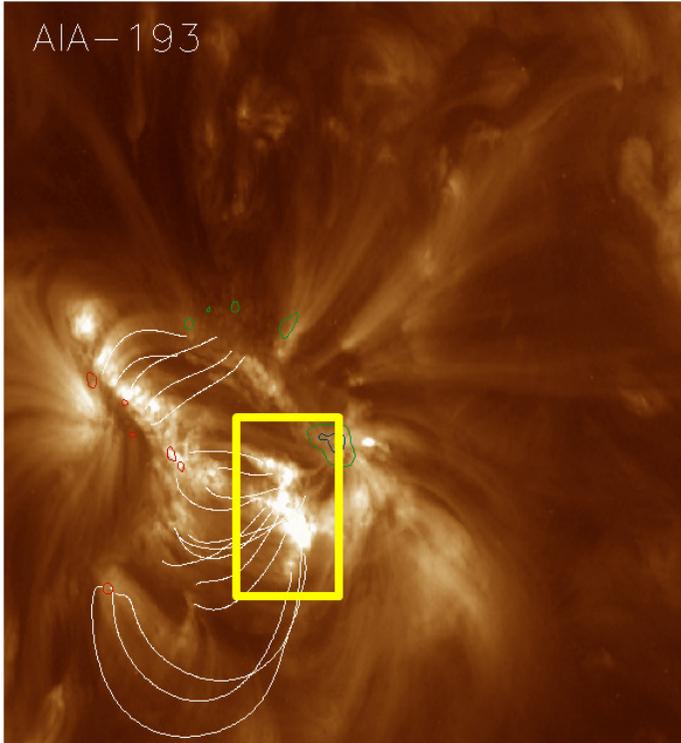
Figure 5.12: Magnetic field lines extrapolated from photospheric field and plotted over Fe xii 193 Å image of AIA/SDO. Red contours show positive and blue and green contours show negative polarities. The yellow frame represents the region of the moss study in this work.

- The field of view should be large enough to cover weak field surrounding of the target active region.
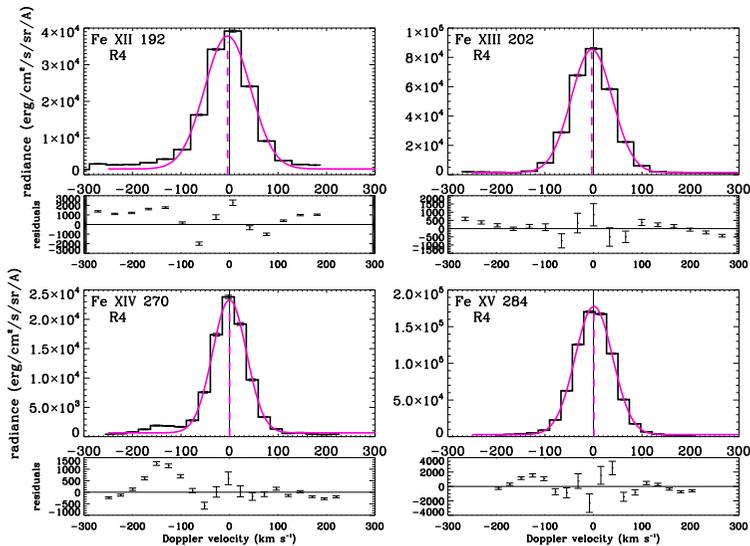
Figure 5.13: Spectral profiles of Fe XII, Fe XIII, Fe XIV, and Fe XV obtained over region 4 (defined in Fig. 5.9).

The field lines shown in Fig. 5.12 better reveal the prevailing direction of the hot loops than can be seen in the 211 and 335 AIA channels. Note that the loops emerging from the moss extend away from it in two directions. These are the short loops extending North-East from the upper part of the moss. These correspond to the loops well visible in Fe XIV and Fe XV, whose legs are sampled by boxes 1, 2, 8, 9, and 10 in Fig. 5.9. The results of the magnetic field extrapolation show another set of loops which is directed the South-East starting from the moss (more visible in cooler lines like Fe IX 171 Å). Thus, the Fe XIV and Fe XV red shifted regions visible in Fig. 5.11 (outlined by the yellow contours) appear located in the areas free of line-of-sight contamination from plasma higher up along the loop legs. Since the emission from the loop legs is clearly blue shifted, we may speculate that the near zero blue shifts observed over the moss may actually be a combination of red shift at the footpoint and blue shift along the loops. Both red and blue shifts are too small to leave a signature in the line profile sufficiently strong to disentangle the two velocity components in a single line profile at the EIS spectral resolution. However, the possibility that the red shifted region seen in Fe XV is due to an independent phenomenon, cannot be entirely excluded.

Impulsive heating models that consider a group of unresolved strands heated by periodic events like nanoflares, predict red shift (downward motion) on both legs of the loops in ~1 MK lines and more complex profiles with an extended blue wing in very hot lines such as Fe XVII (Klimchuk 2006, Patsourakos and Klimchuk 2006).

Our Doppler shift measurements inside the moss region do not show the predicted red shift of ~1 MK lines and the increasing blue shift of lines at increasingly higher
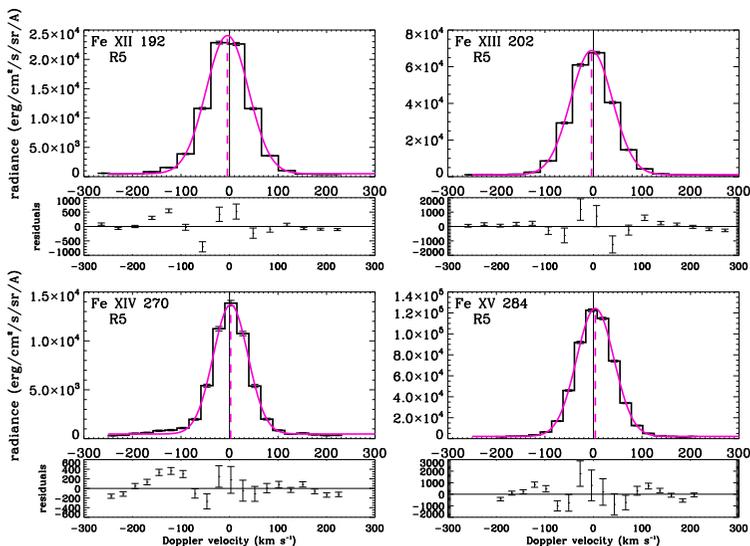
Figure 5.14: Spectral profiles of Fe xii, Fe xiii, Fe xiv, and Fe xv obtained over region 5 (defined in Fig. 5.9).

temperatures, but rather the opposite. We clearly see blue shifted emission in lines formed between 1 and 1.6 MK and almost zero velocity at the Fe xv formation temperature. Moreover, we have studied the line profiles associated with some of these ten regions to look for possible asymmetries. Figures 5.13 to 5.15 show the spectral line profiles for Fe xii 192 Å, Fe xiii 202 Å, Fe xiv 270 Å, and Fe xv 284 Å over the selected regions 4, 5, and 10, respectively. A single Gaussian fit is performed on all line profiles. Residuals of each fit are also plotted right under the panel with the line profile.

The spectral profiles seem to be well represented by a Gaussian and no specific asymmetry is detected (residuals are less than 2 to 3% of the amplitudes of the line profiles). Fe xiv 270 Å and Fe xv 284 Å line profiles seem to be weakly blended with Mg vi 270.394 Å and Al ix 284.015 Å in their blue wings (the small bumps in the residual plots). After taking out the effect of these blends, all line profiles are highly symmetric (see also Tripathi et al. in preparation). If profiles with extended blue wings are actually present at the footpoints of hot loops, they are only observable in lines much hotter that Fe xv.

Measurements of density and thermal properties of moss observed by EIS have shown no significant change over several hours (Tripathi et al. 2010a). This leads the authors to suggest that the heating of the hot coronal loops associated to the moss might be quasi-steady. Brooks and Warren (2009) have shown that the amount and variability of shifts and widths of coronal lines is small and appears consistent with steady heating models. However, we note that variability of density, flows and line widths were studied on a spatially averaged region and any small scale variations may get averaged out. Steady heating models of perfectly symmetric coronal loops predict no bulk motions since the conduc-
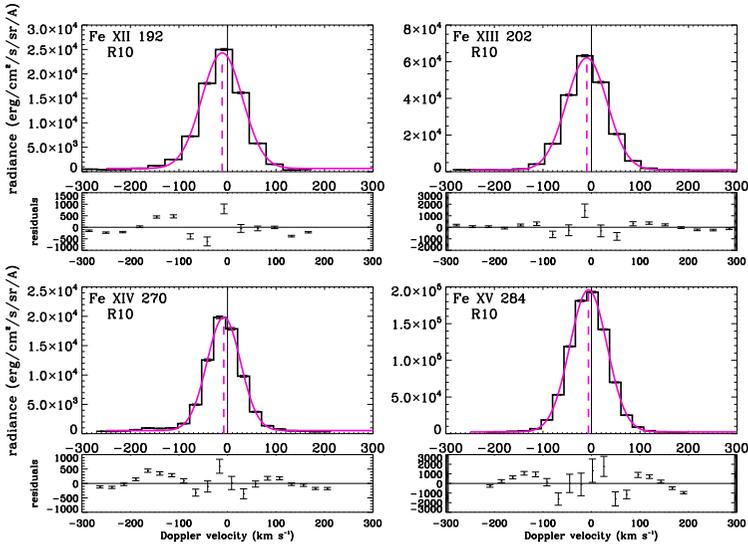
Figure 5.15: Spectral profiles of Fe xɪɪ, Fe xɪɪɪ, Fe xɪv, and Fe xv obtained over region 10 (defined in Fig. 5.9).

tive flux from the corona is balanced by radiative cooling (Mariska and Boris 1983, Klim-chuk et al. 2010). Impulsive heating, on the other hand, predicts definite plasma flows, which are temperature dependent. The relationship between velocity and temperature af-ter spatial averaging may not be straight forward, as different strands may be evolving completely independently and providing mixed observational signatures.

The near absence of Doppler shifts in the hotter lines (Fe xɪv and Fe xv) and, in general, the absence of red shifted emission in the observed moss region, along with the observed symmetric line profiles, seems to be consistent with quasi-steady heating of non-symmetric loops. Steady heating driven by pressure difference between the footpoints of the loops predicts the flows to be accelerated with height. For non-symmetric loops, this effect will produce siphon-like flows in which one footpoint will be red shifted and the other would be blue shifted. Unfortunately, we can not check and compare the flows at the other footpoint of these loops. In fact, due to the fact that the Hinode spacecraft suffered from seasonal eclipses at that time of the year, the other footpoint is missing in the EIS image raster (Figure 5.4).

In support of quasi-steady heating of hot loops, we have found the Doppler shift to increase as we go higher in the loop leg (Figures 5.9 and 5.10). However, observations of a larger sample of moss regions in lines covering higher temperatures than Fe xv would be necessary to consolidate our findings.

5.5   Summary

- By combining SUMER and EIS data, with a new technique developed by Dadashi et al. (2011), we have measured the absolute Doppler shift of hot coronal lines (Fe x 184 Å, Fe xi 188 Å, Fe xii 192 Å, Fe xiii 202 Å, Fe xiv 270 Å, and Fe xv 284 Å) in the moss of an active region.

- The moss is identified as the region where Fe xii 192 Å intensity corresponds to electron densities above about 6.6×10^9 cm^{-3}.

- The inner (brighter and denser) part of the moss area shows roughly a constant blue shift (upward motions) of 5 km s^{-1} in the temperature range of 1 MK to 1.6 MK. For hotter lines the blue shift decreases, down to 1 km s^{-1} for Fe xv 284 Å. Absolute Doppler shift maps are obtained using the Dadashi et al. (2011) technique. The general dependence of the velocity on temperature seems to be the same everywhere in the map. In all regions, the colder the line the stronger the blue shift.

- In general, the inner (brighter and denser) part of the moss shows smaller blue shifts, whereas the legs of hot coronal loops with footpoints in the moss, show larger blue shift.

- Our velocity measurements inside the moss region do not show the red shifts predicted by the impulsive loop heating model (Klimchuk 2006, Patsourakos and Klimchuk 2006). Also, we have found the line profiles to be highly symmetric, which is in contrast with the predictions of impulsive heating models.

- The near absence of motions seen in the hotter lines and, in general, the absence of red shifted emission in the observed moss region, as well as the observed symmetric line profiles, and higher velocities in higher parts of the loop legs seem to be consistent with quasi-steady heating models for non-symmetric loops.

Bibliography

Achour, H., Brekke, P., Kjeldseth-Moe, O., Maltby, P., 1995, Observed Redshifts in the Solar Transition Region above Active and Quiet Regions, The Astrophysical Journal, 453, 945–952

Antiochos, S. K., Karpen, J. T., DeLuca, E. E., Golub, L., Hamilton, P., 2003, Constraints on Active Region Coronal Heating, The Astrophysical Journal, 590, 547–553

Aschwanden, M. J., 2004, Physics of the Solar Corona. An Introduction, Praxis Publishing Ltd

Aschwanden, M. J., Poland, A. I., Rabin, D. M., 2001, The New Solar Corona, Annual Review of Astronomy and Astrophysics, 39, 175–210

Athay, R. G., 1981, Chromosphere-corona transition region models with magnetic field and fluid flow, The Astrophysical Journal, 249, 340–348

Athay, R. G., 1984, The origin of spicules and heating of the lower transition region, The Astrophysical Journal, 287, 412–417

Athay, R. G., Holzer, T. E., 1982, The role of spicules in heating the solar atmosphere, The Astrophysical Journal, 255, 743–752

Ayres, T. R., Jensen, E., Engvold, O., 1988, Redshifts of high-temperature emission lines in the far-ultraviolet spectra of late-type stars. II - New, precise measurements of dwarfs and giants, The Astrophysical Journal Supplement Series, 66, 51–68

Beckers, J. M., 1968, Solar Spicules (Invited Review Paper), Solar Physics, 3, 367–433

Berger, T. E., de Pontieu, B., Fletcher, L., Schrijver, C. J., Tarbell, T. D., Title, A. M., 1999, What is Moss?, Solar Physics, 190, 409–418

Boerner, P., Edwards, C., Lemen, J., Rausch, A., Schrijver, C., Shine, R., Shing, L., Stern, R., Tarbell, T., Title, A., Wolfson, C. J., Soufli, R., Spiller, E., Gullikson, E., McKenzie, D., Windt, D., Golub, L., Podgorski, W., Testa, P., Weber, M., 2012, Initial Calibration of the Atmospheric Imaging Assembly (AIA) on the Solar Dynamics Observatory (SDO), Solar Physics, 275, 41–66

Boris, J. P., Mariska, J. T., 1982, An explanation for the systematic flow of plasma in the solar transition region, The Astrophysical Journal, 258, L49–L52

Bradshaw, S. J., Klimchuk, J. A., 2011, What Dominates the Coronal Emission Spectrum During the Cycle of Impulsive Heating and Cooling?, The Astrophysical Journal Supplement Series, 194, 26

Brekke, P., 1993, Observed redshifts in O V and downflows in the solar transition region, The Astrophysical Journal, 408, 735–743

Brekke, P., 1999, Observations of Transition Region Plasma, Solar Physics, 190, 379–408

Brekke, P., Hassler, D. M., 1995, Needs for Improved Laboratory Wavelength Measurements in the EUV, in Laboratory and Astronomical High Resolution Spectra, (Eds.) A. J. Sauval, R. Blomme, N. Grevesse, vol. 81 of Astronomical Society of the Pacific Conference Series, p. 589

Brekke, P., Hassler, D. M., Wilhelm, K., 1997, Doppler Shifts in the Quiet-Sun Transition Region and Corona Observed with SUMER on SOHO, Solar Physics, 175, 349–374

Brooks, D. H., Warren, H. P., 2009, Flows and Motions in Moss in the Core of a Flaring Active Region: Evidence for Steady Heating, The Astrophysical Journal, 703, L10–L13

Brooks, D. H., Ugarte-Urra, I., Warren, H. P., 2008, The Role of Transient Brightenings in Heating the Solar Corona, The Astrophysical Journal Letter, 689, L77–L80

Brueckner, G. E., Bartoe, J.-D. F., 1983, Observations of high-energy jets in the corona above the quiet sun, the heating of the corona, and the acceleration of the solar wind, The Astrophysical Journal, 272, 329–348

Buchlin, E., Vial, J.-C., 2009, Electron density in the quiet solar coronal transition region from SoHO/SUMER measurements of S VI line radiance and opacity, Astronomy and Astrophysics, 503, 559–568

Cargill, P. J., 1994, Some implications of the nanoflare concept, The Astrophysical Journal, 422, 381–393

Chae, J., Yun, H. S., Poland, A. I., 1998, Temperature Dependence of Ultraviolet Line Average Doppler Shifts in the Quiet Sun, The Astrophysical Journal Supplement Series, 114, 151–164

Chae, J., Park, Y.-D., Moon, Y.-J., Wang, H., Yun, H. S., 2002, Temperatures of Extreme-Ultraviolet-emitting Plasma Structures Observed by the Transition Region and Coronal Explorer, The Astrophysical Journal Letter, 567, L159–L163

Cheimets, P., Caldwell, D. C., Chou, C., Gates, R., Lemen, J., Podgorski, W. A., Wolfson, C. J., Wuelser, J.-P., 2009, SDO-AIA telescope design, in Society of Photo-Optical Instrumentation Engineers (SPIE) Conference Series, vol. 7438 of Society of Photo-Optical Instrumentation Engineers (SPIE) Conference Series

Cheng, Q., 1992, Fluid motions in the solar atmosphere. III - A possible explanation of the downflows, Astronomy and Astrophysics, 262, 581–586

Cirtain, J. W., Golub, L., Winebarger, A. R., De Pontieu, B., Kobayashi, K., Moore, R. L., Walsh, R. W., Korreck, K. E., Weber, M., McCauley, P., Title, A., Kuzin, S., DeForest, C. E., 2013, Energy release in the solar corona from spatially resolved magnetic braids, Nature, 493, 501–503

Craig, I. J. D., McClymont, A. N., 1986, Quasi-steady mass flows in coronal loops, The Astrophysical Journal, 307, 367–380

Culhane, J. L., Harra, L. K., James, A. M., Al-Janabi, K., Bradley, L. J., Chaudry, R. A., Rees, K., Tandy, J. A., Thomas, P., Whillock, M. C. R., Winter, B., Doschek, G. A., Korendyke, C. M., Brown, C. M., Myers, S., Mariska, J., Seely, J., Lang, J., Kent, B. J., Shaughnessy, B. M., Young, P. R., Simnett, G. M., Castelli, C. M., Mahmoud, S., Mapson-Menard, H., Probyn, B. J., Thomas, R. J., Davila, J., Dere, K., Windt, D., Shea, J., Hagood, R., Moye, R., Hara, H., Watanabe, T., Matsuzaki, K., Kosugi, T., Hansteen, V., Wikstol, Ø., 2007, The EUV Imaging Spectrometer for Hinode, Solar Physics, 243, 19–61

Curdt, W., Brekke, P., Feldman, U., Wilhelm, K., Dwivedi, B. N., Schühle, U., Lemaire, P., 2001, The SUMER spectral atlas of solar-disk features, Astronomy and Astrophysics, 375, 591–613

Curdt, W., Landi, E., Feldman, U., 2004, The SUMER spectral atlas of solar coronal features, Astronomy and Astrophysics, 427, 1045–1054

Dadashi, N., Teriaca, L., Solanki, S. K., 2011, The quiet Sun average Doppler shift of coronal lines up to 2 MK, Astronomy and Astrophysics, 534, A90

Dadashi, N., Teriaca, L., Tripathi, D., Solanki, S. K., Wiegelmann, T., 2012, Doppler shift of hot coronal lines in a moss area of an active region, Astronomy and Astrophysics, 548, A115

Dammasch, I. E., Hassler, D. M., Wilhelm, K., Curdt, W., 1999a, Solar Mg X and Fe XII Wavelengths Measured By SUMER, in 8th SOHO Workshop: Plasma Dynamics and Diagnostics in the Solar Transition Region and Corona, (Ed.) J.-C. Vial & B. Kaldeich-Schü, vol. 446 of ESA Special Publication, p. 263

Dammasch, I. E., Wilhelm, K., Curdt, W., Hassler, D. M., 1999b, The NE BT VIII (lambda 770) resonance line: solar wavelengths determined by SUMER on SOHO, Astronomy and Astrophysics, 346, 285–294

Danilovic, S., Schüssler, M., Solanki, S. K., 2010, Probing quiet Sun magnetism using MURaM simulations and Hinode/SP results: support for a local dynamo, Astronomy and Astrophysics, 513, A1

De Pontieu, B., Tarbell, T., Erdélyi, R., 2003, Correlations on Arcsecond Scales between Chromospheric and Transition Region Emission in Active Regions, The Astrophysical Journal, 590, 502–518

De Pontieu, B., McIntosh, S., Hansteen, V. H., Carlsson, M., Schrijver, C. J., Tarbell, T. D., Title, A. M., Shine, R. A., Suematsu, Y., Tsuneta, S., Katsukawa, Y., Ichimoto, K., Shimizu, T., Nagata, S., 2007, A Tale of Two Spicules: The Impact of Spicules on the Magnetic Chromosphere, Publications of the Astronomical Society of Japan, 59, 655

De Pontieu, B., McIntosh, S. W., Hansteen, V. H., Schrijver, C. J., 2009, Observing the Roots of Solar Coronal Heating-in the Chromosphere, The Astrophysical Journal Letters, 701, L1–L6, `0906.5434`

De Pontieu, B., McIntosh, S. W., Carlsson, M., Hansteen, V. H., Tarbell, T. D., Boerner, P., Martinez-Sykora, J., Schrijver, C. J., Title, A. M., 2011, The Origins of Hot Plasma in the Solar Corona, Science, 331, 55–58

Del Zanna, G., 2008, Flows in active region loops observed by Hinode EIS, Astronomy and Astrophysics, 481, L49–L52

Del Zanna, G., Bromage, B. J. I., 1999, Transition Region Densities And Abundances As Derived From SOHO/CDS Observations., in 8th SOHO Workshop: Plasma Dynamics and Diagnostics in the Solar Transition Region and Corona, (Eds.) J.-C. Vial, B. Kaldeich-Schü, vol. 446 of ESA Special Publication, p. 269

Del Zanna, G., Storey, P. J., Badnell, N. R., Mason, H. E., 2012, Atomic data for astrophysics: Fe xii soft X-ray lines, The Astrophysical Journal, 543, A139

Delaboudinière, J.-P., Artzner, G. E., Brunaud, J., Gabriel, A. H., Hochedez, J. F., Millier, F., Song, X. Y., Au, B., Dere, K. P., Howard, R. A., Kreplin, R., Michels, D. J., Moses, J. D., Defise, J. M., Jamar, C., Rochus, P., Chauvineau, J. P., Marioge, J. P., Catura, R. C., Lemen, J. R., Shing, L., Stern, R. A., Gurman, J. B., Neupert, W. M., Maucherat, A., Clette, F., Cugnon, P., van Dessel, E. L., 1995, EIT: Extreme-Ultraviolet Imaging Telescope for the SOHO Mission, Solar Physics, 162, 291–312

Dere, K. P., Moses, J. D., Delaboudinière, J.-P., Brunaud, J., Carabetian, C., Hochedez, J.-F., Song, X. Y., Catura, R. C., Clette, F., Defise, J.-M., 2000, The Preflight Photometric Calibration of the Extreme-Ultraviolet Imaging Telescope EIT, Solar Physics, 195, 13–44

Domínguez Cerdeña, I., Sánchez Almeida, J., Kneer, F., 2006, The Distribution of Quiet Sun Magnetic Field Strengths from 0 to 1800 G, The Astrophysical Journal, 636, 496–509

Doschek, G. A., Bohlin, J. D., Feldman, U., 1976, Doppler wavelength shifts of transition zone lines measured in SKYLAB solar spectra, The Astrophysical Journal Letters, 205, L177–L180

Doschek, G. A., Mariska, J. T., Warren, H. P., Brown, C. M., Culhane, J. L., Hara, H., Watanabe, T., Young, P. R., Mason, H. E., 2007, Nonthermal Velocities in Solar Active Regions Observed with the Extreme-Ultraviolet Imaging Spectrometer on Hinode, The Astrophysical Journal Letter, 667, L109–L112

Doschek, G. A., Warren, H. P., Mariska, J. T., Muglach, K., Culhane, J. L., Hara, H., Watanabe, T., 2008, Flows and Nonthermal Velocities in Solar Active Regions Observed with the EUV Imaging Spectrometer on Hinode: A Tracer of Active Region Sources of Heliospheric Magnetic Fields?, The Astrophysical Journal, 686, 1362–1371

Edlén, B., 1934, Wellenlängen und Terme des Fluorspektrums FV, Z. Physik, 89, 597–600

Edlén, B., 1942, Z. Astrophysics, 22, 30

Fletcher, L., de Pontieu, B., 1999, Plasma Diagnostics of Transition Region "Moss" using SOHO/CDS and TRACE, The Astrophysical Journal Letter, 520, L135–L138

Gebbie, K. B., Hill, F., November, L. J., Gurman, J. B., Shine, R. A., Woodgate, B. E., Athay, R. G., Tandberg-Hanssen, E. A., Toomre, J., Simon, G. W., 1981, Steady flows in the solar transition region observed with SMM, The Astrophysical Journal Letters, 251, L115–L118

Grotrian, W., 1939, Naturwissenschaften, 27, 214

Gudiksen, B. V., Nordlund, Å., 2002, Bulk Heating and Slender Magnetic Loops in the Solar Corona, The Astrophysical Journal Letter, 572, L113–L116

Handy, B. N., Acton, L. W., Kankelborg, C. C., Wolfson, C. J., Akin, D. J., Bruner, M. E., Caravalho, R., Catura, R. C., Chevalier, R., Duncan, D. W., Edwards, C. G., Feinstein, C. N., Freeland, S. L., Friedlaender, F. M., Hoffmann, C. H., Hurlburt, N. E., Jurcevich, B. K., Katz, N. L., Kelly, G. A., Lemen, J. R., Levay, M., Lindgren, R. W., Mathur, D. P., Meyer, S. B., Morrison, S. J., Morrison, M. D., Nightingale, R. W., Pope, T. P., Rehse, R. A., Schrijver, C. J., Shine, R. A., Shing, L., Strong, K. T., Tarbell, T. D., Title, A. M., Torgerson, D. D., Golub, L., Bookbinder, J. A., Caldwell, D., Cheimets, P. N., Davis, W. N., Deluca, E. E., McMullen, R. A., Warren, H. P., Amato, D., Fisher, R., Maldonado, H., Parkinson, C., 1999, The transition region and coronal explorer, Solar Physics, 187, 229–260

Hansteen, V., 1993, A new interpretation of the redshift observed in optically thin transition region lines, The Astrophysical Journal, 402, 741–755

Hansteen, V., Maltby, P., Malagoli, A., 1997, Are the redshifts observed in transition region lines caused by magnetic reconnection?, in Magnetic Reconnection in the Solar Atmosphere, (Ed.) R. D. B. . J. T. Mariska, vol. 111 of ASP Conf. Ser., p. 116

Hansteen, V. H., Wikstol, O., 1994, Transition region lineshifts in the rebound shock spicule model., Astronomy and Astrophysics, 290, 995–1000

Hansteen, V. H., Hara, H., De Pontieu, B., Carlsson, M., 2010, On Redshifts and Blueshifts in the Transition Region and Corona, The Astrophysical Journal, 718, 1070–1078

Hara, H., Watanabe, T., Harra, L. K., Culhane, J. L., Young, P. R., Mariska, J. T., Doschek, G. A., 2008a, Coronal Plasma Motions near Footpoints of Active Region Loops Revealed from Spectroscopic Observations with Hinode EIS, The Astrophysical Journal Letter, 678, L67–L71

Hara, H., Watanabe, T., Harra, L. K., Culhane, J. L., Young, P. R., Mariska, J. T., Doschek, G. A., 2008b, Coronal Plasma Motions near Footpoints of Active Region Loops Revealed from Spectroscopic Observations with Hinode EIS, The Astrophysical Journal Letters, 678, L67–L71

Hassler, D. M., Rottman, G. J., Orrall, F. Q., 1991, Absolute velocity measurements in the solar transition region and corona, Advances in Space Research, 11, 141–145

Heroux, L., Hinteregger, H. E., 1978, Aeronomical reference spectrum for solar UV below 2000 A, Journal of Geophysical Research, 83, 5305–5308

Judge, P. G., Hansteen, V., Wikstol, O., Wilhelm, K., Schuehle, U., Moran, T., 1998, Evidence in Support of the "Nanoflare" Picture of Coronal Heating from SUMER Data, The Astrophysical Journal, 502, 981–996

Kamio, S., Hara, H., Watanabe, T., Fredvik, T., Hansteen, V. H., 2010, Modeling of EIS Spectrum Drift from Instrumental Temperatures, Solar Physics, 266, 209–223

Kaufman, V., Martin, W. C., 1991, The Journal of Physical Chemistry Reference Data, 20

Kelly, R. L., 1987, Atomic and ionic spectrum lines below 2000 Angstroms. Hydrogen through Krypton, vol. 16, New York: American Institute of Physics (AIP), American Chemical Society and the National Bureau of Standards

Kjeldseth-Moe, O., 2003, The solar transition region, pp. 196–216, Cambridge University Press

Klimchuk, J. A., 2006, On Solving the Coronal Heating Problem, Solar Physics, 234, 41–77

Klimchuk, J. A., 2009, Coronal Loop Models and Those Annoying Observations! (Keynote), in The Second Hinode Science Meeting: Beyond Discovery-Toward Understanding, (Ed.) B. Lites, M. Cheung, T. Magara, J. Mariska, & K. Reeves, vol. 415 of Astronomical Society of the Pacific Conference Series, p. 221

Klimchuk, J. A., Karpen, J. T., Antiochos, S. K., 2010, Can Thermal Nonequilibrium Explain Coronal Loops?, The Astrophysical Journal, 714, 1239–1248

Korendyke, C. M., Brown, C. M., Thomas, R. J., Keyser, C., Davila, J., Hagood, R., Hara, H., Heidemann, K., James, A. M., Lang, J., Mariska, J. T., Moser, J., Moye, R., Myers, S., Probyn, B. J., Seely, J. F., Shea, J., Shepler, E., Tandy, J., 2006, Optics and mechanisms for the Extreme-Ultraviolet Imaging Spectrometer on the Solar-B satellite, Applied Optics, 45, 8674–8688

Krieger, A. S., Timothy, A. F., Roelof, E. C., 1973, A Coronal Hole and Its Identification as the Source of a High Velocity Solar Wind Stream, Solar Physics, 29, 505–525

Laming, J. M., 2004, A Unified Picture of the First Ionization Potential and Inverse First Ionization Potential Effects, The Astrophysical Journal, 614, 1063–1072

Landi, E., Del Zanna, G., Young, P. R., Dere, K. P., Mason, H. E., 2012, CHIANTI–An Atomic Database for Emission Lines. XII. Version 7 of the Database, The Astrophysical Journal, 744, 99

Lemaire, P., Wilhelm, K., Curdt, W., Schule, U., Marsch, E., Poland, A. I., Jordan, S. D., Thomas, R. J., Hassler, D. M., Vial, J. C., Kuhne, M., Huber, M. C. E., Siegmund, O. H. W., Gabriel, A., Timothy, J. G., Grewing, M., 1997, First Results of the SUMER Telescope and Spectrometer on SOHO - II. Imagery and Data Management, Solar Physics, 170, 105–122

Lemen, J. R., Title, A. M., Akin, D. J., Boerner, P. F., Chou, C., Drake, J. F., Duncan, D. W., Edwards, C. G., Friedlaender, F. M., Heyman, G. F., Hurlburt, N. E., Katz, N. L., Kushner, G. D., Levay, M., Lindgren, R. W., Mathur, D. P., McFeaters, E. L., Mitchell, S., Rehse, R. A., Schrijver, C. J., Springer, L. A., Stern, R. A., Tarbell, T. D., Wuelser, J.-P., Wolfson, C. J., Yanari, C., Bookbinder, J. A., Cheimets, P. N., Caldwell, D., Deluca, E. E., Gates, R., Golub, L., Park, S., Podgorski, W. A., Bush, R. I., Scherrer, P. H., Gummin, M. A., Smith, P., Auker, G., Jerram, P., Pool, P., Soufli, R., Windt, D. L., Beardsley, S., Clapp, M., Lang, J., Waltham, N., 2012, The Atmospheric Imaging Assembly (AIA) on the Solar Dynamics Observatory (SDO), Solar Physics, 275, 17–40

Magdalenic, J., Marque, C., 2010, The coronal electron density profiles derived from radio observations, in 38th COSPAR Scientific Assembly, vol. 38 of COSPAR Meeting, p. 3024

Mariska, J. T., 1987, Solar transition region and coronal response to heating rate perturbations, The Astrophysical Journal, 319, 465–480

Mariska, J. T., 1988, Observational signatures of loop flows driven by asymmetric heating, The Astrophysical Journal, 334, 489–493

Mariska, J. T., 1992, The solar transition region

Mariska, J. T., Boris, J. P., 1983, Dynamics and spectroscopy of asymmetrically heated coronal loops, The Astrophysical Journal, 267, 409–420

Marsch, E., Tu, C.-Y., 1997, The effects of high-frequency Alfven waves on coronal heating and solar wind acceleration., Astronomy and Astrophysics, 319, L17–L20

Martens, P. C. H., Kankelborg, C. C., Berger, T. E., 2000, On the Nature of the "Moss" Observed by TRACE, The Astrophysical Journal, 537, 471–480

McClymont, A. N., Craig, I. J. D., 1987, Fast downflows in the solar transition region explained, The Astrophysical Journal, 312, 402–411

McIntosh, S. W., De Pontieu, B., 2009a, Observing Episodic Coronal Heating Events Rooted in Chromospheric Activity, The Astrophysical Journal Letters, 706, L80–L85

McIntosh, S. W., De Pontieu, B., 2009b, High-Speed Transition Region and Coronal Upflows in the Quiet Sun, The Astrophysical Journal, 707, 524–538

Muglach, K., Landi, E., Doschek, G. A., 2010, The Electron Temperature of the Solar Transition Region as Derived from EIS and SUMER, The Astrophysical Journal, 708, 550–559

Noci, G., 1981, Siphon flows in the solar corona, Solar Physics, 69, 63–76

Orlando, S., Peres, G., Serio, S., 1995, Models of stationary siphon flows in stratified, thermally conducting coronal loops. II. Shocked solutions., The Astrophysical Journal, 300, 549

Pagano, I., Linsky, J. L., Valenti, J., Duncan, D. K., 2004, HST/STIS high resolution echelle spectra of α Centauri A (G2 V), Astronomy and Astrophysics, 415, 331–348

Patsourakos, S., Klimchuk, J. A., 2006, Nonthermal Spectral Line Broadening and the Nanoflare Model, The Astrophysical Journal, 647, 1452–1465

Patsourakos, S., Klimchuk, J. A., MacNeice, P. J., 2004, The Inability of Steady-Flow Models to Explain the Extreme-Ultraviolet Coronal Loops, The Astrophysical Journal, 603, 322–329

Pérez, M. E., Doyle, J. G., O'Shea, E., Keenan, F., 1999, SUMER Measurements of Electron Density Enhancements in the Solar Transition Region, in Magnetic Fields and Solar Processes, (Eds.) A. Wilson, et al., vol. 448 of ESA Special Publication, p. 629

Peter, H., 1999, Analysis of Transition-Region Emission-Line Profiles from Full-Disk Scans of the Sun Using the SUMER Instrument on SOHO, The Astrophysical Journal, 516, 490–504

Peter, H., 2004, Structure and Dynamics of the Low Corona of the Sun (With 13 Figures), in Reviews in Modern Astronomy, (Ed.) R. E. Schielicke, vol. 17 of Reviews in Modern Astronomy, p. 87

Peter, H., Judge, P. G., 1999, On the Doppler Shifts of Solar Ultraviolet Emission Lines, The Astrophysical Journal, 522, 1148–1166

Peter, H., Vocks, C., 2003, Heating the magnetically open ambient background corona of the Sun by Alfven waves, Astronomy and Astrophysics, 411, L481–L485

Peter, H., Gudiksen, B. V., Nordlund, Å., 2004, Coronal Heating through Braiding of Magnetic Field Lines, The Astrophysical Journal Letters, 617, L85–L88

Peter, H., Gudiksen, B. V., Nordlund, Å., 2006, Forward Modeling of the Corona of the Sun and Solar-like Stars: From a Three-dimensional Magnetohydrodynamic Model to Synthetic Extreme-Ultraviolet Spectra, The Astrophysical Journal, 638, 1086–1100

Pneuman, G. W., Kopp, R. A., 1978, Downflow in the supergranulation network and its implications for transition region models, Solar Physics, 57, 49–64

Podgorski, W. A., Cheimets, P. N., Boerner, P., Glenn, P., 2009, SDO-AIA mirror performance, in Society of Photo-Optical Instrumentation Engineers (SPIE) Conference Series, vol. 7438 of Society of Photo-Optical Instrumentation Engineers (SPIE) Conference Series

Samain, D., 1991, Is the ultraviolet spectrum of the quiet sun redshifted?, Astronomy and Astrophysics, 244, 217–227

Schou, J., Scherrer, P. H., Bush, R. I., Wachter, R., Couvidat, S., Rabello-Soares, M. C., Bogart, R. S., Hoeksema, J. T., Liu, Y., Duvall, T. L., Akin, D. J., Allard, B. A., Miles, J. W., Rairden, R., Shine, R. A., Tarbell, T. D., Title, A. M., Wolfson, C. J., Elmore, D. F., Norton, A. A., Tomczyk, S., 2012, Design and Ground Calibration of the Helioseismic and Magnetic Imager (HMI) Instrument on the Solar Dynamics Observatory (SDO), Solar Physics, 275, 229–259

Schrijver, C. J., 2001, The Coronae of the Sun and Solar-type Stars (CD-ROM Directory: contribs/schrijv), in 11th Cambridge Workshop on Cool Stars, Stellar Systems and the Sun, (Eds.) R. J. Garcia Lopez, R. Rebolo, M. R. Zapaterio Osorio, vol. 223 of Astronomical Society of the Pacific Conference Series, p. 131

Schrijver, C. J., Title, A. M., Berger, T. E., Fletcher, L., Hurlburt, N. E., Nightingale, R. W., Shine, R. A., Tarbell, T. D., Wolfson, J., Golub, L., Bookbinder, J. A., Deluca, E. E., McMullen, R. A., Warren, H. P., Kankelborg, C. C., Handy, B. N., de Pontieu, B., 1999, A new view of the solar outer atmosphere by the Transition Region and Coronal Explorer, Solar Physics, 187, 261–302

Spadaro, D., Antiochos, S. K., Mariska, J. T., 1991, Nonequilibrium ionization effects in asymmetrically heated loops, The Astrophysical Journal, 382, 338–343

Spadaro, D., Lanza, A. F., Karpen, J. T., Antiochos, S. K., 2006, A Transient Heating Model for the Structure and Dynamics of the Solar Transition Region, The Astrophysical Journal, 642, 579–583

Teriaca, L., 2001, Structure and dynamics of solar outer atmosphere as inferred from EUV observations, Ph.D. thesis, Department of Pure and Applied physics, The Queen's University of Belfast, Belfast, Northern Ireland

Teriaca, L., Banerjee, D., Doyle, J. G., 1999a, SUMER observations of Doppler shift in the quiet Sun and in an active region, Astronomy and Astrophysics, 349, 636–648

Teriaca, L., Doyle, J. G., Erdélyi, R., Sarro, L. M., 1999b, New insight into transition region dynamics via SUMER observations and numerical modelling, Astronomy and Astrophysics, 352, L99–L102

Teriaca, L., Madjarska, M. S., Doyle, J. G., 2002, Transition region explosive events: Do they have a coronal counterpart?, Astronomy and Astrophysics, 392, 309–317

Teriaca, L., Andretta, V., Auchère, F., Brown, C. M., Buchlin, E., Cauzzi, G., Culhane, J. L., Curdt, W., Davila, J. M., Del Zanna, G., Doschek, G. A., Fineschi, S., Fludra, A., Gallagher, P. T., Green, L., Harra, L. K., Imada, S., Innes, D., Kliem, B., Korendyke,

C., Mariska, J. T., Martínez-Pillet, V., Parenti, S., Patsourakos, S., Peter, H., Poletto, L., Rutten, R. J., Schühle, U., Siemer, M., Shimizu, T., Socas-Navarro, H., Solanki, S. K., Spadaro, D., Trujillo-Bueno, J., Tsuneta, S., Dominguez, S. V., Vial, J.-C., Walsh, R., Warren, H. P., Wiegelmann, T., Winter, B., Young, P., 2011, LEMUR: Large European module for solar Ultraviolet Research, Experimental Astronomy, p. 135

Tian, H., Tu, C., Marsch, E., He, J., Zhou, G., 2008, Signature of mass supply to quiet coronal loops, Astronomy and Astrophysics, 478, 915–919

Tian, H., Marsch, E., Tu, C., Curdt, W., He, J., 2010, New views on the emission and structure of the solar transition region, New Astronomy Reviews, 54, 13–30

Tripathi, D., Mason, H. E., Young, P. R., Del Zanna, G., 2008, Density structure of an active region and associated moss using Hinode/EIS, The Astrophysical Journal, 481, L53–L56

Tripathi, D., Mason, H. E., Dwivedi, B. N., del Zanna, G., Young, P. R., 2009, Active Region Loops: Hinode/Extreme-Ultraviolet Imaging Spectrometer Observations, The Astrophysical Journal, 694, 1256–1265

Tripathi, D., Mason, H. E., Del Zanna, G., Young, P. R., 2010a, Active region moss. Basic physical parameters and their temporal variation, The Astrophysical Journal, 518, A42

Tripathi, D., Mason, H. E., Klimchuk, J. A., 2010b, Evidence of Impulsive Heating in Active Region Core Loops, The Astrophysical Journal, 723, 713–718

Tripathi, D., Klimchuk, J. A., Mason, H. E., 2011, Emission Measure Distribution and Heating of Two Active Region Cores, The Astrophysical Journal, 740, 111

Tripathi, D., Mason, H. E., Klimchuk, J. A., 2012, Active Region Moss: Doppler Shifts from Hinode/Extreme-ultraviolet Imaging Spectrometer Observations, The Astrophysical Journal, 753, 37

Tripathi, D., Klimchuk, J., a. M. H. E., Young, P. R., in preparation

Trujillo Bueno, J., Shchukina, N., Asensio Ramos, A., 2004, A substantial amount of hidden magnetic energy in the quiet Sun, Nature, 430, 326–329

Tu, C.-Y., Marsch, E., 1997, Two-Fluid Model for Heating of the Solar Corona and Acceleration of the Solar Wind by High-Frequency Alfven Waves, Solar Physics, 171, 363–391

Ugarte-Urra, I., Warren, H. P., Brooks, D. H., 2009, Active Region Transition Region Loop Populations and Their Relationship to the Corona, The Astrophysical Journal, 695, 642–651

Vernazza, J. E., Avrett, E. H., Loeser, R., 1981, Structure of the solar chromosphere. III - Models of the EUV brightness components of the quiet-sun, The Astrophysical Journal, 45, 635–725

Viall, N. M., Klimchuk, J. A., 2011, Patterns of Nanoflare Storm Heating Exhibited by an Active Region Observed with Solar Dynamics Observatory/Atmospheric Imaging Assembly, The Astrophysical Journal, 738, 24

Viall, N. M., Klimchuk, J. A., Goddard Space Flight Center, N., 2012, Evidence for Widespread Cooling in an Active Region Observed with the SDO Atmospheric Imaging Assembly, The Astrophysical Journal

Walsh, R. W., Ireland, J., 2003, The heating of the solar corona, The Astronomy and Astrophysics Review, 12, 1–41

Warren, H. P., Brooks, D. H., 2009, The Temperature and Density Structure of the Solar Corona. I. Observations of the Quiet Sun with the EUV Imaging Spectrometer on Hinode, The Astrophysical Journal, 700, 762–773

Warren, H. P., Winebarger, A. R., Mariska, J. T., 2003, Evolving Active Region Loops Observed with the Transition Region and Coronal explorer. II. Time-dependent Hydrodynamic Simulations, The Astrophysical Journal, 593, 1174–1186

Warren, H. P., Winebarger, A. R., Mariska, J. T., Doschek, G. A., Hara, H., 2008, Observation and Modeling of Coronal "Moss" With the EUV Imaging Spectrometer on Hinode, The Astrophysical Journal, 677, 1395–1400

Warren, H. P., Winebarger, A. R., Brooks, D. H., 2010, Evidence for Steady Heating: Observations of an Active Region Core with Hinode and TRACE, The Astrophysical Journal, 711, 228–238

Wiegelmann, T., Thalmann, J. K., Inhester, B., Tadesse, T., Sun, X., Hoeksema, J. T., 2012, How Should One Optimize Nonlinear Force-Free Coronal Magnetic Field Extrapolations from SDO/HMI Vector Magnetograms?, Solar Physics, p. 67

Wilhelm, K., 2012, SUMER Observations of Coronal-Hole Temperatures, Space Science Reviews, 172, 57–68

Wilhelm, K., Curdt, W., Marsch, E., Schühle, U., Lemaire, P., Gabriel, A., Vial, J., Grewing, M., Huber, M. C. E., Jordan, S. D., Poland, A. I., Thomas, R. J., Kühne, M., Timothy, J. G., Hassler, D. M., Siegmund, O. H. W., 1995, SUMER - Solar Ultraviolet Measurements of Emitted Radiation, Solar Physics, 162, 189–231

Wilhelm, K., Lemaire, P., Curdt, W., Schuhle, U., Marsch, E., Poland, A. I., Jordan, S. D., Thomas, R. J., Hassler, D. M., Huber, M. C. E., Vial, J.-C., Kuhne, M., Siegmund, O. H. W., Gabriel, A., Timothy, J. G., Grewing, M., Feldman, U., Hollandt, J., Brekke, P., 1997, First Results of the SUMER Telescope and Spectrometer on SOHO - I. Spectra and Spectroradiometry, Solar Physics, 170, 75–104

Wilhelm, K., Dwivedi, B. N., Marsch, E., Feldman, U., 2004, Observations of the Sun at Vacuum- Ultraviolet Wavelengths from Space. Part I: Concepts and Instrumentation, Space Science Reviews, 111, 415–480

Winebarger, A., Tripathi, D., Mason, H. E., Del Zanna, G., submitted, 2012, Doppler shifts in active region moss using soho/sumer, The Astrophysical Journal

Winebarger, A. R., Warren, H., van Ballegooijen, A., DeLuca, E. E., Golub, L., 2002, Steady Flows Detected in Extreme-Ultraviolet Loops, The Astrophysical Journal Letter, 567, L89–L92

Winebarger, A. R., Warren, H. P., Falconer, D. A., 2008, Modeling X-Ray Loops and EUV "Moss" in an Active Region Core, The Astrophysical Journal, 676, 672–679

Winebarger, A. R., Schmelz, J. T., Warren, H. P., Saar, S. H., Kashyap, V. L., 2011, Using a Differential Emission Measure and Density Measurements in an Active Region Core to Test a Steady Heating Model, The Astrophysical Journal, 740, 2

Withbroe, G. L., 1983, The role of spicules in heating the solar atmosphere Implications of EUV observations, The Astrophysical Journal, 267, 825–836

Withbroe, G. L., Noyes, R. W., 1977, Mass and energy flow in the solar chromosphere and corona, Annual Review of Astronomy and Astrophysics, 15, 363–387

Wood, B. E., Harper, G. M., Linsky, J. L., Dempsey, R. C., 1996, Goddard High-Resolution Spectrograph Observations of Procyon and HR 1099, The Astrophysical Journal, 458, 761–782

Young, P. R., Del Zanna, G., Mason, H. E., Dere, K. P., Landi, E., Landini, M., Doschek, G. A., Brown, C. M., Culhane, L., Harra, L. K., Watanabe, T., Hara, H., 2007a, EUV Emission Lines and Diagnostics Observed with Hinode/EIS, Publications of the Astronomical Society of Japan, 59, 857

Young, P. R., Del Zanna, G., Mason, H. E., Doschek, G. A., Culhane, L., Hara, H., 2007b, Solar Transition Region Features Observed with Hinode/EIS, Publications of the Astronomical Society of Japan, 59, 727

Young, P. R., Watanabe, T., Hara, H., Mariska, J. T., 2009, High-precision density measurements in the solar corona. I. Analysis methods and results for Fe XII and Fe XIII, Astronomy and Astrophysics, 495, 587–606

Young, P. R., O'Dwyer, B., Mason, H. E., 2012, Velocity Measurements for a Solar Active Region Fan Loop from Hinode/EIS Observations, The Astrophysical Journal, 744, 14

Zhang, Y. Z., Shibata, K., Wang, J. X., Mao, X. J., Matsumoto, T., Liu, Y., Su, J. T., 2012, Revision of Solar Spicule Classification, The Astrophysical Journal, 750, 16

Acknowledgements

Lebenslauf

Persönliche Daten:

Name   Neda Dadashigharehbalagh
Geburtsdatum   13. Mai 1982
Geburtsort   Qaemshahr, Iran
Staatsangehorigkeit   Iranisch

Schulausbildung:

10/1988-06/1993   Grundschule: Esmatiyeh Schule, Qaemshahr, Iran
10/1993-06/2000   Gymnasium: Farzanegan (SAMPAD) Schule, Qaemshahr, Iran

Studium:

10/2000-09/2004   B.S. in Festkörperphysik,
                  Isfahan University, Isfahan, Iran
10/2005-02/2008   M.S. in Astrophysik,
                  Zanjan University, Zanjan, Iran

4/2009-2013   Promotion,
                  MPI für Sonnensystemforschung, Katlenburg Lindau, Germany
                  Technische Universität Carolo-Wilhelmina zu Braunschweig,
                  Germany